공학박사학위논문

Molecular Imaging of Cancer-related Molecules in Cancer Cells and their Microenvironment

암세포와 종양미세환경에서 암 관련 분자들에 대한 분자영상 연구

2014년 8월

서울대학교 대학원

화학생물공학부

류 주 희

암세포와 종양미세환경에서
암 관련 분자들에 대한 분자영상 연구

Molecular Imaging of Cancer-related Molecules in Cancer Cells and their Microenvironment

지도 교수 김 병 수

이 논문을 공학박사 학위논문으로 제출함

2014년 6월

서울대학교 대학원

화학생물공학부

류 주 희

류주희의 공학박사 학위논문을 인준함

2014년 6월

위 원 장 _____ (인)

부위원장 _____ (인)

위 원 _____ (인)

위 원 _____ (인)

위 원 _____ (인)

Abstract

Molecular Imaging of Cancer-related Molecules in Cancer Cells and their Microenvironment

Ju Hee Ryu

School of Chemical and Biological Engineering

The Graduate School

Seoul National University

Molecular imaging is a key element of cancer management in the 21st century. Molecular imaging enables the visualization and characterization of cancer-specific events at the cellular and molecular levels in living systems. It allows cancerous lesions to be detected at an earlier stage, which is one of the most effective strategies for cancer treatment. In addition, it has a major impact on intra-operative cancer detection, the real-time validation of therapy, as well as the knowledge of the role of cancer-related components. Specifically, optical imaging is a highly sensitive and non-invasive molecular imaging technique, in contrast to anatomical imaging approaches.

Cancer research has been focused on studying and characterizing the genetically determined expression of biomolecules by cancer cells in the past several decades. For targeted cancer imaging, over-expressed receptors on the surface of cancer cells or over-produced enzymes by cancer cells have been utilized. However, genetic and epigenetic alterations in tumor cells have been found to be insufficient to offer tumor cells with malignant properties although they are prerequisites for malignant processes. In recent years, it has become obvious that other components of tumors, such as non-tumor cells (endothelial cells, fibroblasts), connective tissue, extracellular matrix (ECM), immune cells, and soluble factors play fundamental roles in tumor development and progression. These components are collectively known as the tumor microenvironment. Therefore, increased attention has been paid to the tumor microenvironment as well as cancer cells for cancer imaging.

In this study, imaging probes were first developed to target and visualize the components of cancer cell or the tumor microenvironment; the probes were then applied for cancer imaging. In Chapter 2, cathepsin B (CB), an over-produced enzyme by cancer cells was targeted and visualized in metastatic tumor models. The fact that the activity of CB is markedly linked to the metastatic process and that CB is found highly expressed in the pericellular regions in this process makes CB an attractive target for diagnosing metastases. A CB-sensitive nanoprobe (CB-CNP) was developed to include CB-sensitive fluorescence peptide probes conjugated onto the surface of tumor-targeting glycol chitosan nanoparticles (CNPs). The fluorescence intensity of the CB-CNP was strongly quenched in physiological

condition. However, self-quenched CB-CNP boosted strong fluorescence signals in the presence of CB, not of cathepsin L or cathepsin D, due to the CB-specific cleavage of peptide probes. Importantly, the intravenously injected CB-CNP demonstrated the potential to discriminate metastases *in vivo* in three metastatic mouse models, including 4T1-luc2 liver metastases, RFP-B16F10 lung metastases and HT1080 peritoneal metastases. CB-CNPs may be useful for depicting metastases through the non-invasive molecular imaging of CB activity.

In Chapter 3, an over-expressed receptor on the surface of cancer cells, epidermal growth factor receptor (EGFR), was targeted for cancer imaging. Herein, an epidermal growth factor-based nanoprobe (EGF-NP) was developed for the *in vivo* optical imaging of EGFR. The self-quenched EGF-NP is fabricated by sequentially conjugating a near-infrared (NIR) fluorophore (Cy5.5) and a quencher (BHQ-3) to EGF, a low-molecular weight polypeptide (6.2 kDa), compared to EGFR antibody (150 kDa). The self-quenched EGF-NP presented great specificity to EGFR, and rapidly internalized into the cells. Importantly, the self-quenched EGF-NP boosted strong fluorescence signals upon EGFR-targeted uptake into EGFR-expressing cells, followed by lysosomal degradation, as confirmed by lysosomal marker cell imaging. Consistent with the cellular results, the intravenous injection of EGF-NP into tumor-bearing mice induced strong NIR fluorescence intensity in the target tumor tissue with high specificity against EGFR-expressing cancer cells. The signal accumulation of EGF-NP in tumors was much faster than that of EGFR monoclonal antibody (Cetuximab)-Cy5.5 conjugates due to the rapid clearance from the body

and tissue permeability of low-molecular weight EGF. This self-quenched, EGF-based imaging probe can be applied to diagnose of various cancers.

In Chapter 4, the detection of lysyl oxidase (LOX) activity in ECM was attempted using gold nanoprobes. Stiffness of ECM is significantly associated with cancer progression and malignancy. LOX is considered as an important factor to affect stiffness of ECM among various factors. In addition, LOX has been validated for a prognostic marker for metastasis and survival in multiple cancer types including head and neck squamous cell carcinoma. Therefore, a sensitive and simple assay for detecting the activity of LOX is needed. The plasmon coupling-based color change using AuNPs has been widely used to detect the presence or amounts of analytes that cause the selective aggregation of AuNPs. The AuNPs were functionalized with LOX-sensitive hexapeptides (LOX-AuNPs) to detect LOX. LOX-AuNPs turn from their original pinkish red to purple and the absorption spectra of the LOX-AuNPs red-shifted in correlation with the LOX concentration. In addition, LOX-AuNPs showed high specificity for LOX as presented in the experiments with LOX inhibitor or Control-AuNPs. LOX-AuNPs demonstrated the potential to detect LOX in cancer cells and tumor tissues including different LOX contents. LOX detection by LOX-AuNPs in cancer cells was more sensitive compared to those by a commercially available LOX assay or Western blot analysis. LOX levels measured using LOX-AuNPs in various tumor tissues were correlated directly with their collagen contents and their ECM stiffness. Therefore, LOX-AuNPs may be applied to detecting LOX activity and further ECM stiffness of tumor tissues.

Successful surgical procedures for cancer treatment depend on the accurate and rapid localization of tumor tissues, following their correct resection. In Chapter 5, tumor tissue-specific imaging by topical application was attempted for rapid tumor visualization. It was hypothesized that tissue-permeable probes can differently accumulated in tumor or normal tissue due to the structural difference between them. To make tissue-permeable probes, the factor of high volume of distribution (Vd) was utilized. The Vd can be calculated as the ratio of the total amount of a drug in the body and its concentration in the blood at a steady state. A higher Vd indicates that the drug is more diluted than it should be in the blood, suggesting that a larger amount of the drug has been distributed in the tissue, not in blood. Accordingly, the drug with high Vd can be tissue-permeable. Four drug-dye conjugates were synthesized by directly coupling the NIR dye, FCR675, with 4 drugs with different Vd values, including raloxifene (2348 l/kg), scopolamine (3.1 l/kg), ampicillin (0.38 l/kg), and ibuprofen (0.15 l/kg). Drug-dye conjugates were topically applied via spraying on the liver surface of the HCT116 liver tumor-bearing mice and transanally applied via the anus into the descending colon of colon tumor-bearing mice. Topically applied Ralo-FCR675 also rapidly penetrated to the tumor's maximum depth and, more importantly, Ralo-FCR675 preferentially accumulated in the tumor lesions within 3 min. Vd could be a factor to differentiate between tumor tissue and non-tumor tissue. Fluorescently labeled drugs with high Vd, such as raloxifene may be useful for the rapid visualization of tumors, contributing to successful surgical procedures for cancer treatment.

Finally, in Chapter 6, tumor-associated macrophage (TAM) was targeted and visualized. Specifically, TAM infiltration into tumors has been strongly correlated with poor prognosis in multiple cancer types. Hence, the imaging of TAM infiltration in tumors could be helpful in clinical applications for the prognosis and treatment of tumors. Scavenger receptors class A (SR-A) is known to be highly expressed in the TAMs of multiple cancer types and to be recognized with various negatively charged macromolecules including dextran sulfate (DS). Herein, FPR675-labeled DS nanoprobes (DSNPs) were developed to detect TAMs. DSNPs were significantly uptaken into RAW264.7 macrophage cells and isolated TAMs, not in MDA-MB-468 cancer cells. In an MDA-MB-468 subcutaneous tumor model, DSNPs provide high fluorescence signal both in tumor and liver sites. Further immunohistochemical analyses demonstrated that DSNPs mainly target CD204-positive TAMs. Therefore, DSNPs could be potentially utilized to visualize TAM infiltration in tumors.

Keywords: molecular imaging, cancer imaging, optical imaging, tumor microenvironment, drug delivery system

Student Number: 2010-31012

Table of contents

Chapter 6. Imaging of tumor-associated macrophages using dextran sulfate-based nanoprobes

List of figures

50, 100 μg/ml). (C) Relative fluorescence intensity of the CB-CNP after incubation with various concentrations of CB (0, 1.0, 2.0, 4.0 and 8.0 nM) for 50 min at 37°C; lower, the corresponding NIR fluorescence images of the CB-CNP treated with various concentrations of CB. (D) Fluorescence emission spectra of the CB-CNP in the presence of different stimuli (CB, cathepsin D, cathepsin L, and CB with inhibitor) for 50 min at 37°C; lower, the corresponding NIR fluorescence images of the CB-CNP in the presence of different stimuli.

Figure 2.6. Cellular uptake and immunocytochemistry of cathepsin B (CB)-sensitive nanoprobe (CB-CNP). **(a**) Cellular uptake images of SCC7 cells in media containing in the presence or absence of CB inhibitor at 6h post-treatment of CB-CNP or CB-peptide probe.

Figure 2.7. *In vivo* near infrared (NIR) fluorescence imaging of CB activity in tumor tissue with cathepsin B (CB)-sensitive nanoprobe (CB-CNP). (a) Whole body NIR fluorescence images of SCC7 tumor-bearing mice after intravenous injection of CB-CNP or CB-peptide probe in the presence or absence of CB inhibitor. (b) NIR fluorescence signal intensity in tumor region of (a). (c) NIR fluorescence images of excised tumors and other organs. (d) NIR fluorescence signal intensity of (c). Asterisks indicate $p < 0.05$.

Figure 2.8. Cellular uptake of the cathepsin B (CB)-sensitive nanoprobe (CB-CNP) and immunocytochemistry for CB in the tumor cells. HT29, 4T1-luc2, RFP-B16F10, HT1080, and NIH3T3 cells were incubated in the media containing the CB-CNP (red) for 2 h. Fluorescein isothiocyanate-conjugated antibody against CB was used for CB imaging (green), and the nucleus was stained with DAPI (blue). The scale bar indicates 100 μm.

Figure 2.9. Probe specificity and detection sensitivity for cathepsin B (CB) in the

subcutaneous tumor model. (a) Whole-body fluorescence images of HT29 subcutaneous tumor-bearing mice after intravenous injection of the CB-sensitive nanoprobe (CB-CNP) in the absence or presence of CB inhibitor. (b) Fluorescence intensity in the tumor region of (a). Asterisks indicate $p < 0.05$. (c) **a** Hematoxylin and eosin staining of the tumor section, **b** immunohistochemical staining of the tumor section for CB, and fluorescence microscopy images of **c** the tumor section and **d** the inhibitor-treated tumor section. The CB-CNP was expressed in red and DAPI in blue in fluorescence microscopy images. (d) *Ex vivo* images of HT29 liver tumors 12 h after intravenous injection of the CB-CNP and CNP-Cy5.5.

Figure 2.10. *In vivo* NIR fluorescence imaging of cathepsin B (CB) activity in 4T1-luc2 liver metastases with intravenously injected CB-sensitive nanoprobe (CB-CNP). (a) Whole-body fluorescence images of 4T1-luc2 liver metastatic tumor-bearing mice or normal mice after intravenous injection of the CB-CNP. (b) *Ex vivo* images of 4T1-luc2 liver metastasis and normal liver acquired with the IVIS Spectrum imaging system or the KODAK image station 12 h after intravenous injection of the CB-CNP. Bioluminescence imaging indicated the metastatic liver cancer. (c) Western blot analysis to detect CB in liver metastasis and normal liver.

Figure 2.11. *In vivo* NIR fluorescence imaging of cathepsin B (CB) activity in RFP-B16F10 lung metastases with intravenously injected CB-sensitive nanoprobe (CB-CNP). (a) Whole-body fluorescence images of RFP-B16F10 lung metastatic tumor-bearing mice or normal mice after intravenous injection of the CB-CNP. (b) Three dimensional *in vivo* images of CB activity in lung metastases using VisEn FMT. (c) *Ex vivo* images of RFP-B16F10 lung metastases and normal lungs 12 h after intravenous injection of the CB-CNP. An RFP signal indicated the metastatic lung cancer and a Cy5.5 signal in lungs indicated high

accumulation and fluorescence activation of the CB-CNP. (d) Hematoxylin and eosin staining images of lung metastasis and normal lung. (e) Western blot analysis to detect CB in lung metastasis and normal lung.

Figure 2.12. *In vivo* NIR fluorescence imaging of cathepsin B (CB) activity in HT1080 peritoneal metastases with intravenously injected CB-sensitive nanoprobe (CB-CNP). (a) Whole-body fluorescence images of HT1080 peritoneal metastatic tumor-bearing mice after intravenous injection of the CB-CNP, acquired by Optix. (b) Whole-body fluorescence images of HT1080 peritoneal metastatic tumor-bearing mice 7 h after intravenous injection of the CB-CNP or phosphate buffered saline (PBS), acquired by an IVIS Spectrum imaging system. (c) *Ex vivo* images of HT1080 peritoneal metastases acquired with a KODAK image station or IVIS Spectrum imaging system 7 h after intravenous injection of the CB-CNP or PBS. (d) Hematoxylin and eosin staining images of peritoneal metastases and normal peritoneum.

Figure 3.1. Preparation of epidermal growth factor receptor (EGFR)-targeted fluorescence activatable nanoprobes. (a) Illustration of chemical reactions used to conjugate Cy5.5 and BHQ3 onto epidermal growth factor (EGF) and chemical structures of Cy5.5 and BHQ3. Each EGF has three amine groups (N-terminal and 2 lysine) available for reaction with Cy5.5 or BHQ3. Crystal structure of EGF was drawn by the program Pymol (DeLano, W.L. The PyMOL Molecular Graphics System (2002) on World Wide Web [http://www.pymol.org]). (b) Schematic presentation for activation of EGFR-targeted fluorescence activatable nanoprobes. EGF labeled with a NIR fluorophore and a quencher (EGF-NP) binds to EGFR, which leads to cellular internalization and intracellular degradation of EGF-NP in the lysosome. Then, lysosomal degradation of EGF-NP causes separation of the fluorophore from the

quencher, allowing recovered fluorescence only within the EGFR-positive cells.

Figure 3.2. HPLC profiles of (a) Cy5.5, (b) epidermal growth factor (EGF)-Cy5.5, (c) EGF, (d) epidermal growth factor-based nanoprobe (EGF-NP). The signal is detected at 280 nm.

Figure 3.3. Monitoring of epidermal growth factor (EGF)-based nanoprobe (EGF-NP) synthesis. (a) MALDI-TOF mass spectrometry of EGF, EGF-Cy5.5 and EGF-NP. (b) SDS-PAGE analysis for EGF, EGF-Cy5.5 and EGF-NP shows that Cy5.5 and BHQ3 are covalently conjugated to EGF molecules (6.2 kDa, left). The fluorescence intensity of EGF-NP was substantially declined compared to EGF-Cy5.5, which means EGF-NP was quenched (right). (c) Fluorescence emission spectra of EGF-Cy5.5 and EGF-NP.

Figure 3.4. De-quenching and cytotoxicity of epidermal growth factor-based nanoprobe (EGF-NP). (a) Fluorescence image of EGF-NP in phosphate buffered saline (PBS) with or without lysosyme and 5% sodium dodecyl sulfate (SDS). In PBS without lysosome and SDS, EGF-NP was quenched. After exposure to lysozyme and SDS for 20 min in room temperature, fluorescence intensity of EGF-NP increased 3.5-fold. (b) Fluorescence intensity of (a). *In vitro* cellular cytotoxicity of EGF-NP using the Cell Counting Kit-8 assay in (c) MDA-MB-468 and (d) MDA-MB-436 cells.

Figure 3.5. Cellular imaging of epidermal growth factor-based nanoprobe (EGF-NP) activation process. (a) Cellular images in MDA-MB-468 and MDA-MB-436 cells after treatment of EGF-NP (red) for 6 h. Nuclei were counterstained with DAPI (blue). (b) Cellular imaging of EGF-NP activation process in MDA-MB-468 cells. Cells incubated with EGF-NP (10 μM, red) were imaged at 5 min intervals over 90 min. (c) Cellular

imaging before and after washing. Cells incubated with EGF-NP (red) or Cetuximab-Cy5.5 (red) for 2 h were imaged with a fluorescence microscope. Then, the same cells were washed twice with phosphate buffered saline (pH 7.4) and visualized by microscope. Cells undergoing the washing process were also stained with DAPI (blue).

Figure 3.6. Binding assay showing the affinity of unmodified human epidermal growth factor (EGF) and EGF-based nanoprobe (EGF-NP) to anti-EGF antibody.

Figure 3.7. *In vivo* and *ex vivo* near infrared (NIR) fluorescence images of MDA-MB-468 and MDA-MB-436 tumors (n=5). (a) *In vivo* NIR fluorescence tomographic images of subcutaneous MDA-MB-468 and MDA-MB-436 tumor-bearing mice 30 min, 1, 3, 6 and 12 h after intravenous injection of the epidermal growth factor (EGF)-based nanoprobe (EGF-NP). Higher NIR fluorescence intensity was visualized in MDA-MB-468 tumors compared to MDA-MB-436 tumors. (b) NIR fluorescence images of excised tumors from mice at 3 h post-injection of EGF-NP.

Figure 3.8. NIR fluorescence images and histology of tumor-bearing mice intravenously injected with EGF-NP and pretreated with or without EGFR siRNA. EGFR siRNA was intratumorally injected into the tumor on the right flank 1 day before EGF-NP administration. (a) *In vivo* NIR fluorescence tomographic images of subcutaneous MDA-MB-468 tumor-bearing mice (n=4) at 1, 3 and 6 h after intravenous injection of the EGF-NP. Higher NIR fluorescence intensity was visualized in non-treated MDA-MB-468 tumors compared to siRNA-treated MDA-MB-468 tumors. (b) NIR fluorescence signal intensity in tumor region (n=4). (c) NIR fluorescence images of excised tumors from mice at 3 h post-injection of EGF-NP. (d,e) Hematoxylin and eosin staining, (f,g) immunohistochemical staining for EGF receptor (EGFR) and (h,i) fluorescence microscopy images of tumor sections.

FCR675. (b) Cellular uptake of various concentrations of Ralo-FCR675 (red). The nucleus was stained with DAPI (blue). The scale bar indicates 10 μm.

Figure 5.6. Measurement of how fast the drug-dye conjugates and free dye extravasate from blood vessels. (a) Representative fluorescence images and (b) fluorescence intensity graph of blood samples (n=3) obtained from mice intravenously injected with four drug-dye conjugates.

Figure 5.7. *In vivo* and e*x vivo* imaging in HCT116-luc liver tumor-bearing mice. (a) *In vivo* NIR fluorescence imaging (FI) and bioluminescence imaging (BLI) of exposed livers captured with an IVIS Spectrum imaging system after topical application via spraying for 3 min and subsequent washing. (b) *Ex vivo* near infrared (NIR) FI and BLI of excised livers of liver tumor-bearing mice with four drug-dye conjugates and free drug. (c) Cross-sectional NIR FI and BLI of livers in liver tumor-bearing mice with four drug-dye conjugates and free drug. The livers were cut along the green dotted lines in (b). (d) NIR fluorescence signal intensities according to tumor depth in cross-section images. (e) *Ex vivo* NIR FI of excised livers captured by OV-100 imaging system after topical application via spraying of Ralo-FCR675 and FCR675. (f) Cross-sectional NIR FI of livers in liver tumor-bearing mice with Ralo-FCR675 and FCR675. The livers were cut along the green dotted lines in (e).

Figure 5.8. Accumulation of the drug-dye conjugates analyzed in tumor sections. (a) Fluorescence signals in liver tumor sections of mice 20, 40 and 60 s after the topical application of Ralo-FCR675 (red) via spraying. (b) Fluorescence signals detected in liver tumor and normal liver sections of mice after the topical application of four drug-dye conjugates and free dye (red) for 3 min and subsequent washing. The nucleus was stained

Figure 6.3. Immunocytochemistry of the isolated tumor-associated macrophages (TAMs) and cellular uptake of dextran sulfate-based nanoprobes (DSNPs). (a) Immunocytochemistry against CD204 of the isolated TAMs. Fluorescein isothiocyanate-conjugated antibody against CD204 was used for CD204 (green) imaging. (b) Cellular uptakes of DSNPs (red) and CNPs (red) in MDA-MB-468 cancer cells, RAW264.7 macrophages, and the isolated TAMs. FPR675-labeled DSNPs or chitosan nanoprobes (CNPs) were displayed as red fluorescence signals. (c) Cellular uptake of DSNPs (red) in the co-culture system of cancer cells and macrophage cells. Cancer cells were stained with 5(6)-carboxyfluorescein N-hydroxysuccinimidyl ester (CFSE, green) cell labeling kit. The scale bars indicate 100 μm. The nucleus was stained with DAPI (blue).

Figure 6.4. *In vivo* and *ex vivo* near infrared (NIR) fluorescence imaging using dextran sulfate-based nanoprobes (DSNPs) in MDA-MB-468 tumor-bearing mice. (a) Whole-body NIR fluorescence images of MDA-MB-468 tumor-bearing mice after intravenous injection of DSNPs. (b) *Ex vivo* images of a liver and tumor acquired with the KODAK image station 24 h after intravenous injection of DSNPs.

Figure 6.5. Histological and immunohistochemical analyses of the excised MDA-MB-468 tumors. (a) Hematoxylin and eosin staining images of tumoral and peritumoral tissues from MDA-MB-468 subcutaneous tumors. The yellow dotted line indicates a large number of infiltrated macrophages in the peritumoral area, and the arrows indicate the small number of macrophages in the tumoral area. Immunohistochemical analysis of CD68 for tumoral and peritumoral tissues from MDA-MB-468 subcutaneous tumors. The scale bar indicates 25 μm. Fluorescein isothiocyanate-conjugated antibodies against (b) F4/80 or (c) CD204 are displayed in green, and FPR675-labeled dextran sulfate-based

nanoprobes (DSNPs) are displayed in red. The scale bar indicates 50 μm.

List of tables

Chapter 1

Introduction

1.1. Cancer

Cancer is a serious global health challenge.[1] According to the World Health Organization, cancer is a leading cause of death worldwide, accounting for 8.2 million deaths in 2012, and this number is predicted to increase to 12 million by 2030.[2, 3] Most cancer occurs because of abnormal cell division induced by complex interactions between the host genome and carcinogens. These abnormalities in cell division often lead to the formation of tissue mass called tumors. Tumors may be classified as either malignant (cancerous) or benign (noncancerous). A malignant tumor is capable of invading normal tissues and organs adjacent to the location of the primary tumor, thereby impeding the normal function of the body's system. However, cancer cells detach from a primary tumor and spread through the blood circulation and lymphatic system to distant spots in the body, developing new tumors; this process is called metastasis. Eventually, malignant tumors can destroy various organs in the body, leading to death.

Cancer research over the past few decades has been focused on understanding the transformation of normal cells to cancer cells. However, scientists spent little time researching other types of cells present within a tumor. Although genetic and epigenetic alterations in tumor cells are prerequisites for the malignant process, they are not sufficient to offer tumor cells with malignant properties. Complex interactions between different host cell types and cancer cells form a dynamic tumor microenvironment that closely interacts with cancer cells.[4] Many lines of evidence

support that the intimate association between cancer cells and their tumor microenvironment deeply influences cancer development and progression and affects many hallmarks of cancer.[5-7] Therefore, attention needs to be paid to the tumor microenvironment as well as cancer cells in the fight against cancers.

1.2. Molecular imaging in cancer management

Molecular imaging enables the visualization and characterization of cancer-specific events at the cellular and molecular levels in living systems. Many features of the malignant process can be visualized with molecular imaging, involving changes in gene expression, the neovasculature of angiogenesis, the expression of receptors on cancer cell surfaces, and changes of extracellular matrix or stromal cells in the tumor microenvironment. Molecular imaging has several advantages for cancer management.[8]

First, it could facilitate the detection of cancerous lesions at an earlier stage. Detecting cancer at an earlier stage is one of the most significant strategies to reduce both mortality and cancer incidence worldwide.[1] Since molecular or cellular changes often happen a long time before any signs of structural, functional, anatomical changes become evident, molecular imaging can provide additional information about molecular and cellular events associated with diseases and facilitate earlier diagnosis in the course of a disease. In cancer, the detection and treatment of cancer before metastasis enhance one's possibility of survival; when

detected at an early stage, cancer treatment is simpler and more effective. For example, the 5-year survival rate for patients who are diagnosed with breast cancer that has not yet spread from the breast tissue is approximately 99%. However, the survival rate for patients whose cancer has already spread to lymph nodes is approximately 84%, and that for patents whose cancer has spread to distant parts of the body including the liver, lungs or bones decreases to 23%.[9] Moreover, this detection can non-invasively be achieved without biopsies or surgical procedures, which allows the repetitive measurement of the same living subject at different time points.

Second, molecular imaging techniques could aid surgeons in delineating the margins of a tumor mass for tumor resection and appropriate biopsy. Successful surgical procedures depend on detecting the accurate and rapid localization of tumor tissues.[10] The intra-operative detection of tumor lesions in real-time can allow complete tumor resection while preserving important structures, improving treatment outcome and reducing healthcare costs.[11]

Third, molecular imaging techniques enable the real-time validation of therapy.[12] Real-time, noninvasive monitoring can allow clinicians to identify positive or negative patient response to the current therapeutic regimen and to guide decisions on the continuation or alteration of the regimen before evaluating traditional treatment efficacy, such as a change in tumor size. For example, clinicians can switch to other therapeutic options, or they can adjust the therapeutic dose for non-responders to the current therapeutic regimen, while continuing the therapy for good

responders. This is especially significant because treatment using monoclonal antibodies, such as cetuximab and trastuzumab is increasing.[13]

Finally, molecular imaging can increase the knowledge of the role of cancer-related components throughout the course of the disease. Such knowledge can broaden understanding of how distinct components can be under control, contributing to the creation of more effective treatment against cancer. In addition, this can lead to the development of more advanced probes and imaging methods to image characteristics and activities of distinct components.

1.3. Cancer imaging modalities

Presently, various imaging modalities are available for diagnosis, staging, and treatment of cancer: optical imaging, ultrasound (US) imaging, magnetic resonance (MR) imaging, computed tomography (CT) and nuclear imaging (single photon emission computed tomography (SPECT), and positron emission tomography (PET)). These modalities can be broadly separated into primarily molecular imaging modalities and primarily morphological/anatomical imaging modalities.[14] The former, which are characterized by high sensitivity, include optical imaging and PET/SPECT; on the other hand, the latter, which are featured by high spatial resolution, include CT, US, and MR.[14, 15] However, those imaging modalities have various advantages and disadvantages in terms of sensitivity and spatial/depth

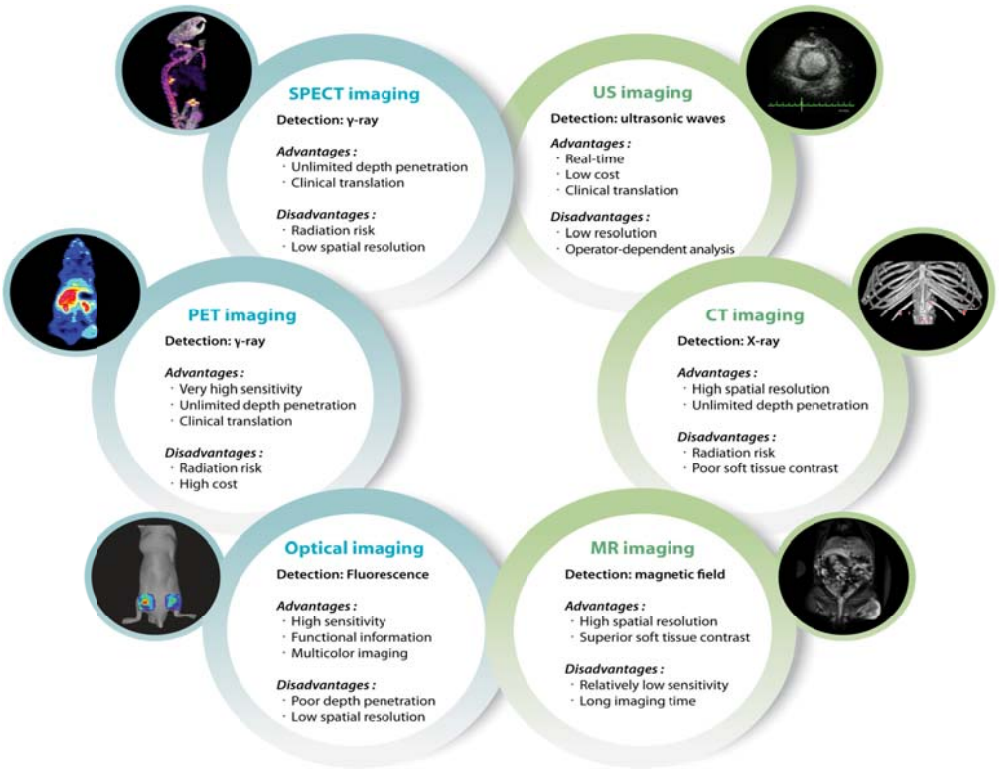

Figure 1.1. Characteristics of cancer imaging modalities

resolution (Figure 1.1).

Computed tomography

CT is a widely performed modality in diagnosis and staging of nearly all cancer, and also the initial comprehensive imaging performed in patients with suspected cancer.[16] CT is used to detect different densities of X-ray absorption in different tissues when x-rays pass through a patient's body.[17] It has an inherent high-contrast resolution, which allows the discrimination of tiny differences between body tissues with various physical densities. However, the soft tissue contrast of CT is low, which could cause difficulties when detecting cancer invasion into surrounding structures or distant metastases.[18] In addition, exposure to ionizing radiation during a CT scan is the most serious weakness, because it could harm patients, specifically to children. However, CT has still many advantages, therefore, it has frequently been utilized in clinical diagnosis.

Magnetic resonance imaging

MR imaging displays great promise for detecting cancers and for defining the extent of a cancer's spread. MR imaging produces anatomical images of organs with surpassed soft tissue differentiation compared to any other imaging method, which enables accurate cancer detection and local staging. MR imaging detects the

spin of the hydrogen nucleus, which are predominantly contained in the water and fat of the human body. During the MRI examination, nuclear spins are subjected to a selective radio-frequency pulse, and then nuclei in the excited state will "relax" and return to their initial state. This process, called relaxation, involves spin-lattice relaxation time (T_1) and spin-spin relaxation time (T_2), both of which can be used to produce an MR image capable of distinguishing between various types of tissue. MRI examination is expensive and time-consuming, but MR imaging is advantageous in high contrast resolution between different soft tissue types and superior three-dimensional spatial resolution.

Nuclear imaging

Nuclear imaging modalities, including PET and SPECT, remotely visualize molecular events in cancer progression by observing radioactive emission from targeted radiolabelled probes.[19, 20] They provide quantitative images of the three-dimensional distribution of injected short-lived radiolabelled probes *in vivo*. Radiolabelled probes can be constructed using monoclonal antibodies against cancer cell-specific antigen, which has been widely used in imaging of several cancer types. Common positron-emitting radioisotopes for PET involve ^{11}C, ^{18}F, ^{13}N, ^{15}O, and ^{124}I, while common γ-emitting isotopes for SPECT include ^{99m}Tc and ^{111}In.[21] Cancer imaging by PET with the tracer ^{18}F-fluorodeoxyglucose (^{18}F-FDG) is commonly utilized in clinics, which is based on increased uptake of ^{18}F-FDG in metabolically active proliferative tissue such as cancer. Some studies reported that

PET is useful in finding small metastases that is missed by CT.[16] The sensitivity of PET is particularly superior to that of SPECT. On the other hand, SPECT allows the simultaneous measurement of different radioisotopes labeled with multiple compounds.

Ultrasound imaging

US imaging is a well-established imaging technique used in clinical settings for diagnosing several cancer types such as breast, prostate, and pancreatic cancer. US enables demonstration of zonal anatomy and determination of cancer size. US imaging utilizes high-frequency ultrasound waves. The ultrasound waves transmitted from a transducer are reflected back by the target organs in a patient's body, endowing reconstructed images of scanned areas. US imaging is mainly a tool used to provide highly detailed, real-time visualization of anatomy and physiology in clinical diagnosis. US imaging has benefits in that it is safe, fast, and inexpensive. However, the ultrasound waves are disrupted by gas or air; US has limitations in visualizing air-filled bowel or gas-containing organs like the lungs. In addition, US has difficulties in penetrating bone; therefore, US imaging cannot see the interior of bony structures. Recently, contrast-enhanced US with micro/nanobubbles has been researched to achieve high sensitivity in the detection of cancer foci.[22]

Optical imaging

Optical imaging based on bioluminescence or fluorescence is a sensitive imaging technology for diagnosing and staging of cancer and follow-up care after cancer treatment. Optical imaging used light to probe molecular targets and gene reporters in the context of cancer in a living subject. Bioluminescence imaging measures the light emitted by the chemical reaction between a luciferase enzyme and luciferin. In addition, fluorescence imaging detects the light emitted from a fluorophore at a particular wavelength after excitation light typically illuminates the area of interest. The advantages of optical imaging include sensitivity, real-time and convenient use, and non-ionization safety. However, it has a low penetration depth due to strong absorption in the visible light region. This is the main reason that near-infrared (NIR) fluorescent light (λ=650-900 nm) is used, especially in *in vivo* imaging. The use of fluorophores within this range allows for low levels of interfering autofluorescence and high tissue penetration (up to several centimeters deep) in living tissues, providing enhanced image contrast with high sensitivity. Because of the availability of multicolor imaging involving different fluorophores, optical imaging would be very popular and powerful when capturing the various biological status of different tissues with regard to cancer heterogeneity.[23] The use of optical imaging can be also applied for delineating the margins of a tumor mass for tumor resection and appropriate biopsy as well as screening for cancer.

No single imaging modality simultaneously provides sufficient sensitivity and temporal and spatial resolution for cancer diagnosis. Hence, integrated molecular/ anatomical systems have recently been exploited to combine the strengths of

individual imaging modalities. For example, PET imaging provides high sensitivity, but not anatomical information. Hence, PET imaging has been integrated with CT which allows anatomical information with high spatial resolution. Indeed, an integrated PET/CT system is commercially available now and is routinely utilized for diagnosing and staging of cancer, and follow-up care of cancer treatment in clinical settings.[24]

1.4. Targets of cancer cells for cancer imaging

Some cancer cells produce over-expressed receptors on their surface compared to normal cells.[25] For several decades, over-expressed receptors on the surface of cancer cells have been researched as primary targets for tumor imaging and therapy. These include human epidermal receptors, transferrin receptors, and folate receptors.[3]

Epidermal growth factor receptor

Epidermal growth factor receptor (EGFR) belongs to the ErbB family of receptor tyrosine kinases.[26, 27] EGFR is known to activate multiple cell signaling pathways that promote cell growth in response to the binding of its specific ligands, including transforming growth factor-α (TGF-α) and epidermal growth factor (EGF). These ligands bind directly to EGFR; therefore, these ligands can act as targeting moieties for EGFR. EGFR is shown to be overexpressed in many types of cancers, including

non-small cell lung cancer, skin cancer, breast cancer, small cell carcinoma of head and neck, and prostate cancer. In fact, one-third of all solid tumors is known to express EGFR.[28] The overexpression of EGFR is shown to be correlated with poor prognosis and increased metastatic potential.

Transferrin receptors

Transferrin receptors are membrane-associated glycoproteins that function in the regulation of cell growth and the cellular uptake of iron and by binding with transferrin.[29] Iron is an essential cofactor of various proteins involved in cellular processes such as metabolism and DNA synthesis. When binding to the transferrin receptors on the plasma memebrane, the transferrin is internalized via receptor-mediated endocytosis, and trasferrin receptors recycle onto the cell surface. The transferrin receptors are shown to be overexpressed in many types of cancers, including glioma, bladder-trasitional cell carcinomas, lung adenocarcinoma, breast cancer, and chronic lymphocytic leukemia. Transferrin receptors are very attractive targets for cancer targeting because they are known to be overexpressed on drug-resistant or metastatic cells.[30]

Folate receptors

Folate receptors, glycosylphosphatidylinositol-anchored cell surface receptors, are one of the most widely investigated targets for cancer targeting.[31] Folate receptors

facilitate the transportation of folate into the cytoplasm of cells. Folate is necessary for essential cell functioning because it is involved in the synthesis of pyrimidines and purines. Folate receptors are expressed in nearly all cells for normal cell division as well as DNA replication. However, they are expressed in a much greater amount in tumor cells than nontumor cells. In particular, they are highly overexpressed on the vast majority of cancers including ovarian, brain, lung, and breast cancers. Folate is widely used as a targeting ligand for folate receptors because of its low cost, high binding affinity, high stability in blood, and low toxicity.[32]

1.5. Targets of the tumor microenvironment for cancer imaging

In recent years, it has become obvious that other components of tumors, such as non-tumor cells (endothelial cells, fibroblasts), connective tissue, extracellular matrix (ECM), immune cells, and soluble factors play fundamental roles in tumor development and progression.[33] These components are collectively known as the tumor microenvironment. New strategies for tumor imaging or therapy have been established by targeting the tumor microenvironment instead of targeting tumor cells.[34] Unlike tumor cells, cellular components in the tumor microenvironment are genetically stable, which makes the tumor microenvironment attractive therapeutic targets because of the reduced risk of drug resistance and tumor recurrence.[35, 36]

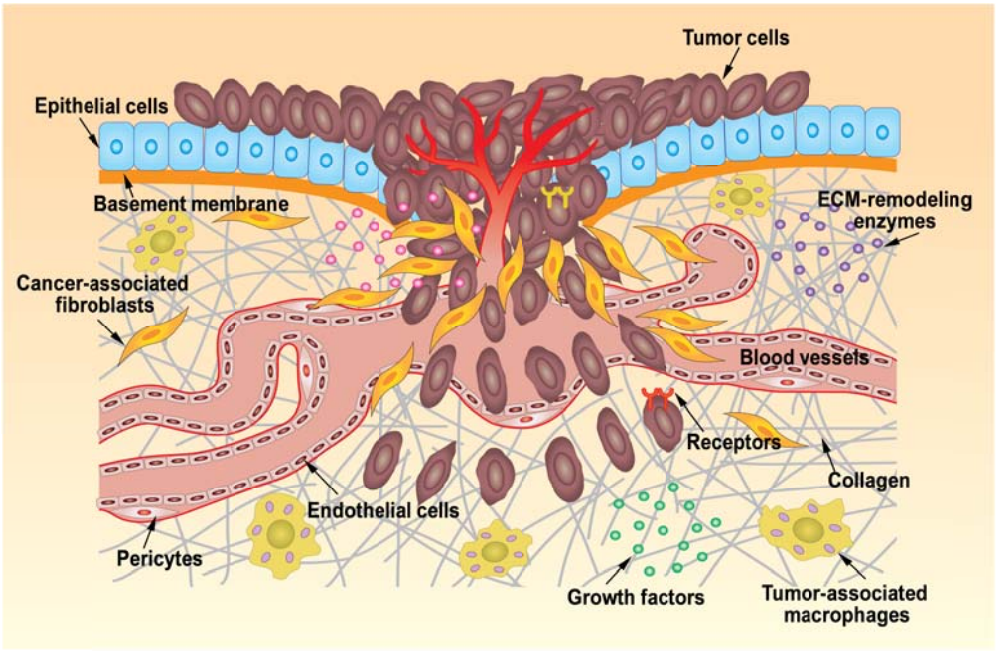

Figure 1.2. Schematic illustration of the major components in the tumor microenvironment.

Targets of the tumor microenvironment for tumor imaging can be grouped into two categories: cellular components and non-cellular components.

1.5.1. Cellular components of the tumor microenvironment

Blood-vessel cells such endothelial cells and pericytes, CAFs, and immune cells are key players among the cellular components of the tumor microenvironment.

Blood vessel cells

Angiogenesis-associated targeting has become attractive for cancer imaging and therapy. Blood vessels promote tumor growth by delivering sufficient oxygen and nutrients. In fact, most tumors cannot expand a few mm^3 in volume and maintain clinically silent in the absence of blood-vessels.[37] Tumor angiogenesis is the multi-step process of new blood vessels from pre-existing vasculature, which is mainly mediated by the invasion, migration, and proliferation of endothelial cells. Host cells and tumors secrete a variety of pro-angiogenic growth factors and anti-angiogenic growth factors, which could bind to their receptors on the surface of endothelial cells. These specific bindings between growth factors and their receptors mediate and regulate angiogenesis. Pericytes are contractile cells that surround the endothelial cells of blood vessels, which provide vascular stability and mediate endothelial proliferation. Tumor blood vessels are known to be leaky and irregularly dilated, unlike normal blood vessels. These properties of tumor blood vessels are the

primary reason to utilize nanoparticles (NPs) for tumor targeting. NPs can easily extravasate from blood vessels into tumor tissues because of leaky and irregularly dilated blood vessels at tumor sites, and they can also be retained at tumor sites owing to poor lymphatic drainage. This phenomenon of the selective accumulation of NPs near tumor tissues is termed the enhanced permeability and retention (EPR) effect.

Cancer-associated fibroblasts

CAFs comprise a majority of the cells in tumor stroma. They can derive from normal fibroblasts as well as from excessive progenitor cells including bone marrow-derived cells, endothelial cells through the process of endothelial-to-mesenchymal transition, and cancer cells through the process of epithelial-to-mesenchymal transition. CAFs produce a series of growth factors such as eptidermal growth factor (EGF) and vascular endothelial growth factor (VEGF), cytokines such as interleukins and proteases such as matrix metalloproteinases (MMPs), which sustain cancer progression.[38] In addition, they synthesize a diversity of ECM components including fibronectin, tenascin, and collagens to regulate tumor cell proliferation, angiogenesis, and cancer metastasis. Increasing evidence indicates that interactions between tumor cells and CAFs are essential for cancer development and progression, which makes CAFs attractive targets for tumor imaging and therapy.[39, 40]

Immune cells

Immune cells, including lymphocytes, macrophages, natural killer cells, and dendritic cells are important for tumor suppression. However, diverse suppressor cells such as TAMs, regulatory T cells, and myeloid-derived suppressor cells are recruited to the tumor microenvironment.[41] These cells negatively regulate immune response, helping tumor cells avoid the attack by immune effector cells.[42] Accumulated evidence has demonstrated that tumor-associated immune cells can secret cytokines, growth factors, chemokines, and matrix-degrading proteases, such as MMPs, cathepsin proteases, and heparanses, which provide favorable conditions for tumor cell proliferation, angiogenesis, and cancer metastasis. By producing these cytokines, growth factors, and proteases, immune cells in the tumor microenvironment work as essential mediators in sustaining cancer progression.

1.5.2. Non-cellular components of the tumor microenvironment

Extracellular matrix

The ECM, a multifunctional interstitial matrix, consists mainly of collagens, elastin, laminin, fibronectin, and proteoglycans. Because it has an important role in conferring shape and stability to tissues, ECM ubiquitously exists in human tissues. However, its composition can vary according to its location and function.[43] In cancer, the ECM is not a static structure to maintain tissue morphology and

constantly undergoes remodeling. Highly dynamic ECM can result from the modified composition or density of the ECM. The ECM in tumor tissues commonly includes a much denser and thicker network consisting of different composition compared to normal tissues.[44] Specifically, the ECM is typically deregulated and becomes abnormal, which directly influences cancer progression by encouraging transformation and metastasis.[45] In addition, abnormal ECM also deregulates surrounding stromal cells and promotes tumor-associated angiogenesis, which continuously creates favorable conditions to accelerate tumor malignancy and metastatic progression. Because the ECM is not enclosed by a plasma membrane, imaging probes or drugs have essentially unlimited access to these areas.[46] This can be the most crucial benefit of approaches to target ECM.

Matrix-degrading enzymes

Matrix-degrading enzymes including MMPs, cysteines, plasminogen activators, and other hydrolases are over-produced by tumor cells, CAFs, or TAMs.[47] MMPs are a group of over 20 enzymes facilitating the degradation of the ECM and the basement membrane. By degrading the ECM, especially type IV collagen and laminin, MMPs enable the invasion and migration of tumor cells as well as endothelial cells and immune cells to surrounding tissues. Besides degradation of the ECM, MMPs can promote the release of angiogenic cytokines, such as VEGF, and the homing of bone marrow-derived circulating endothelial progenitor cells, which contributes to successful angiogenesis.[48] Cathepsins are a group of 11

enzymes belonging to the papain family of cysteine proteases.[49] Among various cathepsins, cathepsin B is known to play an important role in the growth, migration, invasion, and metastasis of various cancers.[50, 51] In addition, some reports on solid tumors have shown a correlation between the expression of cathepsin B and tumor progression/clinical outcomes in patients.[52]

Soluble factors

A variety of soluble factors are produced and secreted by stromal and tumor cells in the tumor microenvironment.[53] These over-expressed soluble factors engage in a wide range of signaling pathways and influence tumor behavior upon binding to their receptors. For instance, VEGF plays a significant role in initiating tumor angiogenesis.[54, 55] VEGF potentiates microvascular hyperpermeability which enables to both precede and accompany angiogenesis by stimulating an influx of endothelial cells, fibroblasts, and inflammatory cells. Upon binding to its specific receptor, moreover, VEGF promotes the expression of Bcl-2 and signaling through chemokines (CXCL1 and CXCL8), resulting in the proliferation and migration of endothelial cells and the formation of new blood vessels. Activated fibroblasts that encourage a microenvironment conducive to tumor progression are mediated by various soluble growth factors including fibroblast growth factor-2, platelet-derived growth factor, and transforming growth factor-β (TGF- β).[56] Tumor cells may alter their stroma by a wide range of soluble factors.[57]

Integrins

The tumor microenvironment includes a large group of cell adhesion receptors called integrins, which are involved in cell-cell and cell-ECM interactions.[58] Intergrins consist of different combinations of two transmembrane glycoprotein (α and β) subunits and are overexpressed in various cell types of tumors. For example, $\alpha_v\beta_3$ integrin is one of extensively investigated targets for tumor targeting. To target $\alpha_v\beta_3$ integrin, the peptide possessing high affinity for $\alpha_v\beta_3$ integrin, arginine-glycine-aspartic acid (RGD) sequence, was widely utilized.[59] $\alpha_v\beta_3$ integrin is upregulated on proliferating tumor cells and activated endothelial cells, but is minimally expressed in cells in most normal organ systems and in resting or normal endothelial cells. $\alpha_v\beta_3$ integrin can influence the survival, migration, and invasion of tumor cells, mediating interaction between tumor cells and ECM proteins.

1.6. Scope of this thesis

Even with the recent advances in diagnosis and management of many cancers, cancer modality rates still remain high. By employing a more sensitive and more specific imaging technique, earlier diagnosis and more accurate assessment of prognostic factors of cancer are possible. It ultimately improves patient care. In particular, for the imaging to be more effective, cancer should be considered as a multi-factorial disease, resulted from the combined influence of many genetic factors acting in concert with the environmental change. The combination of

information using results from multiple target-specific molecular imaging will improve the sensitivity and specificity in the diagnostic process of cancer.

This dissertation seeks to visualize the key components of the evolving cancer burden during cancer development and progression. Various key components of the evolving cancer burden were selected: the over-produced protease, the over-expressed receptors on the surface of cancer cells, the tumor-associated macrophages in the tumor microenvironment, the extracellular matrix-remodeling enzymes, and the modified tumor tissues. To visualize specific components, new imaging probes were developed based on appropriate materials targeting the cancer-specific components – a peptide, a protein, a commercial drug, a gold nanoparticle, or a polymer. Although this work focuses on applying the targeting abilities of the probes to visualize the targets, the specific abilities developed here offer new opportunities as a platform for therapeutic use. I performed the cancer-specific imaging with hopes to translate this work to a clinical setting and help patients in need of personalized treatment options.

The specific goals of this thesis are as follows:

· To develop peptide-based activatable probes for non-invasive imaging of metastasis

· To develop protein-based activatable probes with potential use for therapeutic monitoring

· To visualize the infiltration of tumor-associated macrophages with polymer-based

probes

· To detect ECM-modifying enzymes with gold nanoparticle-based probes

· To develop a rapid method for determining tumor mass in the operating room

1.7. References

1. Hellebust, A.; Richards-Kortum, R. *Nanomedicine* **2012**, *7*, 429.

2. "Lastest world cancer statistics", International Agency for Research on Cancer, last revised Dec 12, 2013, http://www.iarc.fr/en/media-centre/pr/2013/pdfs/pr223_E.pdf

3. Barreto, J. A.; O'Malley, W.; Kubeil, M.; Graham, B.; Stephan, H.; Spiccia, L. *Advanced Materials* **2011**, *23*, H18.

4. Fang, H.; DeClerck, Y. A. *Cancer Research* **2013**, *73*, 4965.

5. Liotta, L. A.; Kohn, E. C. *Nature* **2001**, *411*, 375.

6. Bobrie, A.; Krumeich, S.; Reyal, F.; Recchi, C.; Moita, L. F.; Seabra, M. C.; Ostrowski, M.; Théry, C. *Cancer Research* **2012**, *72*, 4920.

7. Coulouarn, C.; Corlu, A.; Glaise, D.; Guénon, I.; Thorgeirsson, S. S.; Clément, B. *Cancer Research* **2012**, *72*, 2533.

8. Li, C. *Nature Materials* **2014**, *13*, 110.

9. "Breast cancer survival rates by stage", American Cancer Society, last revised Jan 31, 2014, http://www.cancer.org/cancer/breastcancer/detailedguide/breast-cancer-survival-by-stage.

10. Urano, Y.; Sakabe, M.; Kosaka, N.; Ogawa, M.; Mitsunaga, M.; Asanuma, D.; Kamiya, M.; Young, M. R.; Nagano, T.; Choyke, P. L.; Kobayashi, H. *Science Translational Medicine* **2011**, *3*, 110.

11. Nguyen, Q. T.; Tsien, R. Y.*Nature Reviews Cancer* **2013**, *13*, 653.

12. Ryu, J. H.; Koo, H.; Sun, I.-C.; Yuk, S. H.; Choi, K.; Kim, K.; Kwon, I. C.

Advanced Drug Delivery Reviews **2012**, *64*, 1447.

13. Kumar, S.; Richards-Kortum, R. *Nanomedicine* **2006**, *1*, 23.

14. Willmann, J. K.; van Bruggen, N.; Dinkelborg, L. M.; Gambhir, S. S. *Nature Reviews Drug Discovery* **2008**, *7*, 591.

15. Huang, Y.; He, S.; Cao, W.; Cai, K.; Liang, X.-J. *Nanoscale* **2012**, *4*, 6135.

16. Tummala, P.; Junaidi, O.; Agarwal, B. *Journal of Gastrointestinal Oncology* **2011**, *2*, 168.

17. Brenner, D. J.; Hall, E. J. *New England Journal of Medicine* **2007**, *357*, 2277.

18. Agrawal, P.; Strijkers, G. J.; Nicolay, K. *Advanced Drug Delivery Reviews* **2010**, *62*, 42.

19. Gambhir, S. S. *Nature Reviews Cancer* **2002**, *2*, 683.

20. Phelps, M. E. *Proceedings of the National Academy of Sciences of the United States of America* **2000**, *97*, 9226.

21. Wang, D. S.; Dake, M. D; Park, J. M.; Kuo, M. D. *Journal of Vascular and Interventional Radiology* **2006**, *17*, 1405.

22. Min, H. S.; Son, S.; Lee, T. W.; Koo, H.; Yoon, H. Y.; Na, J. H.; Choi, Y.; Park, J. H.; Lee, J.; Han, M. H.; Park, R. –W.; Kim, I. –S.; Jeong, S. Y.; Rhee, K.; Kim, S. H.; Kwon, I. C.; Kim, K. *Advanced Functional Materials* **2013**, *23*, 5518.

23. Kobayashi, H.; Longmire, M. R.; Choyke, P. L. *Advanced Drug Delivery Reviews* **2013**, *65*, 1112.

24. Kievit, F. M.; Zhang, M. *Advanced Materials* **2011**, *23*, H217.

25. Agarwal, A.; Saraf, S.; Asthana, A.; Gupta, U.; Gajbhiye, V.; Jain, N. K. *International Journal of Pharmaceutics* **2008**, *350*, 3.

26. Kari, C.; Chan, T. O.; Rocha de Quadros, M.; Rodeck, U. *Cancer Research* **2003**, *63*, 1.

27. Ke, S.; Wen, X.; Gurfinkel, M.; Charnsangavej, C.; Wallace, S.; Sevick-Muraca, E. M.; Li, C. *Cancer Research* **2003**, *63*, 7870.

28. Novak, H.; Noy, R.; Oved, K.; Segal, D.; Wels, W. S.; Reiter, Y. *International Journal of Cancer* **2007**, *120*, 329.

29. Kawamoto, M.; Horibe, T.; Kohno, M.; Kawakami, K. *BMC Cancer* **2011**, *11*, 359.

30. Singh, M. *Current Pharmaceutical Design* **1999**, *5*,443.

31. Byrne, J. D.; Betancourt, T.; Brannon-Peppas, L. *Advanced Drug Delivery Reviews* **2008**, *60*, 1615

32. Low, P. S.; Antony, A. C. *Advanced Drug Delivery Reviews* **2004**, *56*, 1055.

33. Witz, I. P.; Levy-Nissenbaum, O. *Cancer Letter* **2006**, *242*, 1.

34. Ji, T.; Zhao, Y.; Ding, Y.; Nie, G. *Advanced Materials* **2013**, *25*, 3508.

35. Zhao G, R. B. *International Journal of Nanomedicine* **2013**, *8*, 61.

36. Quail, D. F.; Joyce, J. A. *Nature Medicine* **2013**, *19*, 1423.

37. Lorusso, G.; Rüegg, C. *Histochemistry and Cell Biology* **2008**, *130*, 1091.

38. Cirri P, C. P. *American Journal of Cancer Research* **2011**, *1*, 482.

39. Kalluri, R.; Zeisberg, M. *Nature Reviews Cancer* **2006**, *6*, 392.

40. Zhi, K.; Shen, X.; Zhang, H.; Bi, J. *Journal of Experimental & Clinical Cancer Research* **2010**, *29*, 66.

41. Park, Y.-J.; Song, B.; Kim, Y.-S.; Kim, E.-K.; Lee, J.-M.; Lee, G.-E.; Kim, J.-O.; Kim, Y.-J.; Chang, W.-S.; Kang, C.-Y. *Cancer Research* **2013**, *73*, 5669.

42. Sounni, N. E.; Noel, A. *Clinical Chemistry* **2013**, *59*, 85.

43. Del Vecchio S, Z. A.; Iommelli, F.; Lettieri, A.; Brunetti, A.; Salvatore, M. *The Quarterly Journal of Nuclear Medicine and Molecular Imaging* **2010**, *54*, 249.

44. Heldin, C.-H.; Rubin, K.; Pietras, K.; Ostman, A. *Nature Reviews Cancer* **2004**, *4*, 806.

45. Lu, P.; Weaver, V. M.; Werb, Z. *The Journal of Cell Biology* **2012**, *196*, 395.

46. Kanapathipillai, M.; Mammoto, A.; Mammoto, T.; Kang, J. H.; Jiang, E.; Ghosh,

K.; Korin, N.; Gibbs, A.; Mannix, R.; Ingber, D. E. *Nano Letters* **2012**, *12*, 3213.

47. Weissleder, R.; Pittet, M. J. *Nature* **2008**, *452*, 580.

48. Johnson, C.; Sung, H.-J.; Lessner, S. M.; Fini, M. E.; Galis, Z. S. *Circulation Research* **2004**, *94*, 262.

49. Mohamed, M. M.; Sloane, B. F. *Nature Reviews Cancer* **2006**, *6*, 764.

50. Hulkower, K. I.; Butler, C. C.; Linebaugh, B. E.; Klaus, J. L.; Keppler, D.; Giranda, V. L.; Sloane, B. F. *European Journal of Biochemistry.* **2000,** *267*, 4165.

51. Lopez-Otin, C.; Matrisian, L. M. *Nature Reviews Cancer* **2007**, *7*, 800.

52. Sinha, A. A.; Jamuar, M. P.; Wilson, M. J.; Rozhin, J.; Sloane, B. F. *The Prostate* **2001**, *49*, 172.

53. Sung, S.-Y.; Hsieh, C.-L.; Wu, D.; Chung, L. W. K.; Johnstone, P. A. S. *Current Problems in Cancer* **2007**, *31*, 36.

54. Hoeben, A.; Landuyt, B.; Highley, M. S.; Wildiers, H.; Van Oosterom, A. T.; De Bruijn, E. A. *Pharmacological Reviews* **2004**, *56*, 549.

55. Ferrara, N.; Gerber, H.-P.; LeCouter, J. *Nature Medicine* **2003**, *9*, 669.

56. Brennen, W. N.; Isaacs, J. T.; Denmeade, S. R. *Molecular Cancer Therapeutics* **2012**, *11*, 257.

57. Koontongkaew, S. *Journal of Cancer* **2013**, *4*, 66.

58. Alphonso A, A. S. *Neoplasia* **2009**, *11*, 1264.

59. Akers, W. J.; Zhang, Z.; Berezin, M.; Ye, Y.; Agee, A.; Guo, K.; Fuhrhop, R. W.; Wickline, S. A.; Lanza, G. M.; Achilefu, S. *Nanomedicine* **2010**, *5*, 715.

Chapter 2

Imaging of cathepsin B activity with activatable nanoprobes

2.1. Introduction

An important determinant of cancer patients' treatment is the absence or presence of metastasis.[1] The progression of cancer from a primary tumor to metastasis occurs at widely different rates for various tumors.[2] Though the rate of this progression may be dissimilar among tumors, many tumors undergo a series of steps that lead to cellular- or molecular level changes prior to or during metastasis. Identifying molecular changes prior to or during metastasis could help in diagnosing early metastases, contributing to the early initiation of therapy and ultimately the improved survival of patients. Most studies have demonstrated the characterization of molecular changes *in vitro*; however, few researchers have attempted to visualize molecular changes *in vivo* for metastasis.[3] Therefore, there is an urgent need for imaging techniques that are capable of depicting metastases *in vivo* by detecting molecular changes associated with metastasis.

High levels of secretion of cathepsin B (CB) into the pericellular region are important for cancer invasion and metastasis.[4, 5] In the metastatic process, the proteolytic degradation of extracellular matrices (ECMs) is required because malignant cancer cells invade basement membranes, spread to distant sites, and subsequently reinvade and grow at new location in the body. Various proteases have been implicated in cancer invasion and metastasis, including cathepsins, plasminogen activators (PA), and matrix metalloproteinases (MMPs). CB activates PA, which then converts plasminogen to plasmin. Plasmin in turn activates latent

MMPs, turning them into activated MMPs. That is, CB is highly expressed in the early stage of the proteolytic cascade involved in cancer invasion and metastasis.[6] In addition, active forms of CB normally remain in the lysosomal compartments inside mammalian cells; however, as cells obtain metastatic potential, CB is highly expressed in the pericellular region.[7] Therefore, pericellular CB activity detection can facilitate the early diagnosis of metastases.

CB activity detection could be a favorable approach to diagnose metastases. A CB-sensitive nanoprobe (CB-CNP) consisting of CB-sensitive fluorescence peptide probes conjugated onto the surface of tumor-targeting glycol chitosan nanoparticles (CNPs) was developed to detect the activity of CB.[8] In addition, three metastatic mouse models were induced, including 4T1-luc2 liver metastases, RFP-B16F10 lung metastases, and HT1080 peritoneal metastases. CB expression in various tumor models was confirmed by immunohistochemistry (IHC) or Western blot. Importantly, the potential use of intravenously injected CB-CNPs for discriminating metastases *in vivo* was investigated (Figure 2.1). The CB-CNP's *in vivo* specificity was also evaluated by treating CB inhibitor in an HT29 subcutaneous tumor mouse model. Then, CB-CNP's detection sensitivity was compared with that of CNP-Cy5.5 without CB-sensitive moiety in an HT29 liver tumor model.

2.2. Experimental section

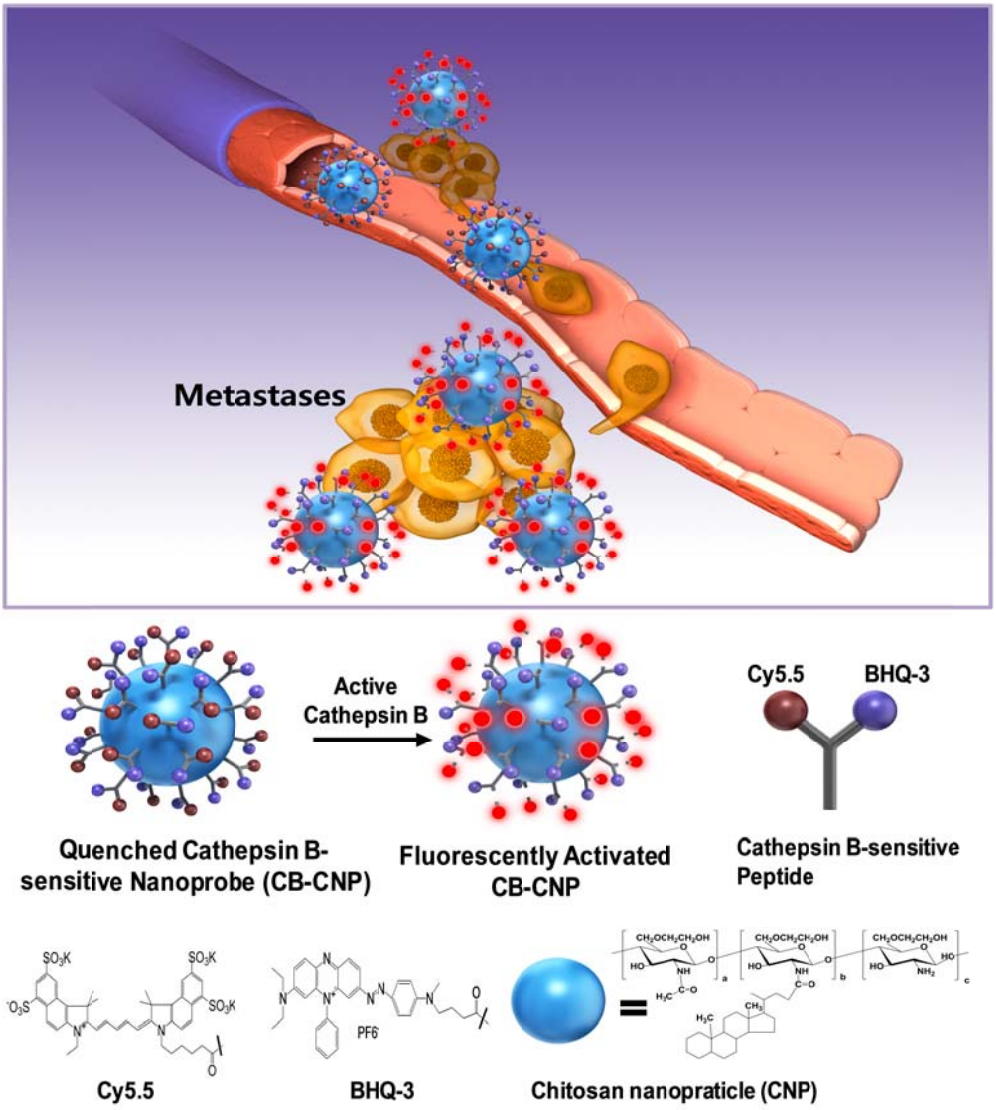

Figure 2.1. Schematic presentation describing that cathepsin B (CB)-sensitive nanoprobe (CB-CNP) can be utilized for depicting metastases. Illustration for activation of CB-CNP and chemical structures of Cy5.5, BHQ-3, and glycol chitosan nanoparticles (CNPs). Self-quenched CB-sensitive fluorescence peptide probes including a NIR dye (Cy5.5) and a quencher (BHQ-3), were covalently conjugated to CNP, resulting in the CB-CNP. CB-CNP produced intense fluorescence signals due to the elevated CB activity in metastatic tumor tissues.

2.2.1. Materials

Cy5.5 N-hydroxysuccinamide (NHS) ester (Cy5.5-NHS, excitation and emission maximum of 675 nm and 693 nm, respectively) was purchased from GE Healthcare (Piscataway, NJ) and black hole quencher 3 NHS ester (BHQ3-NHS, absorbance maximum of 672 nm) was obtained from Biosearch Technologies, Inc. (Novato, CA). CB, cathepsin D and cathepsin L enzymes were purchased from R&D Systems, Inc. (Minneapolis, MN). Cathepsin inhibitor (Z-Phe-Ala-FMK) was purchased from Calbiochem (San Diego, CA). Monoclonal mouse anti-CB IgG and goat anti-mouse IgG-FITC were purchased from Abcam (Cambridge, MA) and Santa Cruz Biotechnology Inc. (Santa Cruz, CA), respectively. Fetal bovine serum (FBS) was purchased from Invitrogen Canada (Burlington, ON, Canada), and RPMI 1640 medium and Dulbecco's modification of Eagle's medium (DMEM) were obtained from Gibco (Grand Island, NY). For Western blot, anti-CB and a horseradish peroxidase-conjugated anti-mouse antibody were purchased from Calbiochem and Santa Cruz Biotechnology, respectively.

2.2.2. Preparation of the cathepsin B-sensitive nanoprobe

The CB-peptide probe was developed by linking a near infrared (NIR) fluorophore (Cy5.5) and a dark quencher (BHQ-3) to a CB-sensitive substrate peptide (Gly-*Arg*-*Arg*-Gly-Lys-Gly-Gly; the recognition site is italicized and the cleavage site was between Arg and Gly).[8] Peptides were synthesized using a standard solid-phase

peptide synthesis method (Peptron, Daejeon, Korea). Next, the CB-peptide probes were chemically linked onto the surface of the self-assembled chitosan nanoparticles (CNPs) to develop the cathepsin B-sensitive chitosan nanoprobe (CB-CNP). Briefly, glycol chitosan was conjugated with hydrophobic 5β-cholanic acid (150 ± 5 molecules of 5β-cholanic acid per glycol chitosan).[9] The glycol chitosan conjugated with 5β-cholanic acid (22 nmol) was dispersed in phosphate-buffered saline (PBS, 7 ml) using a probe-type sonicator (90 W, 5 min, Ultrasonic Processor, GEX-600; Sonics & Materials, Newtown, CT), resulting in CNP solution. The CB-peptide probe (1.2 μmol) was dissolved in a co-solvent of dimethyl sulfoxide (DMSO) and PBS (1:1, v/v; 200 μl), and mixed with 1-ethyl-3-(3-dimethylaminopropyl)carbodiimide (EDC) and sulfo-NHS dissolved in PBS (100 μl) for 15 min. Then, these activated CB-peptide probes were mixed with CNP solution at room temperature (RT) in the dark for 12 h. After dialysis against distilled water (DW) and lyophilization, the CB-CNP (molecular weight 345 kDa) was obtained as blue powder. Meanwhile, CNP-Cy5.5 was synthesized by mixing Cy5.5-NHS with CNP solution at RT in the dark for 12 h.

2.2.3. Characterization of cathepsin B-sensitive nanoprobe

The mean diameter and size distribution of the CB-CNP were observed with dynamic light scattering (DLS) at 25°C. The CB-CNP's morphology in DW (1 mg/ml) was assessed with transmission electron microscopy (TEM, CM30

electronmicroscope, Philips, CA). TEM analysis was performed at 200 kV. The sample solution was placed on the grid for 2 min and excess of sample solution was blotted with filter paper. For staining, the grid was placed on a drop of 2% (w/v) uranyl acetate. UV/Vis absorbance of CB-CNP (0.8 μM) and CB-peptide probes at various concentrations (2.5, 5.0, 10, 20 μM, respectively) was recorded from 450 to 800 nm using UV/Vis spectrophotometer (Optizen 2120, Mecasys, Daejeon, Korea). The absorption intensity of BHQ-3 (690 nm) was measured, and the concentration of conjugated CB-peptide probe in CB-CNP was calculated from standard curve made by various concentration of CB-peptide probe.

2.2.4. *In vitro* enzyme specificity

In vitro CB enzyme specificity of the CB-CNP was examined by incubating the CB-CNP with CB, cathepsin L, cathepsin D, or CB plus inhibitor. The CB-CNP (20 nM) was incubated for 50 min in an assay buffer [25 mM of 2-(N-morpholine)-ethanesulphonic acid (MES)] containing 3.0 nM of CB, in an assay buffer (0.1 M of sodium acetate, 0.2 M of NaCl, pH 3.5) containing 23 nM of cathepsin D, or in an assay buffer (50 mM of MES, 5 mM of DTT, pH 6.5) containing 1.0 nM of cathepsin L, respectively. Fluorescence intensity was measured with a spectrofluorometer (F-7000 Fluorescence Spectrophotometer, Hitachi, Tokyo, Japan) every 10 min for 50 min at 37°C. The excitation wavelength was 675 nm, and the emission intensity was measured at 693 nm. In addition, the CB-CNP (20 nM) was

incubated in 25 mM of MES buffer containing different concentrations (0, 1.0, 2.0, 4.0, 8.0 nM) of CB enzyme for 50 min.

2.2.5. Cytotoxicity

Murine squamous cancer cells (SCC7), human colon cancer cells (HT29), enhanced firefly luciferase (luc2) gene-transfected mouse mammary gland tumor cells (4T1-luc2), and red fluorescence protein (RFP) gene-transfected mouse melanoma cells (RFP-B16F10) were maintained in RPMI 1640 medium containing 10% (v/v) FBS and penicillin G (100 U/ml)/streptomycin (100 μg/ml) at 37°C, 5% CO_2. Human fibrosarcoma cells (HT1080) and mouse embryonic fibroblast cells (NIH3T3) were maintained in DMEM containing 10% (v/v) FBS and penicillin G (100 U/ml)/streptomycin (100 μg/ml) at 37°C, 5% CO_2.

The CB-CNP's cytotoxicity was evaluated using Cell Counting Kit-8 (CCK-8) assay. In brief, four kinds of cells, HT29, 4T1-luc2, RFP-B16F10 and HT1080 (1 × 104 cells/well) were seeded in a 96-well microplate, and cultured for 24–36 h. The CB-CNP concentrations (5, 10, 25, 50, 100 μg/ml) were added to each well of the cell culture and incubated for 24 h. CCK-8 solution was added to each well of the cell culture and incubated for 2 h, and absorbance was observed at 450 nm with a plate reader. Cell viability was expressed as a percentage relative to the untreated control cells.

2.2.6. Cellular uptake and immunocytochemistry

SCC7 cells (1×10^4 cells/dish) were plated in 35 mm cover-glass bottom dishes and grown to 80% confluence. The cells were washed twice with PBS (pH 7.4), and then incubated with serum-free medium containing CB-CNP (200 nM) and cathepsin B substrate peptide probe with same amount of Cy5.5 in the presence or absence of inhibitors for 6 h. The inhibitor was treated 30 min before CB-CNP incubation. The cells were washed with PBS (pH 7.4) twice, fixed with fresh 4% (v/v) paraformaldehyde at room temperature for 5 min, and mounted with Fluoromount-G™ (Southern Biotech, Birmingham, AL). Cellular uptake of the probes were observed using IX81-ZDC focus drift compensating microscope (Olympus, Tokyo, Japan) equipped with a 673-nm excitation filter and a 692-nm emission filter.

Five kinds of cells were plated in 35 mm cover-glass bottom dishes and incubated for 48 h. The CB-CNP (200 nM) was treated in each cell culture and incubated for 2 h. After incubation, the cells were washed with PBS and fixed in 4% (v/v) paraformaldehyde at RT for 10 min. The antigens were retrieved in the buffer (100 mM Tris, pH 9.5, urea [5%, w/v]) at 95°C for 10 min, and the cells were permeabilized with Triton X-100 (0.25%, w/v) for 5 min in PBS. Permeabilized cells were treated with monoclonal mouse anti-CB IgG (1:150 dilution) for 2 h and then with goat anti-mouse IgG-FITC (1:1500 dilution) for 30 min. Then, the cells were stained with 4',6-diamidino-2-phenylindole (DAPI). The samples were

observed with an IL-70 microscope (Olympus, Tokyo, Japan) equipped with a mercury arc lamp, a digital camera (Roper Scientific, Tucson, AZ), and optical filter sets (Omega Optical, Battleboro, VT).

2.2.7. Tumor models

All animal experimental procedures were in compliance with the institutional guidelines of Korea Institute of Science and Technology and the relevant laws. Five tumor models were utilized in this study. All tumors were induced in male athymic nude mice (20 g, Orient, Korea), and mice were anesthetized with an intraperitoneal injection of xylazine (10 mg/kg body weight) and ketamine (80 mg/kg body weight). For the induction of subcutaneous tumors, mice were anesthetized and SCC7 cells (1×10^6 cells/mouse) or HT29 cells (7×10^6 cells/mouse) suspended in 100 μl sterile saline were subcutaneously injected into the flank of athymic nude mice, respectively. When subcutaneous tumors reached 5.0 ± 0.5 mm in diameter, the mice were utilized for imaging. The CB inhibitor was intratumorally injected 30 min before the CB-CNP administration. To induce liver tumors, mice were anesthetized, a paramidline abdominal incision was made, and the liver was exposed. Then, HT29 cells (3×10^5 cells/mouse) suspended in 20 μl of sterile saline were injected into the left lobe of the liver under the capsule.[9] After injection of the cells, the paramidline incision was sutured. Seven days after the injection of HT29 cells into the liver, the mice were utilized for imaging. To induce liver metastases,

mice were anesthetized, an incision on a left lateral flank was made, and the spleen was exposed. Then, 4T1-luc2 cells (3×10^5 cells/mouse) suspended in 30 μl of sterile saline were injected into the spleen.[10, 11] After injection of the cells, the incision was sutured. At 10 to 14 days after the injection of 4T1-luc2 cells, the mice were utilized for imaging. For the lung metastases, RFP-B16F10 cells (3×10^5 cells/mouse) suspended in 50 μl of sterile saline were injected into the tail vein.[9, 12] Fourteen days after the injection of RFP-B16F10 cells, the mice were utilized for imaging. For the peritoneal metastases, HT1080 cells (3×10^5 cells/mouse) suspended in 300 μl of sterile saline were intraperitoneally injected.[13, 14] Five days after the injection of HT1080 cells, the mice were utilized for imaging.

2.2.8. *In vivo* and *ex vivo* fluorescence imaging

The CB-CNP (100 μg/100 μl/mouse) was intravenously injected via the tail vein into all tumor-bearing mice. *In vivo* NIR tomographic images were acquired with an eXplore Optix system (Advanced Research Technologies Inc., Montreal, Canada). For quantitative analysis, the total photon counts in tumors were calculated using the region of interest (ROI) measurement of the Analysis Workstation software program (Advanced Research Technologies Inc.), and the tumor signal to background ratio (TBR) between the tumor and normal region was also evaluated as a function of time. In addition, *in vivo* NIR fluorescence was imaged with an IVIS Spectrum imaging system (Caliper Life Sciences, Hopkinton, MA). For *in vivo*

bioluminescence imaging, D-luciferin solution (150 mg/kg body weight) was intraperitoneally injected 10 min prior to imaging. Bioluminescence imaging was performed with the IVIS Spectrum imaging system. *In vivo* NIR fluorescence molecular tomography (FMT) system (VisEn Medical Inc., Bedford, MA) was operated with a 680 nm fluorescence channel to obtain three-dimensional (3-D) *in vivo* images of CB activity in the lung metastatic model. FMT images were acquired between 0.29 and 2.05 mm at 0.59-mm steps. FMT images were obtained by utilizing a continuous wave-type scanner to obtain transillumination, absorption, and reflectance data.

After *in vivo* imaging studies, the mice were sacrificed, and the organs were excised and imaged using a Kodak image station (4000MM; Kodak, New Haven, CT) equipped with a special C-mount lens and Cy5.5 and RFP bandpass emission filters. In addition, *ex vivo* NIR fluorescence images of the organs were taken using the IVIS Spectrum imaging system.

2.2.9. Histological and Western blot analyses

Each organ was fixed in formalin (4%, v/v) and embedded in paraffin for hematoxylin and eosin (H&E) staining and IHC. Then, 5 μm-thick sections cut from the paraffin-embedded specimens were stained with H&E. In addition, 5 μm-thick sections were stained with the primary antibodies against CB. Signal visualization

was achieved with a Histostain®-Plus Kit. Sections were counterstained with Harris's hematoxylin. Meanwhile, 8 μm-thick frozen sections of HT29 subcutaneous tumors were prepared for fluorescence microscopic imaging of Cy5.5 and DAPI.

For Western blot analysis, each aliquot of the extracted normal organ or metastasis mixed with a sample buffer (0.25 M of Tris, 0.8% [w/v] sodium dodecyl sulfate, 10% [v/v] glycerol, 0.05% [w/v] bromophenol blue, pH 6.8) was run on 7.5% polyacrylamide gel after boiling (10 min). Gels were transferred to a blot membrane using iBLOT (Invitrogen). Membranes were blocked with milk in Tris-buffered saline-Tween20 (TBST) at RT for 1 h and then incubated with anti-CB at RT for 1 h. Three washes (15 min each) with TBST were performed, and the membranes were incubated with a horseradish peroxidase-conjugated anti-mouse antibody for 30 min in TBST and then washed (three washes, 15 min each) with TBST. Immunoreactive proteins were visualized with enhanced chemiluminescence.

2.2.10. Statistical analysis

Data represents the means ± standard deviation. A one-way analysis of variance was used for the comparison of variables between groups. A value of $p < 0.05$ was considered statistically significant.

2.3. Results

2.3.1. Development and characterization of cathepsin B-sensitive nanoprobe

The CB-CNP was developed by conjugating CB-peptide probes (molecular weight 2117 Da) which is composed of cathepsin B substrate peptide, NIR florophore (Cy5.5), and dark quencher (BHQ-3), on the surface of self-assembled CNPs as a carrier (Figure 2.2). CNPs were variously characterized.[15-17] CNPs showed fast uptake into cancer cells because CNPs could avoid unintended uptake from macrophages and pass through vascular structure. Also, CNPs could enable efficient accumulation in tumor tissue likely due to *in vitro*/*in vivo* stability and rapid uptake into target tumor cells.[9, 17] After these procedures, CB-peptide probe on CNPs could generate NIR fluorescence signals in response to CB.

To develop CB-CNP, the peptide sequence, Gly-Arg-Arg-Gly-Lys-Gly-Gly with Arg-Arg as a recognition sequence was used.[18] The Arg-Arg sequence is known to confer substantial specificity to cathepsin B as compared with other cathepsins.[19, 20] The CB-peptide probes were characterized by HPLC, UV/Vis spectra, fluorescence emission spectra, MALDI-TOF mass spectrometry, which indicated that CB-peptide probes were successfully developed (Figure 2.3). The CB-peptide probes were conjugated on the surface of CNPs in the presence of EDC and sulfo-NHS. The conjugation of CB-peptide probes to CNP was confirmed by measuring the absorption intensity of BHQ-3 (690 nm) using UV/Vis spectrophotometer (Figure

2.4). The absorption intensity of CB-CNP (0.8 μM) corresponds to 17 μM of CB-peptide probe in the standard curve, indicating that approximately 21 molecules of CB-peptide probes were attached to 1 CNP molecule. Therefore, it was calculated that the molecular weight of CB-CNP was 345 kDa. TEM and DLS analyses showed that the CB-CNP formed a spherical nanoparticle and that it was 280 ± 24 nm in diameter (Figure 2.5 a). The CB-CNP's cytotoxicity in four different cell lines (HT29, 4T1-luc2, RFP-B16F10, and HT1080) was determined using CCK-8 assay (Figure 2.5 b). The CB-CNP exhibited cell viability > 95% against all types of cells at concentrations up to 50 μg/ml.

The CB-CNP was significantly strongly quenched in physiological condition and specifically activated by CB. The CB-CNP's fluorescence intensity was highly quenched in 25 mM of MES buffer at 37°C. When the CB-CNP was incubated with various concentrations of CB for 50 min at 37°C, the self-quenched CB-CNP's fluorescence signal was activated (18, 11, 4.9, and 2.3-fold fluorescence increases for 8.0, 4.0, 2.0, and 1.0 nM of CB, respectively, for 50 min), depending on the CB concentrations (r^2 = 0.99) (Figure 2.5 c). In particular, the CB-CNP boosted a considerable florescence signal with 1.0 nM of CB, demonstrating high sensitivity to active CB. The *in vitro* specificity of the CB-CNP was examined with CB, cathepsin D, cathepsin L, and CB plus inhibitor, respectively. During a 50-min incubation at 37°C, the NIR fluorescent signal was time-dependently recovered when treated with CB, whereas minimal increases in fluorescence signals occurred with cathepsin D, cathepsin L, and CB plus inhibitor (Figure 2.5 d).

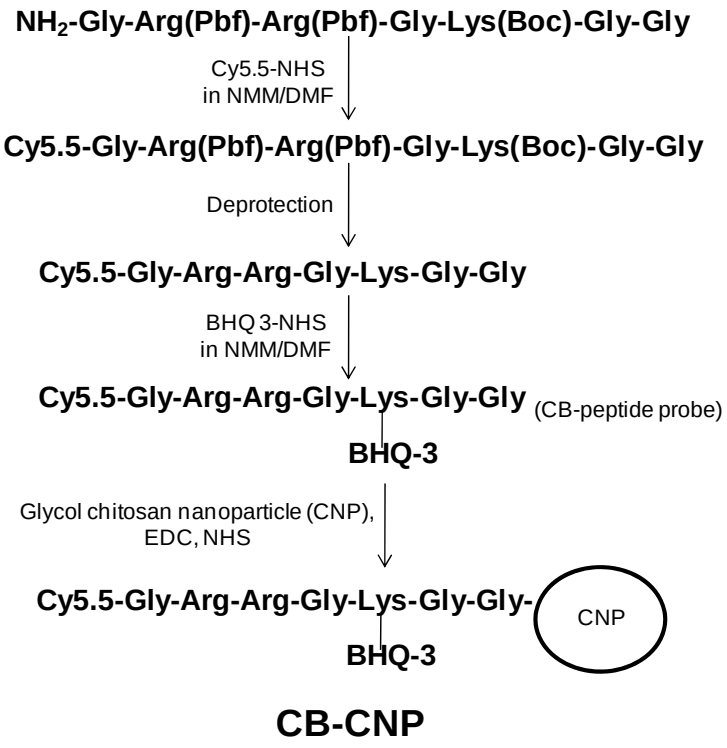

Figure 2.2. Synthetic scheme of cathepsin B-sensitive nanoprobe (CB-CNP).

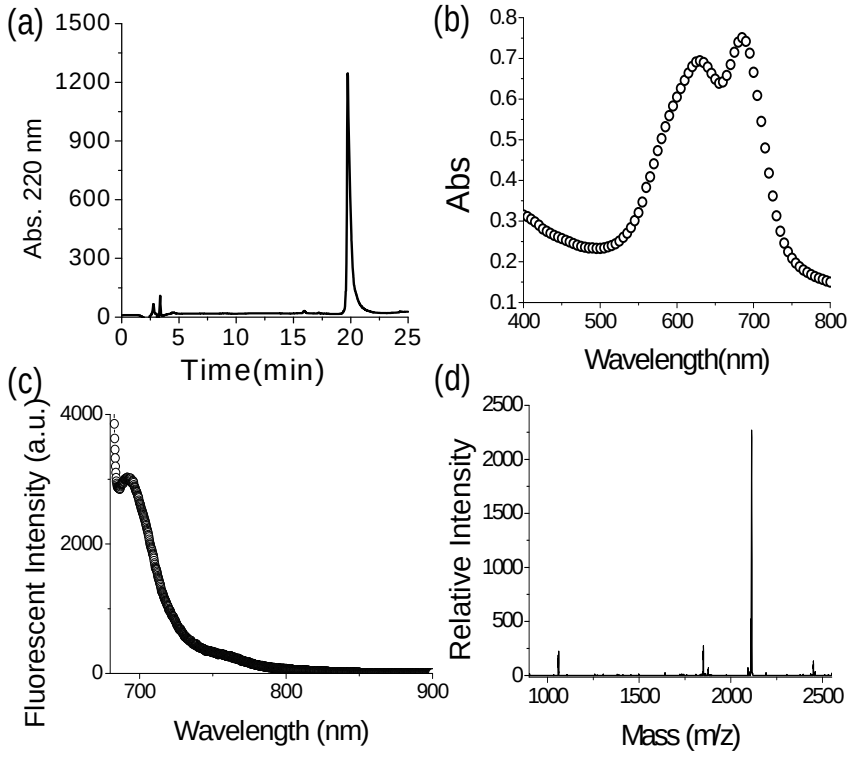

Figure 2.3. Analytical experiments including (a) HPLC, (b) UV/Vis spectra, (c) emission spectra, and (d) MALDI-TOF mass spectrometry of cathepsin B-peptide probe.

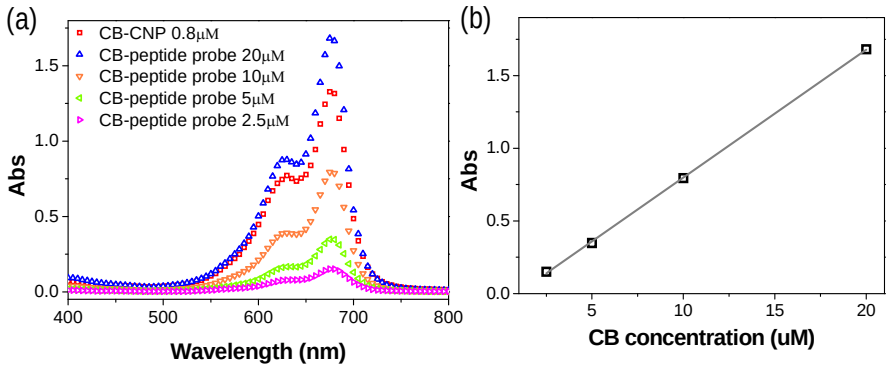

Figure 2.4. Characterization of the cathepsin B (CB)-sensitive nanoprobe (CB-CNP) including (a) UV/Vis absorbance of CB-CNP (0.80 μM) and various concentrations of CB-peptide probes (2.5, 5.0, 10, 20 μM), (b) standard curve for calculation of the amounts of CB-peptide probes conjugated to chitosan nanoparticles (CNPs).

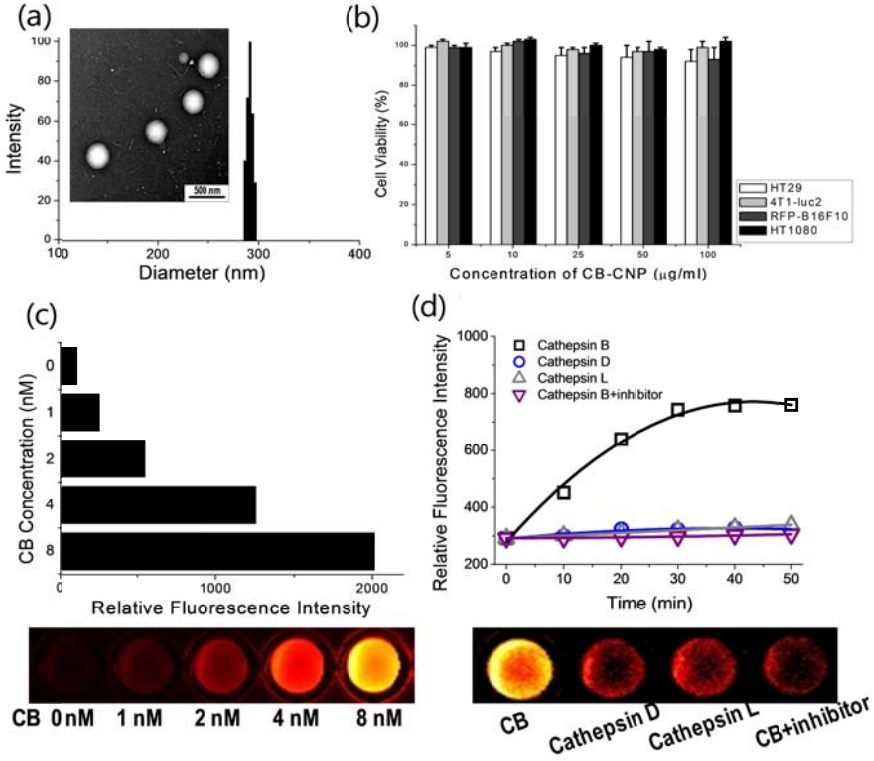

Figure 2.5. Characterization of the cathepsin B (CB)-sensitive nanoprobe (CB-CNP). (A) Size distribution of the CB-CNP in phosphate-buffered saline; Inset, TEM image of the CB-CNP. (B) Cell viability measured with CCK-8 assay. HT29, 4T1-luc2, RFP-B16F10, and HT1080 were incubated for 24 h with various concentrations of the CB-CNP (5, 10, 25, 50, 100 μg/ml). (C) Relative fluorescence intensity of the CB-CNP after incubation with various concentrations of CB (0, 1.0, 2.0, 4.0 and 8.0 nM) for 50 min at 37°C; lower, the corresponding NIR fluorescence images of the CB-CNP treated with various concentrations of CB. (D) Fluorescence emission spectra of the CB-CNP in the presence of different stimuli (CB, cathepsin D, cathepsin L, and CB with inhibitor) for 50 min at 37°C; lower, the corresponding NIR fluorescence images of the CB-CNP in the presence of different stimuli.

2.3.2. Advantages of nanoprobes for imaging of cathepsin B activity

Advantages of nanoprobes for imaging of CB activity were confirmed in cellular condition and *in vivo*. An obvious intracellular fluorescence due to the activation of the probe after cellular uptake was detected after 60 min incubation with the CB-CNP. The CB-CNP provided increasing Cy5.5 signal (red) in a time-dependent manner, whereas the fluorescence signals were not observed in cells incubated with cathepsin B inhibitor, indicating specific response of CB-CNP to CB (Figure 2.6). A more intense Cy5.5 signal with CB-CNP than that with CB-peptide probe was observed, which is attributed to fast uptake of CB-CNP into cancer cells. Fast uptake of the probe could be a critical factor for imaging of the pericellular protease such as cathepsin B.

To validate the use of CB-CNP for *in vivo* imaging of CB, the whole-body fluorescence images were obtained in SCC7 tumor-bearing mice after intravenous injection of CB-CNP.[19] An obvious fluorescence signal was detected from the tumor as early as 1 h after injection (Figure 2.7 a). The NIR fluorescence signal from the tumors were significantly increased to 6 h, and showed steady intense signals over 1 day post-injection of CB-CNP and CB-peptide probe. The NIR fluorescence signal from the tumor in CB-CNP-treated mouse slowly diminished after 1 day, but tumor tissue was still brighter than the surrounding normal tissue even after 2 days. Meanwhile, the NIR fluorescence signal from the inhibitor-treated tumors was significantly faint. The NIR fluorescence intensity in tumor tissue was also evaluated as a function of time after injection of CB-CNP, CB-

peptide probe, and CB-CNP plus inhibitor to tumor-bearing mice, respectively (Figure 2.7 b). The signals gradually increased until 6 h after injection of CB-CNP and CB-peptide probe, whereas there was only a minimal increase in the inhibitor-treated mice. At 6 h post-injection of CB-CNP and CB-peptide probe, the NIR fluorescence intensities in tumors were about 11.5 and 5.2 fold higher than that of the inhibitor-treated one. Highly enhanced signal of CB-CNP than that of CB-peptide probe significantly demonstrated the advantage of tumor-targeting CNP carriers such as high accumulation in tumor tissue and fast uptake into tumor cells. To further assess the results of *in vivo* imaging, tumors and other organs were excised after whole body imaging at 6 h post-injection of probes, and examined using a Kodak Image Station.[20] The highest NIR fluorescence intensity was markedly observed in the tumor of CB-CNP injected mouse, and *ex vivo* images of each group of mice were in accordance with the trends shown in the whole body imaging (Figure 2.7).

2.3.3. Cellular uptake and cathepsin B distribution

The CB-CNP's cellular uptake and CB distribution were monitored in five different cell lines (Figure 2.8). In this study, the cancer cell lines HT29,[21] 4T1,[22] B16F10,[23] and HT1080[24] which are known to highly express CB, were selected as positive target cell lines. As a negative control, NIH3T3 cell line was selected, as this cell line is known to have no or extremely low CB expression.[25] In fact, CB was highly expressed in HT29, 4T1-luc2, RFP-B16F10, and HT1080 cells and barely

expressed in NIH3T3 cells, as confirmed by immunocytochemistry. After incubation for 2 h with the CB-CNP, an intense Cy5.5 fluorescence signal was observed mainly in the cytoplasm of HT29, 4T1-luc2, RFP-B16F10, and HT1080

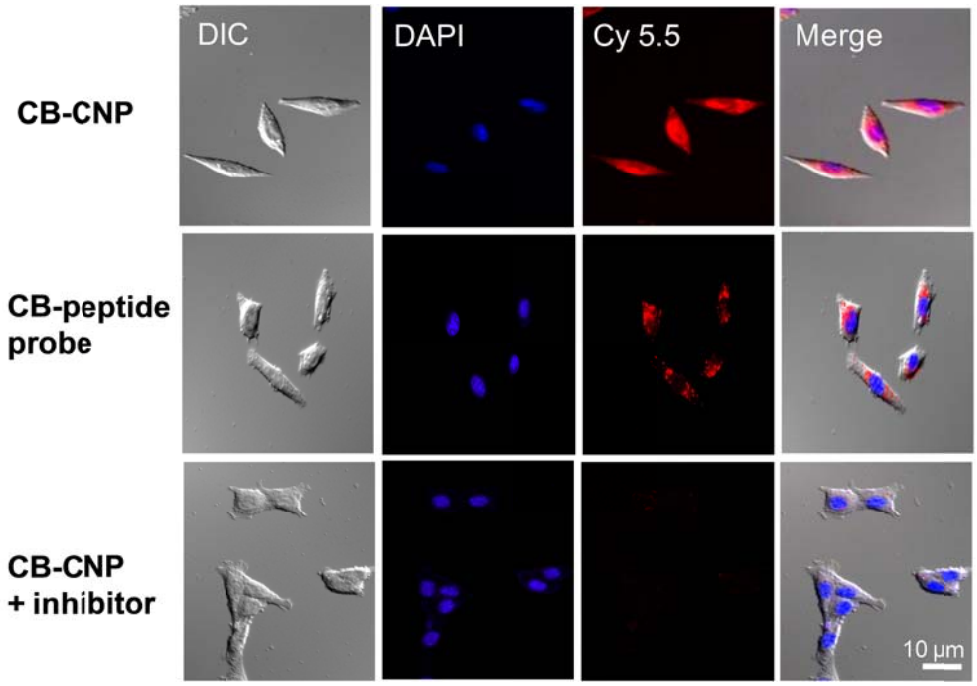

Figure 2.6. Cellular uptake and immunocytochemistry of cathepsin B (CB)-sensitive nanoprobe (CB-CNP). **(a)** Cellular uptake images of SCC7 cells in media containing in the presence or absence of CB inhibitor at 6h post-treatment of CB-CNP or CB-peptide probe.

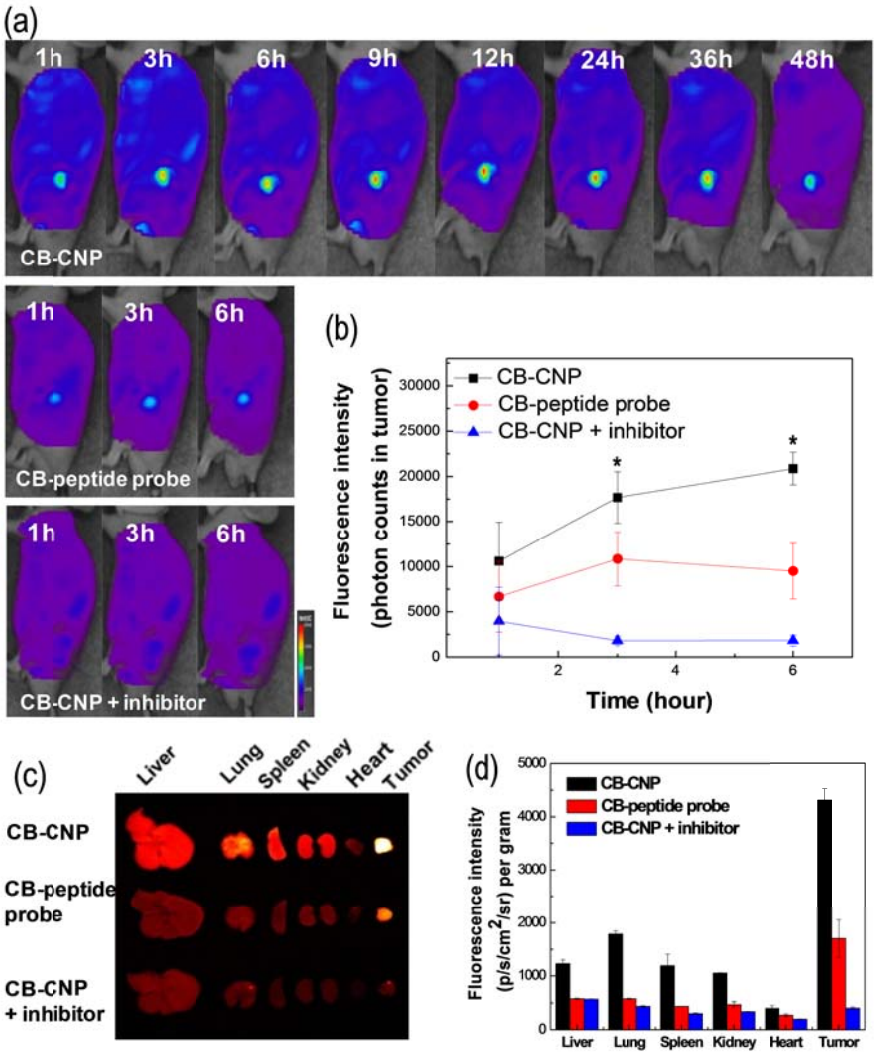

Figure 2.7. *In vivo* near infrared (NIR) fluorescence imaging of CB activity in tumor tissue with cathepsin B (CB)-sensitive nanoprobe (CB-CNP). (a) Whole body NIR fluorescence images of SCC7 tumor-bearing mice after intravenous injection of CB-CNP or CB-peptide probe in the presence or absence of CB inhibitor. (b) NIR fluorescence signal intensity in tumor region of (a). (c) NIR fluorescence images of excised tumors and other organs. (d) NIR fluorescence signal intensity of (c). Asterisks indicate $p < 0.05$.

cells, which suggested that the CB-CNP was internalized into tumor cells and activated in their cytoplasm. Conversely, only a faint Cy5.5 fluorescence was detected in NIH3T3 cells. In addition, the fluorescence signal from the CB-CNP (red) was co-localized with that of CB expression (green). These results clearly indicate that the CB-CNP could easily enter into tumor cells and specifically respond to CB in such cells.

2.3.4. Probe specificity for cathepsin B *in vivo*

The CB-CNP's specificity for CB was evaluated in HT29 subcutaneous tumor-bearing mice. Following systemic administration of the CB-CNP, the tumors' NIR fluorescence signals significantly increased for 6 h and slowly diminished afterwards (Figure 2.9). In contrast, their NIR fluorescence signals were noticeably reduced when CB inhibitor was intratumorally injected 30 min before the CB-CNP administration. Six hours after the CB-CNP was intravenously injected, the NIR fluorescence intensity of non-treated tumors was 17.1 fold higher than that of inhibitor-treated tumors (27900 ± 4520 for non-treated tumors versus 1630 ± 363 for inhibitor-treated tumors; $p < 0.05$). H&E displayed the growth of HT29 tumors, and IHC for anti-CB antibody showed substantial CB expression in the whole tumor tissue (Figure 2.9 c). Fluorescence microscopy images of non-treated tumors demonstrated significantly stronger Cy5.5 fluorescence than that of inhibitor-treated tumors. The CB-CNP's detection sensitivity was compared with that of CNP-Cy5.5

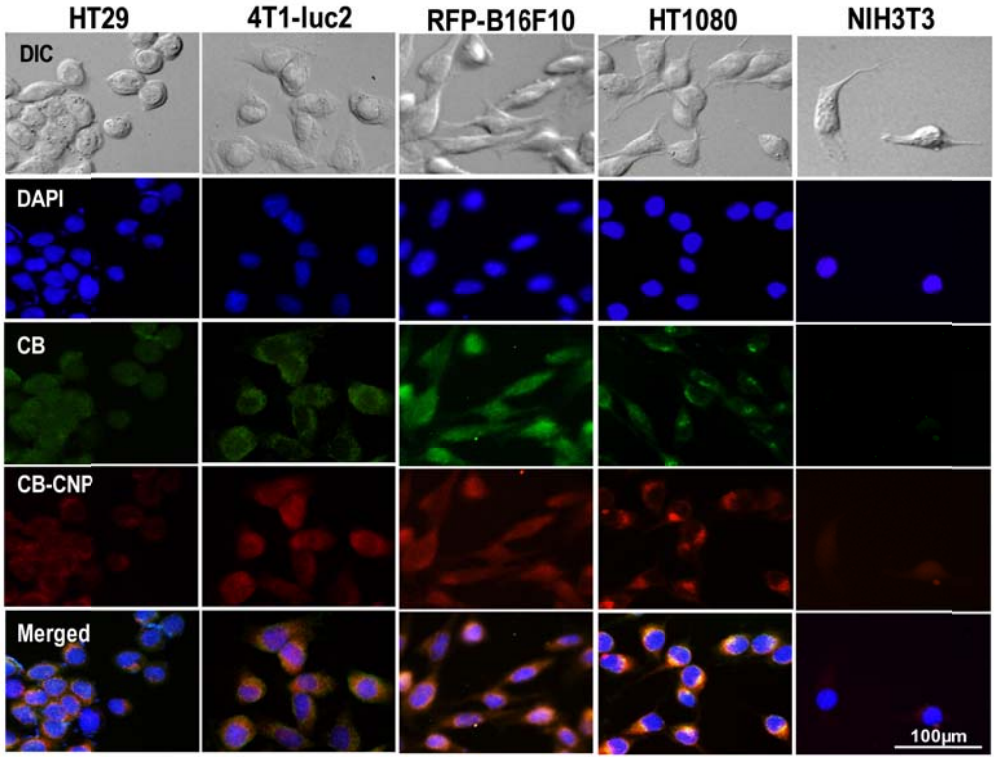

Figure 2.8. Cellular uptake of the cathepsin B (CB)-sensitive nanoprobe (CB-CNP) and immunocytochemistry for CB in the tumor cells. HT29, 4T1-luc2, RFP-B16F10, HT1080, and NIH3T3 cells were incubated in the media containing the CB-CNP (red) for 2 h. Fluorescein isothiocyanate-conjugated antibody against CB was used for CB imaging (green), and the nucleus was stained with DAPI (blue). The scale bar indicates 100 μm.

without CB-sensitive moiety in the HT29 liver tumor model. Liver tumor model was induced by laparotomy and subsequent injection of HT29 tumor cells into the left lobe of the liver. In bright field images of the excised livers, the tumor region can be easily detected from normal regions due to its color change and mainly detected in the left lobe of the liver. Whereas the NIR fluorescence signal from CNP-Cy5.5 was widely detected throughout the left liver lobes including tumors, the signal from the CB-CNP was well localized to the tumor region in the left liver lobes (Figure 2.9 d).

2.3.5. *In vivo* imaging of cathepsin B activity in three different metastatic mouse models

Next, it was evaluated whether the CB-CNP could be used to discriminate metastases in three different metastatic mouse models. Liver metastasis model was induced by injecting 4T1-luc2 cells into spleen.[10, 11] Metastases in the liver were detected in all mice 10 to 14 days after 4T1-luc2 cell injections into the spleen, as confirmed by bioluminescence imaging. Following systemic administration of the CB-CNP, strong NIR fluorescence signals were demonstrated in the vicinity of the liver and the spleen at 1 h, as measured in Optix (Figure 2.10 a). On the other hand, minimal fluorescence recovery was detected in normal mice after intravenously injecting the CB-CNP. Fluorescence signal from the CB-CNP was considerably matched with bioluminescence signal, as confirmed in *ex vivo* images (Figure

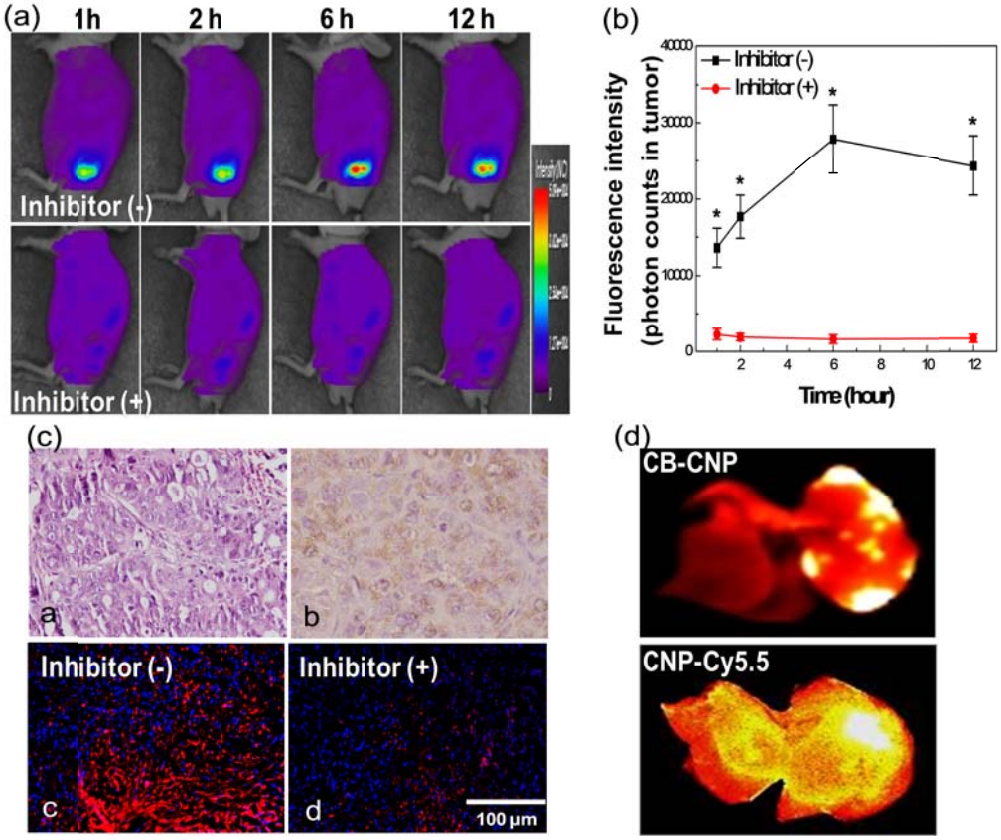

Figure 2.9. Probe specificity and detection sensitivity for cathepsin B (CB) in the subcutaneous tumor model. (a) Whole-body fluorescence images of HT29 subcutaneous tumor-bearing mice after intravenous injection of the CB-sensitive nanoprobe (CB-CNP) in the absence or presence of CB inhibitor. (b) Fluorescence intensity in the tumor region of (a). Asterisks indicate $p < 0.05$. (c) **a** Hematoxylin and eosin staining of the tumor section, **b** immunohistochemical staining of the tumor section for CB, and fluorescence microscopy images of **c** the tumor section and **d** the inhibitor-treated tumor section. The CB-CNP was expressed in red and DAPI in blue in fluorescence microscopy images. (d) *Ex vivo* images of HT29 liver tumors 12 h after intravenous injection of the CB-CNP and CNP-Cy5.5.

2.10b). Western blot analysis revealed that the level of CB expression in liver metastases had increased compared to normal liver (Figure 2.10 c).

Lung metastases were induced in all animals 14 days after RFP-B16F10 cells expressing the RFP gene were injected into the tail vein. Following the systemic administration of the CB-CNP, the intense NIR fluorescence signal in the vicinity of the lungs was increasingly observed from 1 h to 12 h, as monitored by Optix (Figure 2.11 a). On the other hand, weak fluorescence recovery was detected in normal mice after the intravenous injection of the CB-CNP. Three-dimensional *in vivo* images of CB activity in lung metastases were acquired using VisEn FMT.[26] FMT technology is known to achieve several centimeters of tissue penetration.[27, 28] These images demonstrated variations in CB activity with position (between 0.29 and 2.05 mm at 0.59-mm steps) (Figure 2.11 b). RFP signals expressed from excised lungs clearly indicated that metastases were induced in the lungs (Figure 2.11 c). Also, *ex vivo* images of the lung metastasis revealed high accumulation and fluorescence activation of the CB-CNP by NIR fluorescence imaging. Conversely, minimal fluorescence was exhibited in *ex vivo* images of the normal lung. H&E displayed the growth of B16F10 tumors, which is different from that of normal lungs (Figure 2.11 d). Western blot analysis demonstrated that the level of CB expression in lung metastases had increased compared to normal lung (Figure 2.11 e).

Lastly, the CB-CNP's potential for discriminating peritoneal metastases *in vivo* were investigated. Metastases in the peritoneum were induced in all animals 5 days

after HT1080 cells were intraperitoneally injected. Following the systemic administration of the CB-CNP, the NIR fluorescence signal around the peritoneal cavity was gradually enhanced from 1 h to 7 h, as measured by Optix (Figure 2.12 a). Under *in vivo* observation using the IVIS system, substantial fluorescence activity around the peritoneal cavity of intact mice was also detected after the intravenous injection of the CB-CNP (Figure 2.12 b). In the *ex vivo* observation, several nodules with significant NIR fluorescence activity were detected on the peritoneum of the abdominal wall when CB-CNP was intravenously injected into the mice (Figure 2.12 c). H&E displayed the growth of HT1080 tumors, which is different from that of normal peritoneum (Figure 2.12 d).

2.4. Discussion

A significant amount of experimental evidence has been supported that CB takes part in the metastatic process: a number of studies have obviously demonstrated that CB activity is closely correlated with tumors' invasive and metastatic potential.[29-31] Many studies have implicated elevated CB activity in the metastatic process *in vitro*. However, few studies have demonstrated visualization of CB activity in the metastases *in vivo*, as unsatisfactory sensitivity make it difficult to detect metastases in host tissues, and *in vivo* metastatic mouse model that closely mimics the clinical situation lacks.[32] In this study, a CB-sensitive and tumor-targeting fluorescence nanoprobe (CB-CNP) was applied to three metastatic mouse models to investigate

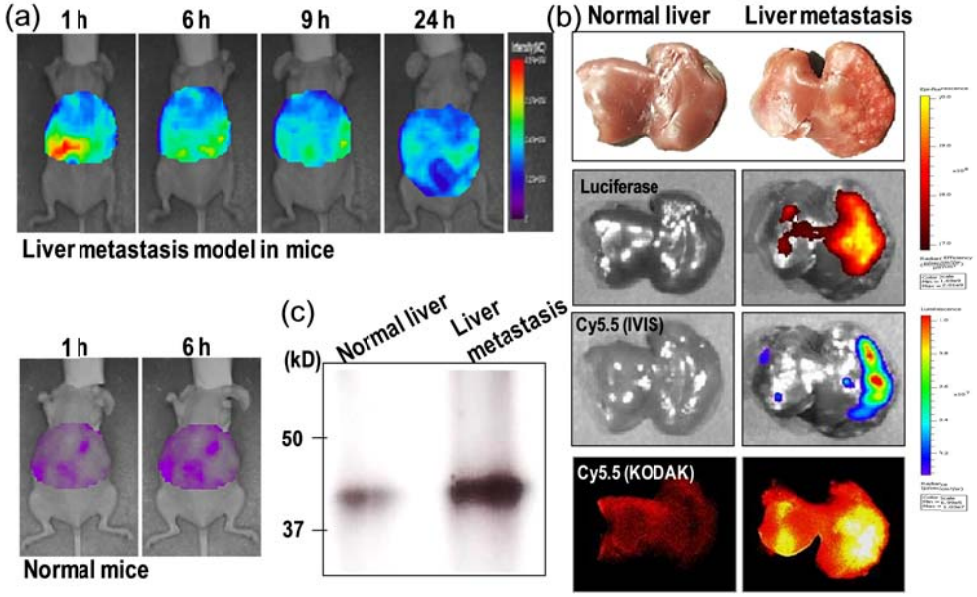

Figure 2.10. *In vivo* NIR fluorescence imaging of cathepsin B (CB) activity in 4T1-luc2 liver metastases with intravenously injected CB-sensitive nanoprobe (CB-CNP). (a) Whole-body fluorescence images of 4T1-luc2 liver metastatic tumor-bearing mice or normal mice after intravenous injection of the CB-CNP. (b) *Ex vivo* images of 4T1-luc2 liver metastasis and normal liver acquired with the IVIS Spectrum imaging system or the KODAK image station 12 h after intravenous injection of the CB-CNP. Bioluminescence imaging indicated the metastatic liver cancer. (c) Western blot analysis to detect CB in liver metastasis and normal liver.

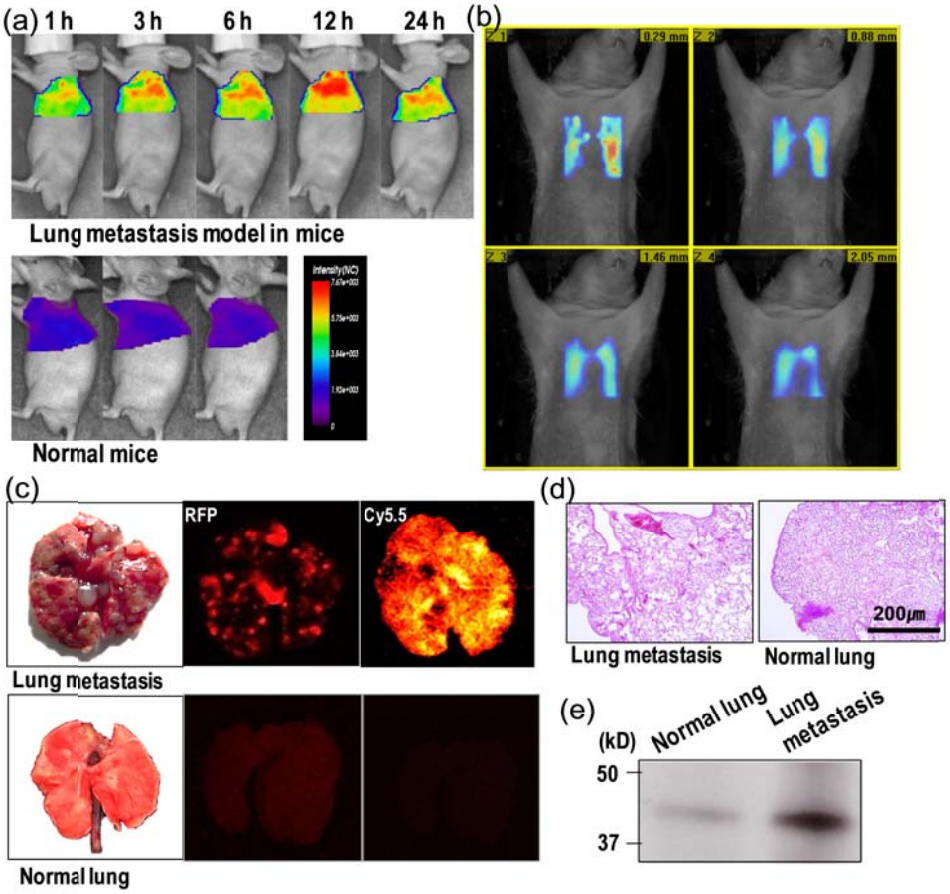

Figure 2.11. *In vivo* NIR fluorescence imaging of cathepsin B (CB) activity in RFP-B16F10 lung metastases with intravenously injected CB-sensitive nanoprobe (CB-CNP). (a) Whole-body fluorescence images of RFP-B16F10 lung metastatic tumor-bearing mice or normal mice after intravenous injection of the CB-CNP. (b) Three dimensional *in vivo* images of CB activity in lung metastases using VisEn FMT. (c) *Ex vivo* images of RFP-B16F10 lung metastases and normal lungs 12 h after intravenous injection of the CB-CNP. An RFP signal indicated the metastatic lung cancer and a Cy5.5 signal in lungs indicated high accumulation and fluorescence activation of the CB-CNP. (d) Hematoxylin and eosin staining images of lung metastasis and normal lung. (e) Western blot analysis to detect CB in lung metastasis and normal lung.

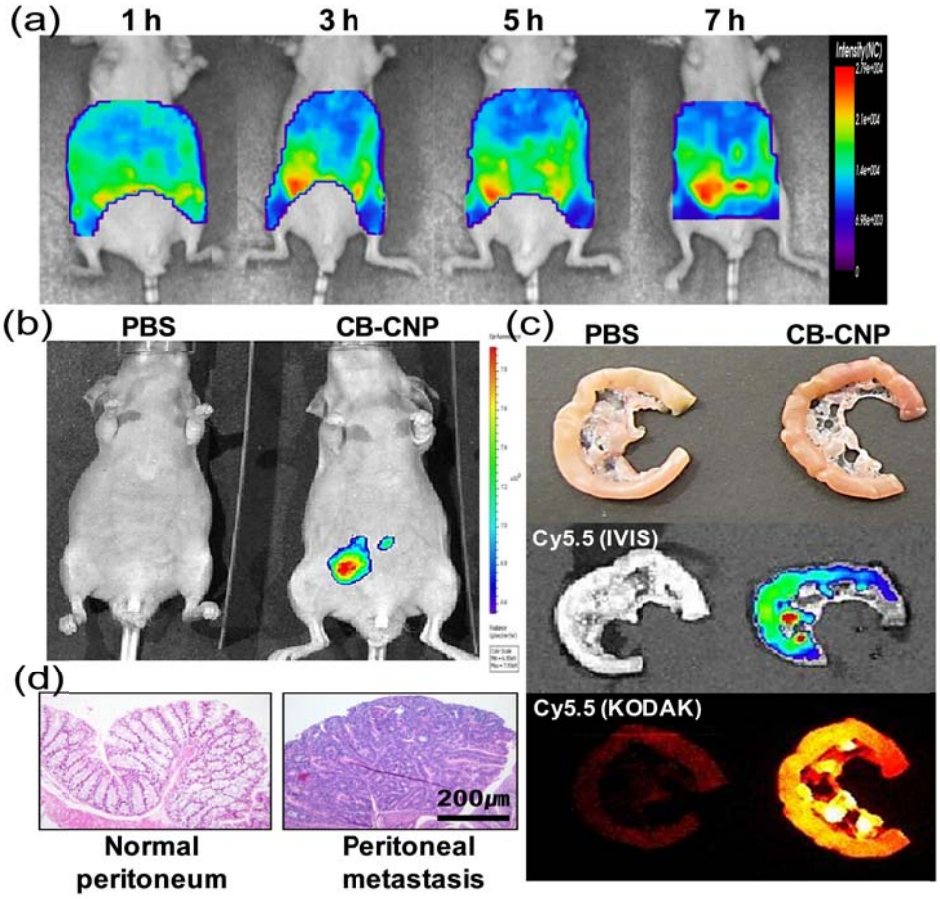

Figure 2.12. *In vivo* NIR fluorescence imaging of cathepsin B (CB) activity in HT1080 peritoneal metastases with intravenously injected CB-sensitive nanoprobe (CB-CNP). (a) Whole-body fluorescence images of HT1080 peritoneal metastatic tumor-bearing mice after intravenous injection of the CB-CNP, acquired by Optix. (b) Whole-body fluorescence images of HT1080 peritoneal metastatic tumor-bearing mice 7 h after intravenous injection of the CB-CNP or phosphate buffered saline (PBS), acquired by an IVIS Spectrum imaging system. (c) *Ex vivo* images of HT1080 peritoneal metastases acquired with a KODAK image station or IVIS Spectrum imaging system 7 h after intravenous injection of the CB-CNP or PBS. (d) Hematoxylin and eosin staining images of peritoneal metastases and normal peritoneum.

its potential use for discriminating metastases *in vivo*.

CB-CNPs can be used to improve the detection of metastases compared to CNP-Cy5.5. Remarkably, the CB-CNP, consisting of CB-responsive probes conjugated onto the surface of tumor-targeting CNP, allowed the tumor tissue to be clearly distinguished from the surrounding normal tissue in a liver tumor model (Figure 2.9 d). The CNP-Cy5.5 mainly accumulated in the tumor tissue rather than the normal liver tissue.[9] This is attributed to superior tumor-targeting ability and cell permeability of CNPs.[9, 33] The CB-CNP's ability to discriminate between tumor tissue and normal tissue more distinctly can be explained in two steps. First, the CB-CNP can be preferentially accumulated in tumor tissues instead of normal tissue via enhanced permeability and retention effects in the same manner as CNP-Cy5.5. Additionally, the CB-CNP undergoes a selective enzymatic cleavage due to the elevated CB activity in metastatic tumor tissues.

Fluorescence imaging using the CB-CNP can provide high sensitivity to detect metastases in cellular and *in vivo* systems because it can stay strongly self-quenched in normal tissue. A high level of sensitivity is required to successfully image disseminated metastases. In terms of sensitivity, an activatable imaging system using the fluorophore (Cy5.5)-quencher (BHQ-3) pair is favorable.[34] Fluorescence imaging is able to distinguish target tumors, taking the surrounding background as a reference.[35] Therefore, it is significant to enhance the signal in tumor cells or tissues while reducing the signal in background normal cells or tissues. Due to the effective fluorescence-quenching property of the quencher (BHQ-3) and the self-quenching

of the fluorophores (Cy5.5), this activatable peptide probes which were covalently onto the surface of the self-assembled nanoparticles, produced a low fluorescence signal in the quenched state. This contributed to extremely low background noise. Moreover, the fluorescence signal of this system was remarkably boosted by the target enzyme (CB), contributing greatly to sensitive detection. Thus, the activatable system using a well-matched fluorophore-quencher pair can improve sensitivity, enabling the sensitive and early *in vivo* diagnosis of metastases.

There are available *in vivo* metastatic mouse models.[36] Intrasplenic injections of 4T1 cells have established liver metastases as well as primary intrasplenic tumors.[10] Dissemination of metastatic cells from splenic tumors into the liver has been carried out by the portal system.[37] In particular, 4T1 cells are known to show strong potential for tumor invasion and metastasis.[38, 39] In fact, 4T1-luc2 cells injected into the spleen have effectively developed metastases in many other organs as well as liver, which is easily confirmed by luminescence imaging due to the transfected luc2 gene (Figure 2.10). Therefore, fluorescence signal in living mice was detected in primary tumor of spleen and other metastases as well as liver metastases. Pulmonary metastases developed by injecting B16 melanoma cells into the tail vein are the best characterized among the experimental metastasis models.[40, 41] In the present study, lung metastases induced with RFP-B16F10 cells were clearly confirmed by RFP signals *ex vivo* (Figure 2.11 c). Peritoneal metastases developed by intraperitoneally injecting HT1080 cells have been used in many metastasis studies.[13, 14, 42] In addition, HT1080 cells are known as highly malignant cells.[42, 43]

Metastases in the peritoneum were confirmed by observable differences from normal peritoneum in H&E staining (Figure 2.12 d). These metastatic mouse models have several advantages for research.[36] Many of these models are consistent and reproducible. The type and number of injected cells can be controlled. Indeed, three metastases used in the study were induced in all animals in which tumor cells were injected. In addition, the time course required for model maturity is relatively rapid in these models. However, these models are pathophysiologically far from naturally occurring metastases and only partially resemble the relevant clinical situation in the metastatic process.[44] Therefore, *in vivo* models of metastases that more closely mimic the clinical situation are needed for clinical cancer research.

An increasing number of treatments of metastases rely on diagnostics and imaging these days. Decisions for cancer patients' treatment are based on detecting and imaging the extent of the disease's spread. In addition, several treatments including directed radiotherapy require the exact tumor localization to be known. Being able to non-invasively visualize gross metastases and metastatic cell clusters within the intact whole body could help to facilitate guided surgery. Having the ability to accurately localize metastases during surgery is helpful for surgeons to eradicate metastases when using fluorescence cameras in the operating room. Fluorescence imaging using the CB-CNP developed in this study could be utilized as a means for guided surgery. The CB-CNP can be quite practical because it enables the fast and easy acquisition of images, which is advantageous for avoiding associated health risks by minimizing time under anesthesia.[10]

2.5. Conclusions

The facts that the activity of CB is markedly linked to the metastatic process and that CB is found highly expressed in the pericellular regions in this process make CB an attractive target for diagnosing metastases. The CB-CNP consisting of CB-sensitive fluorescence peptide probes conjugated onto the surface of tumor-targeting glycol chitosan nanoparticles, facilitated specific and sensitive visualization of CB activity in the cellular study and *in vivo* tumor models. Importantly, the CB-CNP demonstrated the potential to discriminate metastases *in vivo* in three metastatic mouse models including liver, lung, and peritoneal metastases. Developing a molecular imaging technology to depict metastases enables medical therapy to be personalized, tailoring treatment to each individual patient by minimizing the risks and maximizing the benefits.

2.6. References

1. Sporn, M. B. *Lancet* **1996**, *347*, 1377.

2. Chaffer, C. L.; Weinberg, R. A. *Science* **2011**, *331*, 1559.

3. McCann, T. E.; Kosaka, N.; Turkbey, B.; Mitsunaga, M.; Choyke, P. L.; Kobayashi, H. *NMR in Biomedicine* **2011**, *24*, 561.

4. Elliott, E.; Sloane, B. *Perspectives in Drug Discovery and Design* **1996**, *6*, 12.

5. Sloane, B. F.; Rozhin, J.; Johnson, K.; Taylor, H.; Crissman, J. D.; Honn, K. V. *Proceedings of the National Academy of Sciences* **1986**, *83*, 2483.

6. Van Noorden, C. J. F.; Jonges, T. G. N.; Meade-Tollin, L. C.; Smith, R. E.; Koehler, A. *British Journal of Cancer* **2000**, *82*, 931.

7. Mohamed, M. M.; Sloane, B. F. *Nature Reviews Cancer* **2006**, *6*, 764.

8. Ryu, J. H.; Kim, S. A.; Koo, H.; Yhee, J. Y.; Lee, A.; Na, J. H.; Youn, I.; Choi, K.; Kwon, I. C.; Kim, B.-S.; Kim, K. *Journal of Materials Chemistry* **2011**, *21*, 17631.

9. Na, J. H.; Koo, H.; Lee, S.; Min, K. H.; Park, K.; Yoo, H.; Lee, S. H.; Park, J. H.; Kwon, I. C.; Jeong, S. Y.; Kim, K. *Biomaterials* **2011**, *32*, 5252.

10. Lavilla-Alonso, S.; Abo-Ramadan, U.; Halavaara, J.; Escutenaire, S.; Tatlisumak, T.; Saksela, K.; Kanerva, A.; Hemminki, A.; Pesonen, S. *PLoS ONE* **2011**, *6*, 26810.

11. Osawa Y, S. A. *The Journal of Clinical Investigation* **2013**, *123*, 834.

12. Park, K.; Ki Lee, S.; Hyun Son, D.; Ah Park, S.; Kim, K.; Won Chang, H.; Jeong, E.-j.; Park, R.-W.; Kim, I.-S.; Chan Kwon, I.; Byun, Y.; Kim, S. Y. *Biomaterials* **2007**, *28*, 2667.

13. Mori, A.; Arii, S.; Furutani, M.; Mizumoto, M.; Uchida, S.; Furuyama, H.; Kondo, Y.; Gorrin-Rivas, M. J.; Furumoto, K.; Kaneda, Y.; Imamura, M. *Gene Therapy* **2000**, *7*, 1027.

14. Nayak, T. K.; Garmestani, K.; Milenic, D. E.; Brechbiel, M. W. *Journal of Nuclear Medicine* **2012**, *53*, 113.

15. Kim, K.; Kim, J. H.; Park, H.; Kim, Y.-S.; Park, K.; Nam, H.; Lee, S.; Park, J. H.; Park, R.-W.; Kim, I.-S.; Choi, K.; Kim, S. Y.; Park, K.; Kwon, I. C. *Journal of Controlled Release* **2010**, *146*, 219.

16. Min, K. H.; Park, K.; Kim, Y.-S.; Bae, S. M.; Lee, S.; Jo, H. G.; Park, R.-W.; Kim, I.-S.; Jeong, S. Y.; Kim, K.; Kwon, I. C. *Journal of Controlled Release* **2008**, *127*, 208.

17. Nam, H. Y.; Kwon, S. M.; Chung, H.; Lee, S. Y.; Kwon, S. H.; Jeon, H.; Kim, Y.; Park, J. H.; Kim, J.; Her, S.; Oh, Y. K.; Kwon, I. C.; Kim, K.; Jeong, S. Y. *Journal of Control Release* **2009**, *135*, 259.

18. Maciewicz, R. A.; Etherington, D. J. *Biochemical. Journal.* **1988**, *256*, 433.

19. Mort, J. S.; Recklies, A. D. *Biochemical. Journal.* **1986**, *233*, 57.

20. Almeida, P. C.; Oliveira, V.; Chagas, J. R.; Meldal, M.; Juliano, M. A.; Juliano, L. *Hypertension* **2000**, *35*, 1278.

21. Krueger, S.; Kalinski, T.; Wolf, H.; Kellner, U.; Roessner, A. *Cancer Letters* **2005**, *223*, 313.

22. Xie, B.-W.; Mol, I. M.; Keereweer, S.; van Beek, E. R.; Que, I.; Snoeks, T. J. A.; Chan, A.; Kaijzel, E. L.; Löwik, C. W. G. M. *PLoS ONE* **2012**, *7*, 31875.

23. Sloane, B. F.; Honn, K. V.; Sadler, J. G.; Turner, W. A.; Kimpson, J. J.; Taylor, J. D. *Cancer Research* **1982**, *42*, 980.

24. Kim, M.; Egan, C.; Alain, T.; Urbanski, S. J.; Lee, P. W.; Forsyth, P. A.; Johnston, R. N. *Oncogene* **2007**, *26*, 4124.

25. Yang, Y.; Aw, J.; Chen, K.; Liu, F.; Padmanabhan, P.; Hou, Y.; Cheng, Z.; Xing, B. *Chemistry – An Asian Journal* **2011**, *6*, 1381.

26. Zhang, Q.; Bindokas, V.; Shen, J.; Fan, H.; Hoffman, R. M.; Xing, H. R. *Molecular Cancer Therapeutics* **2011**, *10*, 1173.

27. Ntziachristos, V.; Tung, C.-H.; Bremer, C.; Weissleder, R. *Nature Medicine* **2002**, *8*, 757.

28. Zhao, L.; Lee, V. K.; Yoo, S.-S.; Dai, G.; Intes, X. *Biomaterials* **2012**, *33*, 5325.

29. Coulibaly, S.; Schwihla, H.; Abrahamson, M.; Albini, A.; Cerni, C.; Clark, J. L.; Ng, K. M.; Katunuma, N.; Schlappack, O.; Glössl, J.; Mach, L. *International Journal of Cancer* **1999**, *83*, 526.

30. Hazen, L. G. M.; Bleeker, F. E.; Lauritzen, B.; Bahns, S.; Song, J.; Jonker, A.; Driel, B. E. M. V.; Lyon, H.; Hansen, U.; Köhler, A.; Noorden, C. J. F. V. *Journal of Histochemistry & Cytochemistry* **2000**, *48*, 1421.

31. Withana, N. P.; Blum, G.; Sameni, M.; Slaney, C.; Anbalagan, A.; Olive, M. B.; Bidwell, B. N.; Edgington, L.; Wang, L.; Moin, K.; Sloane, B. F.; Anderson, R. L.; Bogyo, M. S.; Parker, B. S. *Cancer Research* **2012**, *72*, 1199.

32. Hama, Y.; Urano, Y.; Koyama, Y.; Kamiya, M.; Bernardo, M.; Paik, R. S.; Krishna, M. C.; Choyke, P. L.; Kobayashi, H. *Neoplasia* **2006**, *8*, 607.

33. Na, J. H.; Lee, S.-Y.; Lee, S.; Koo, H.; Min, K. H.; Jeong, S. Y.; Yuk, S. H.; Kim, K.; Kwon, I. C. *Journal of Controlled Release* **2012**, *163*, 2.

34. Gong, P.; Shi, B.; Zheng, M.; Wang, B.; Zhang, P.; Hu, D.; Gao, D.; Sheng, Z.; Zheng, C.; Ma, Y.; Cai, L. *Biomaterials* **2012**, *33*, 7810.

35. Ryu, J. H.; Shin, J.-Y.; Kim, S. A.; Kang, S.-W.; Kim, H.; Kang, S.; Choi, K.; Kwon, I. C.; Kim, B.-S.; Kim, K. *Biomaterials* **2013**, *34*, 6871.

36. Khanna, C.; Hunter, K. *Carcinogenesis* **2005**, *26*, 513.

37. Francia, G.; Cruz-Munoz, W.; Man, S.; Xu, P.; Kerbel, R. S. *Nature Reviews Cancer* **2011**, *11*, 135.

38. McEarchern, J. A.; Kobie, J. J.; Mack, V.; Wu, R. S.; Meade-Tollin, L.; Arteaga, C. L.; Dumont, N.; Besselsen, D.; Seftor, E.; Hendrix, M. J. C.; Katsanis, E.; Akporiaye, E. T. *International Journal of Cancer* **2001**, *91*, 76.

39. Kim, J.-B.; Urban, K.; Cochran, E.; Lee, S.; Ang, A.; Rice, B.; Bata, A.; Campbell, K.; Coffee, R.; Gorodinsky, A.; Lu, Z.; Zhou, H.; Kishimoto, T. K.; Lassota, P. *PLoS ONE* **2010**, *5*, e9364.

40. Poste, G.; Doll, J.; Hart, I. R.; Fidler, I. J. *Cancer Research* **1980**, *40*, 1636.

41. Liu, J.; Tan, Y.; Zhang, H.; Zhang, Y.; Xu, P.; Chen, J.; Poh, Y.-C.; Tang, K.; Wang, N.; Huang, B. *Nature Materials* **2012**, *11*, 734.

42. Zijlstra, A.; Mellor, R.; Panzarella, G.; Aimes, R. T.; Hooper, J. D.; Marchenko, N. D.; Quigley, J. P. *Cancer Research* **2002**, *62*, 7083.

43. Stoletov, K.; Montel, V.; Lester, R. D.; Gonias, S. L.; Klemke, R. *Proceedings of the National Academy of Sciences* **2007**, *104*, 17406.

44. Paris, S.; Sesboüé, R. *Carcinogenesis* **2004**, *25*, 2285.

Chapter 3

Epidermal growth factor receptor-targeted imaging of tumors

3.1. Introduction

Receptor-targeted imaging is emerging as a promising strategy for the diagnosis of human cancer.[1, 2] The advantage of specific receptor targeting is obvious - the use of imaging probes with higher specificity towards the target receptor allows highly sensitive and selective imaging with a low dose of the probe.[3-5] Furthermore, receptor-targeted imaging could be helpful in selecting patients for receptor-targeted therapy before the course of treatment.[4] During treatment, receptor-targeted imaging can also monitor effects of the receptor-targeted therapy, allowing clinicians to identify tumor responsiveness before evaluation of traditional, late-stage markers of treatment efficacy, such as a change in tumor size.

Epidermal growth factor receptor (EGFR) is an important target receptor in many types of cancers, including non-small cell lung cancer, skin cancer, breast cancer, small cell carcinoma of head and neck, and prostate cancer.[6-8] Overexpression of EGFR is shown to be correlated with poor prognosis and increased metastatic potential.[9,10] The current standard method to image EGFR has utilized EGFR antibodies, due to their exquisite specificity towards EGFR in tumor cells. When modified with radioisotopes or magnetic or fluorescent probes, EGFR antibodies are used to image various tumors by nuclear, magnetic resonance (MRI), and fluorescence imaging, respectively.[11-13] However, despite numerous studies using EGFR antibody-based imaging probes, they are still limited and insufficient, due to the big size of EGFR antibodies (150 kDa) that cause some drawbacks in receptor-

targeted imaging, such as long circulation time, poor tissue permeability, and slow clearance from the body (few days to weeks), etc.[14,15]

Recently, epidermal growth factor (EGF) has shown great potential for EGFR-targeted cancer imaging.[16-18] EGF is the natural ligand for EGFR and is comprised of 53 amino acids with a molecular weight of ~6 kDa. EGF offers unique advantages for targeting EGFR over EGFR antibody: the binding affinity is typically stronger, cell penetration occurs in deeper regions of the tumor, and clearance rates are more rapid because of a smaller molecular weight compared to EGFR antibody.[19,20] For targeted EGFR imaging, EGF molecules have been labeled with various radionuclides and organic dyes for cell and small animal imaging.[11-13] Owing to its small size and high affinities, EGF-based imaging probe generally show fast tumor targeting (within a half hour), high tumor uptake, and quick clearance from normal tissues.[16] Therefore, EGF-based probes have been known to be a good platform for developing imaging probes for EGFR.

Herein, for construction of an EGFR-specific and activatable probe, EGF was labeled with a quencher and a near-infrared (NIR) fluorophore, producing a fluorescently quenched EGF-based nanoprobe (EGF-NP) (Figure 3.1). A fluorescently quenched imaging probe can reduce background signals and boost strong fluorescence intensity, as in the case of EGF-NP for targeted EGFR imaging. Various protease-targeted activatable nanoprobes were developed for *in vivo* fluorescence imaging, which have a strongly dual-quenched (dye-dark quencher and dye-dye self-quenching mechanism) system.[21-25] They showed highly efficient

quenching and responsive amplified fluorescent signals upon exposure of the probes to targeted protease *in vitro* and *in vivo*.

EGF-NP can be intensely activated in high EGFR-expressing cells and high EGFR-expressing tumor-bearing mice, compared to low EGFR-expressing cells and low EGFR-expressing tumor-bearing mice. Cellular imaging of EGF-NP in tumor cells was captured using live cell imaging microscopy with a video imaging system. In addition, cellular imaging and whole body imaging of EGF-NP treatment was compared to EGFR antibody (Cetuximab)-Cy5.5 conjugates.

3.2. Experimental section

3.2.1. Materials

EGF consisting of 53 amino acid with a molecular weight of 6215 Da was obtained from Sigma (St. Louis, MO). Cy5.5 N-hydroxysuccinimide (NHS) ester (Cy5.5-NHS; excitation/emission: 675/695 nm) was purchased from GE Healthcare (Piscataway, NJ) and black hole quencher 3 NHS ester (BHQ3-NHS; maximum absorbance: 650 nm) was from Biosearch Technologies, Inc. (Novato, CA). PD-10 disposable columns and gradient gel were purchased from Amersham Pharmacia Biotech (Uppsala, Sweden) and Elpisbio (Taejeon, Korea), respectively. EGFR antibody was purchased from Santa Cruz Biotechnology Inc. (Santa Cruz, CA) and horseradish peroxidase-conjugated anti-mouse antibody was purchased from Waters

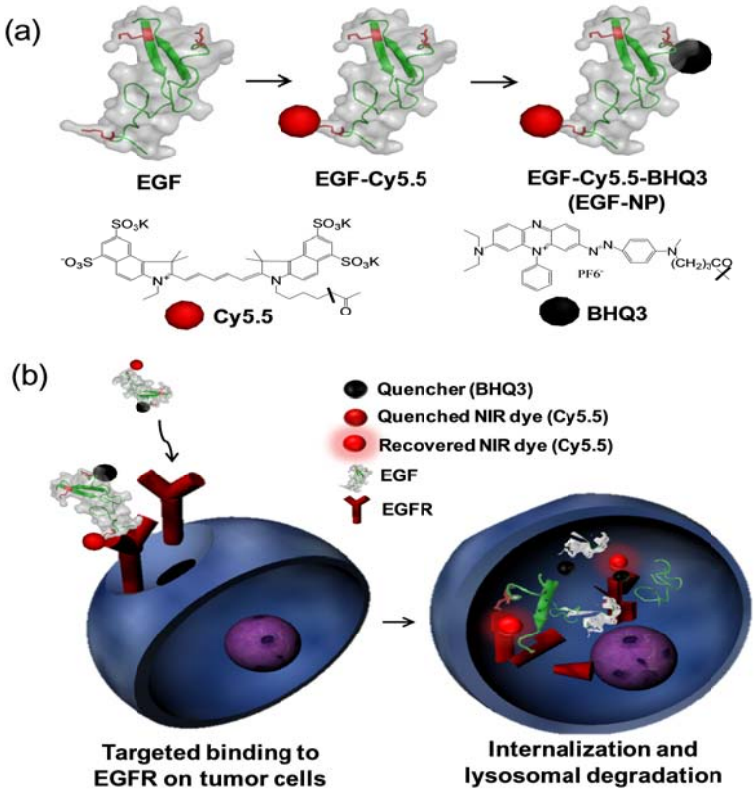

Figure 3.1. Preparation of epidermal growth factor receptor (EGFR)-targeted fluorescence activatable nanoprobes. (a) Illustration of chemical reactions used to conjugate Cy5.5 and BHQ3 onto epidermal growth factor (EGF) and chemical structures of Cy5.5 and BHQ3. Each EGF has three amine groups (N-terminal and 2 lysine) available for reaction with Cy5.5 or BHQ3. Crystal structure of EGF was drawn by the program Pymol (DeLano, W.L. The PyMOL Molecular Graphics System (2002) on World Wide Web [http://www.pymol.org]). (b) Schematic presentation for activation of EGFR-targeted fluorescence activatable nanoprobes. EGF labeled with a NIR fluorophore and a quencher (EGF-NP) binds to EGFR, which leads to cellular internalization and intracellular degradation of EGF-NP in the lysosome. Then, lysosomal degradation of EGF-NP causes separation of the fluorophore from the quencher, allowing recovered fluorescence only within the EGFR-positive cells.

(Milford, MA). Lipofectamine was purchased from Invitrogen (Carlsbad, CA). DMEM and RPMI 1640 were purchased from Gibco (Grand Island, NY). Cell Counting Kit-8 (CCK-8) and a human EGF enzyme-linked immunosorbent assay (ELISA) kit were purchased from Dojindo Molecular Technologies, Inc. (Kumamoto, Japan) and RayBiotech, Inc. (Norcross, GA), respectively.

3.2.2. Synthesis and characterization of epidermal growth factor-based nanoprobe

An aqueous solution of recombinant human EGF (0.32 μmol, 1 ml sodium bicarbonate buffer, 0.1 M, pH 9.5) was incubated with Cy5.5-NHS (0.32 μmol) in 500 μl dimethyl sulfoxide (DMSO) at room temperature (RT) for 30 min. Then, BHQ3-NHS (0.32 μmol) in 500 μl DMSO was added to the aqueous solution of EGF-Cy5.5, which was reacted at RT for 30 min. The reaction mixture was purified with preparative reverse phase-high performance liquid chromatography (RP-HPLC); 20% to 80% acetonitrile containing 0.1% trifluoroacetic acid (TFA) versus distilled water containing 0.1% TFA over 40 min at a flow rate of 1.0 ml/min. The collected fractions, EGF-Cy5.5-BHQ3 conjugates (EGF-NP), were stored at 4°C for further use.

EGF-NP was characterized using sodium dodecyl sulfate polyacrylamide gel electrophoresis (SDS-PAGE), spectrofluorometry, analytical RP-HPLC equipped with a ZORBAX 300SB-C18 column, and matrix-assisted laser

desorption/ionization-time of flight (MALDI-TOF). For SDS-PAGE, EGF, EGF-Cy5.5 and EGF-NP were mixed with an equal volume of sample buffer (0.25 M Tris [pH 6.8] containing 0.1% [w/v] bromphenol blue), respectively. The mixed products were loaded on a 15% gradient polyacrylamide gel. The gel was washed twice with 2.5% (v/v) Triton X-100 solution (30 min and 1 h each) and incubated in 50 mM Tris HCl (pH 7.5), 10 mM $CaCl_2$ and 0.2 M NaCl at 37°C for 24 h. The gel was stained with 3% (w/v) Coomassie blue, dried and scanned. Fluorescence signal of gels was imaged using a Kodak Image Station (4000 MM; Kodak, New Haven, CT). Kodak Image Station is equipped with the excitation filter for Cy5.5 and halogen lamp. Fluorescence images were obtained with an emission filter (680 to 720 nm; Omega Optical, Brattleboro, VT) and 12-bit CCD camera equipped with C-mount lens. In addition, fluorescence intensities of EGF-Cy5.5 and EGF-NP were measured using a fluorescence spectrophotometer (F-7000, Hitach, Tokyo, Japan). MALDI-TOF mass spectrometry was used to measure the molecular weight of EGF, EGF-Cy5.5 and EGF-NP using a MALDI-TOF system (Microflex LRF20, Bruker Daltonics, Bremen, Germany). Cy5.5, EGF, EGF-Cy5.5 and EGF-NP were characterized by analytical RP-HPLC; 5% to 90% acetonitrile containing 0.1% TFA versus distilled water containing 0.1% TFA over 20 min at a flow rate of 1.0 ml/min. To evaluate the de-quenching ability, EGF-NP was incubated in phosphate-buffered saline (PBS, pH 5.0) with or without lysozyme and 5% sodium dodecyl sulfate (SDS) for 20 min, and then imaged with Kodak Image Station. As control, EGFR monoclonal antibody, Cetuximab (3.3 nmol) was incubated with Cy5.5-NHS (40

nmol) in 0.1 M Na_2HPO_4 (pH 8.5) at RT for 1.5 h. Then, the reaction mixture was purified with a PD-10 column to remove unbound Cy5.5.

3.2.3. Cytotoxicity

Human breast cancer cell lines, MDA-MB-468 (high EGFR-expressing) and MDA-MB-436 cells (low EGFR-expressing) were obtained from the American Type Culture Collection (Manassas, VA).[26] MDA-MB-468 cells were cultured in DMEM containing 10% fetal bovine serum (FBS) and 100 U/ml penicillin and MDA-MB-436 cells were cultured in RPMI 1640 containing 10% FBS and 100 U/ml penicillin. Cytotoxicity was evaluated using CCK-8. In brief, MDA-MB-468 cells and MDA-MB-436 cells, respectively, were seeded in a 96-well microplate and incubated with various concentrations of the EGF-NP (0 to 50 μg/ml) for 24 h before incubation with CCK-8 solution for 2 h. Absorbance was measured at 450 nm with a plate reader. Cell viability was calculated as the percentage of viable cells relative to untreated cells.

3.2.4. Binding studies

The binding assay was performed in a 96-well microplate coated with anti-human EGF antibody from a human EGF ELISA kit. One hundred microliters of unmodified human EGF and EGF-NP were incubated for 2.5 h at RT, allowing

binding to the coated antibody. After discarding the solution and washing with wash buffer, biotinylated anti-human EGF antibody (100 μl) was incubated in the wells for 1 h at RT. After washing with wash buffer, horseradish peroxidase-conjugated streptavidin (100 μl) was incubated in the well for 45 min at RT. After washing with wash buffer, 3,3',5,5'-tetramethylbenzidine One-Step Substrate Reagent (100 μl) was incubated for 30 min at RT in the dark. Stop Solution was added to each well, and the absorbance of the solution was measured at 450 nm.

To directly assess EGFR binding, MDA-MB-468 or MDA-MB-436 cells (1×10^5 cells/dish) were plated in 35 mm coverslip bottom dishes and then incubated overnight. EGF-NP (10 μM) was added into each well and then incubated for 6 h. For the blocking test, EGFR monoclonal antibody, Cetuximab (4.0 μM) was treated to the culture medium 72 h before EGF-NP treatment. For *in vitro* EGFR siRNA silencing, EGFR siRNA and lipofectamine 2000 were mixed for 20 min in 100 μl PBS, and then the cells were treated with siRNA-lipofectamine complexes (10 nM) for 72 h. Microscopy was performed on a Deltavision system (Applied Precision, Issaquah, WA). The sample was imaged using a microscope (IL-70, Olympus, Tokyo, Japan) equipped with a mercury arc lamp. Differential visualization of the fluorophores was achieved with 660 nm/710 nm, 360 nm/457 nm, 490 nm/528 nm filters (excitation/emission). Images were analyzed with the SoftWorRx program from Applied Precision.

3.2.5. Cellular imaging

MDA-MB-468 cells (1×10^5 cells/dish) were plated in 35 mm coverslip bottom dishes and cultured for 36 h, respectively. After washing with PBS (pH 7.4), the cells were incubated in serum-free medium containing EGF-NP (10 μg/ml) for 0, 4 or 8 h. The cells were fixed in methanol and incubated with Alexa Fluor® 488-conjugated anti-EGFR for EGFR staining, Alexa Fluor® 405-conjugated anti-LAMP-1 for lysosomal marker, or 4′,6′-diamidino-2-phenylindole hydrochloride (DAPI) for nuclear staining at RT for 10 min. Cells were observed on a Deltavision system. To visualize live cell imaging, MDA-MB-468 cells on a 35 mm coverslip bottom dishes were placed in a CO_2- and temperature-controlled chamber of a microscope. Images were captured at 5 min intervals over 90 min with a cooled charged-coupled device video camera (CoolSNAP fx CCD camera, Photometrics, Tucson, AZ). Cells were exposed for 100 ms and 5000 ms to acquire differential interference contrast (DIC) images and NIR fluorescence images, respectively. To collect cell images before and after the washing process, MDA-MB-468 cells in 35 mm coverslip bottom dishes were incubated with EGF-NP or Cetuximab-Cy5.5 for 2 h. Cell image was captured with IX81-ZDC focus drift compensating microscope (Olympus, Tokyo, Japan) equipped with a 673-nm excitation filter and a 692-nm emission filter. Then, these cells were washed twice with PBS (pH 7.4) and visualized with the same equipment.

3.2.6. *In vivo* and *ex vivo* fluorescence imaging

All animal experimental procedures were in compliance with the institutional guidelines of Korea Institute of Science and Technology and the relevant laws. MDA-MB-468 and MDA-MB-436 cells (1×10^7 cells/mouse) suspended in PBS (100 μl) were subcutaneously injected into the left flank and right flank of athymic nude mice (20 g, Institute of Medical Science, Tokyo), respectively. For *in vivo* EGFR siRNA silencing, MDA-MB-468 (1×10^7 cells/mouse) suspended in PBS (100 μl) were subcutaneously injected into both the left and right flanks of athymic nude mice. When tumors reached a size of approximately 5 mm in diameter, EGF-NP (100 μg/100 μl PBS/mouse) was intravenously injected via a tail vein into the mice either directly or following pretreatment with siRNA complex. EGFR siRNA and lipofectamine 2000 were mixed for 20 min in 100 μl PBS, and then EGFR siRNA-lipofectamine complexes were intratumorally injected into the MDA-MB-468 tumor in the right flank 1 day before intravenous EGF-NP injection. For comparison study of *in vivo* biodistribution and tumor accumulation of EGF-NP and Cetuximab-Cy5.5, EGF-NP (300 μg/100 μl PBS/mouse) and Cetuximab-Cy5.5 (300 μg/100 μl PBS/mouse) were intravenously injected via the tail vein into the mice. *In vivo* NIR fluorescence tomographic images were acquired with an eXplore Optix system (ART Advanced Research Technologies Inc., Montreal, Canada).[27] Imaging was performed at a predetermined post-injection time point and the total fluorescence intensity in tumor was calculated with the region of interest analysis of

Analysis Workstation software (ART Advanced Research Technologies Inc.). For *ex vivo* NIR fluorescence imaging, tumors were excised and imaged with a Kodak Image Station at 3 h post-injection of EGF-NP.

3.2.7. Histological and Western blot analyses

Three hours after probe injection, each excised tumor was divided into 2 pieces. One was fixed in 4% (v/v) buffered formalin and then embedded in paraffin for hematoxylin and eosin (H&E) staining and immunohistochemistry (IHC). The other was embedded in optimal cutting temperature compound for cryo-section preparation and further fluorescence microscopic imaging. The paraffin-embedded specimens were cut into 5 μm-thick sections and stained with H&E. For immunohistochemical analyses, 5 μm-thick sections were stained with primary antibodies against EGFR. The staining signals were developed with a Histostain®-Plus Kit (Invitrogen). Harris's hematoxylin was used for counterstaining. The 8 μm-thick frozen sections were prepared for fluorescence microscopic imaging of Cy5.5 and DAPI. The sections were observed under the microscope without any histological stains.

Cell extract was clarified by centrifugation at 4°C (15000 g, 10 min). The cells were resuspended in cold lysis buffer (50 mM Tris-HCl, pH 8.0, 150 mM NaCl, 1% Nonidet P-40) containing protease inhibitor cocktail for 30 min. Protein extracts

were clarified by centrifugation at 4°C (15000 g, 30 min). Protein extracts were loaded onto SDS-PAGE, and gels were then transferred to a nitrocellulose membrane using an iBLOT system (Invitrogen, Carlsbad, CA). The membrane was blocked with 5% milk in Tris buffered saline with Tween 20 (TBST) at RT for 1 h and then incubated with primary antibody (EGFR antibody) at RT for 1 h. The membrane was washed three times (15 min each) and then incubated with horseradish peroxidase-conjugated anti-mouse antibody in TBST for 30 min. Immunoreactivity was visualized using enhanced chemiluminescence.

3.2.8. Statistical analysis

Values are expressed as means ± standard deviation. A one-way analysis of variance (ANOVA) was used for the comparison of continuous variables between groups. $P < 0.05$ was considered statistically significant.

3.3. Results

3.3.1. Preparation of epidermal growth factor-based nanoprobe

The EGF-NP was developed by a two-step conjugation of Cy5.5 and BHQ3 onto EGF. The procedure of EGF-NP synthesis was monitored by HPLC, mass spectroscopy and SDS-PAGE. Each EGF has three amine groups (N-terminal and 2

lysine) available for reaction with Cy5.5-NHS or BHQ3-NHS. As seen in the crystal structure of EGF-NP (Figure 3.1 a), three amine groups are exposed on the surface of EGF, allowing easy conjugation with Cy5.5-NHS or BHQ3-NHS. After a two-conjugation process with Cy5.5-NHS or BHQ3-NHS, the resulting product was purified from unbound fluorophores using a PD-10 column. HPLC results of purified EGF-NP demonstrated successful elimination of unbound Cy5.5 or BHQ3 (Figure 3.2). Mass spectrometry showed a peak at 7270 Da in EGF-Cy5.5 and at 8184 Da in EGF-NP, respectively, indicating that approximately 1 molecule of Cy5.5 and 1 molecule of BHQ3 were attached to 1 EGF molecule in the EGF-NP (Figure 3.3 a). SDS-PAGE showed that Cy5.5 and BHQ3 were covalently conjugated to the EGF molecules in the EGF-Cy5.5 and EGF-NP groups (Figure 3.3 b). With the same Cy5.5 concentration, EGF-NP was found to have a quenched fluorescence effect in PBS compared to EGF-Cy5.5 (Figure 3.3 c).

3.3.2. Characterization and cellular imaging of epidermal growth factor-based nanoprobe

Fluorescence recovery of EGF-NP was evaluated by adding lysozyme, one of the proteolytic enzymes found in lysosomes, and 5% SDS. EGF-NP was well dispersed and quenched in the PBS (Figure 3.4 a). After exposure to lysozyme and SDS for 20 min in RT, the fluorescence intensity of EGF-NP increased 3.5 ± 0.6 fold (Figure 3.4). This activation by lysozyme and SDS shows the potential of cellular

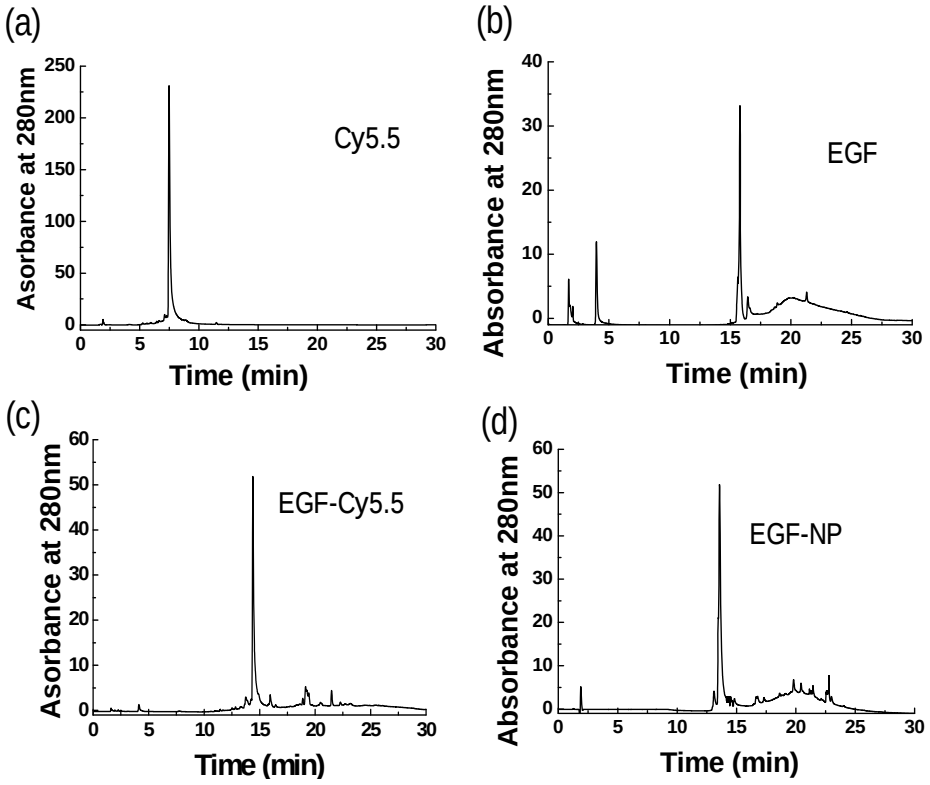

Figure 3.2. HPLC profiles of (a) Cy5.5, (b) epidermal growth factor (EGF)-Cy5.5, (c) EGF, (d) epidermal growth factor-based nanoprobe (EGF-NP). The signal is detected at 280 nm.

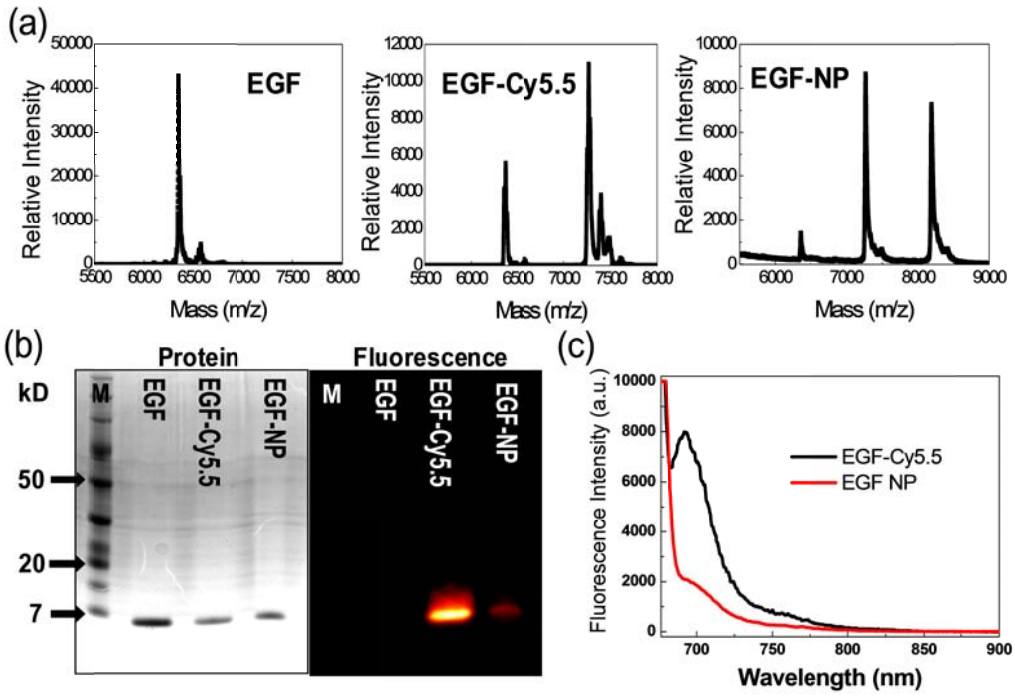

Figure 3.3. Monitoring of epidermal growth factor (EGF)-based nanoprobe (EGF-NP) synthesis. (a) MALDI-TOF mass spectrometry of EGF, EGF-Cy5.5 and EGF-NP. (b) SDS-PAGE analysis for EGF, EGF-Cy5.5 and EGF-NP shows that Cy5.5 and BHQ3 are covalently conjugated to EGF molecules (6.2 kDa, left). The fluorescence intensity of EGF-NP was substantially declined compared to EGF-Cy5.5, which means EGF-NP was quenched (right). (c) Fluorescence emission spectra of EGF-Cy5.5 and EGF-NP.

fluorescence recovery after internalization and lysosomal degradation of EGF-NP. To evaluate the cytotoxic effect of EGF-NP in high (MDA-MB-468) or low EGFR-expressing cells (MDA-MB-436), a cell viability assay was performed using CCK-8 solution. EGF-NP exhibited cell viability > 95% against MDA-MB-468 cells at concentrations lower than 10 μg/ml and against MDA-MB-436 cells at concentrations up to 50 μg/ml (Figure 3.4).

In this study, MDA-MB-436 cells and MDA-MB-468 cells were used as low EGFR-expressing cells and high EGFR-expressing cells, respectively. When EGF-NP were treated, fluorescence seen in MDA-MB-468 cells was stronger than that in MDA-MB-436 cells (Figure 3.5 a). Tumor cells were monitored using live cell imaging microscopy as time passed. MDA-MB-468 cells showed gradually increasing NIR fluorescence depending on the EGF-NP incubation time, enabling clear visualization of the probe activation process in cells (Figure 3.5 b).

Upon EGF-NP treatment, MDA-MB-468 cells exhibited a low background fluorescence signal without washing (Figure 3.5 c). Of course, EGF-NP provides a higher contrast image after washing with buffer, compared to that before washing. EGFR monoclonal antibody, Cetuximab conjugated with Cy5.5 (Cetuximab-Cy5.5) also produced a strong fluorescence signal in cells following washing. However, cells without the washing process produced a high background fluorescence signal. The low background signals caused after EGF-NP treatment allow real-time imaging in live cells.

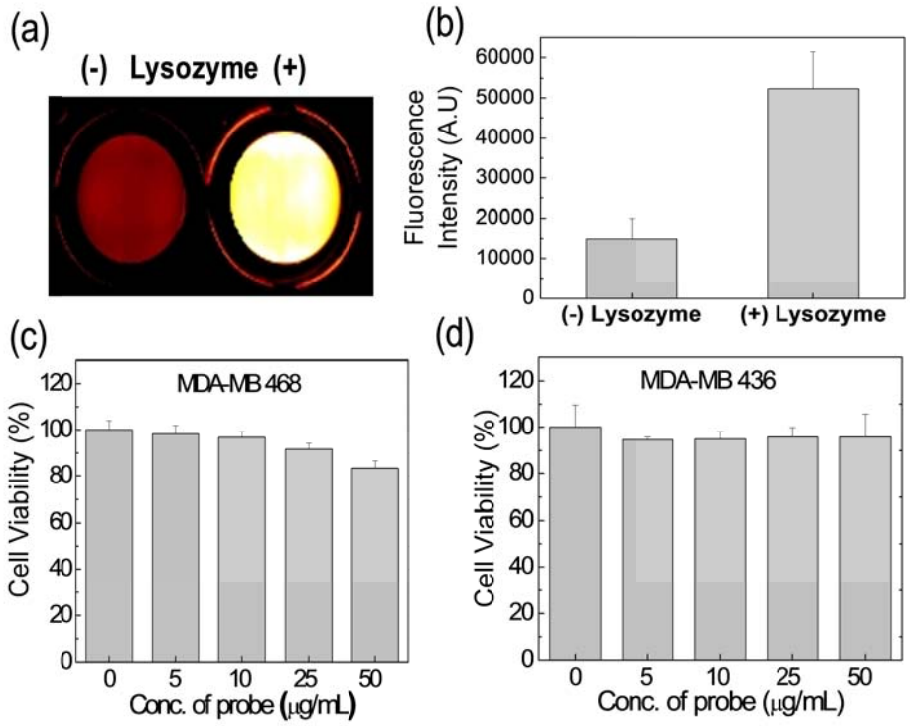

Figure 3.4. De-quenching and cytotoxicity of epidermal growth factor-based nanoprobe (EGF-NP). (a) Fluorescence image of EGF-NP in phosphate buffered saline (PBS) with or without lysosyme and 5% sodium dodecyl sulfate (SDS). In PBS without lysosome and SDS, EGF-NP was quenched. After exposure to lysozyme and SDS for 20 min in room temperature, fluorescence intensity of EGF-NP increased 3.5-fold. (b) Fluorescence intensity of (a). *In vitro* cellular cytotoxicity of EGF-NP using the Cell Counting Kit-8 assay in (c) MDA-MB-468 and (d) MDA-MB-436 cells.

3.3.3. Probe specificity for epidermal growth factor receptor

EGF-NP has affinity and specificity required for imaging cellular EGFR. Three amine groups in each EGF can be conjugated with Cy5.5 or BHQ3, but can also deteriorate EGF capacity to bind to EGFR. Therefore, ELISA-based binding assay for anti-human EGF antibody was performed with various concentrations of unmodified EGF and EGF-NP (0.8 to 200 pg/ml) (Figure 3.6).[19] Compared to unmodified EGF, EGF-NP showed lower binding affinity for anti-EGF antibody. However, EGF-NP exhibited comparable binding affinity for anti-EGF antibody, which means that the fluorophore conjugation process onto EGF does not substantially deteriorate the capacity of EGF-NP to bind to EGFR. However, this assay does not directly measure EGFR binding. To further evaluate EGFR-binding affinity of EGF-NP directly, cellular binding studies were done in MDA-MB-468 cells. Pretreatment of Cetuximab, EGFR monoclonal antibody, to MDA-MB-468 cells importantly blocks binding of ligand, resulting in significantly reduced cellular fluorescence.

3.3.4. Intracellular location of activated epidermal growth factor-based nanoprobe

EGF-NP is importantly activated in the lysosome of the cells. EGF-NP showed fluorescence signals in the cytoplasm 4 h after probe treatment in MDA-MB-468 cells, whereas EGF-Cy5.5 conjugate exhibited fluorescent signals at the cell surface as early as 5 min after incubation in MDA-MB-468 cells. To display whether the

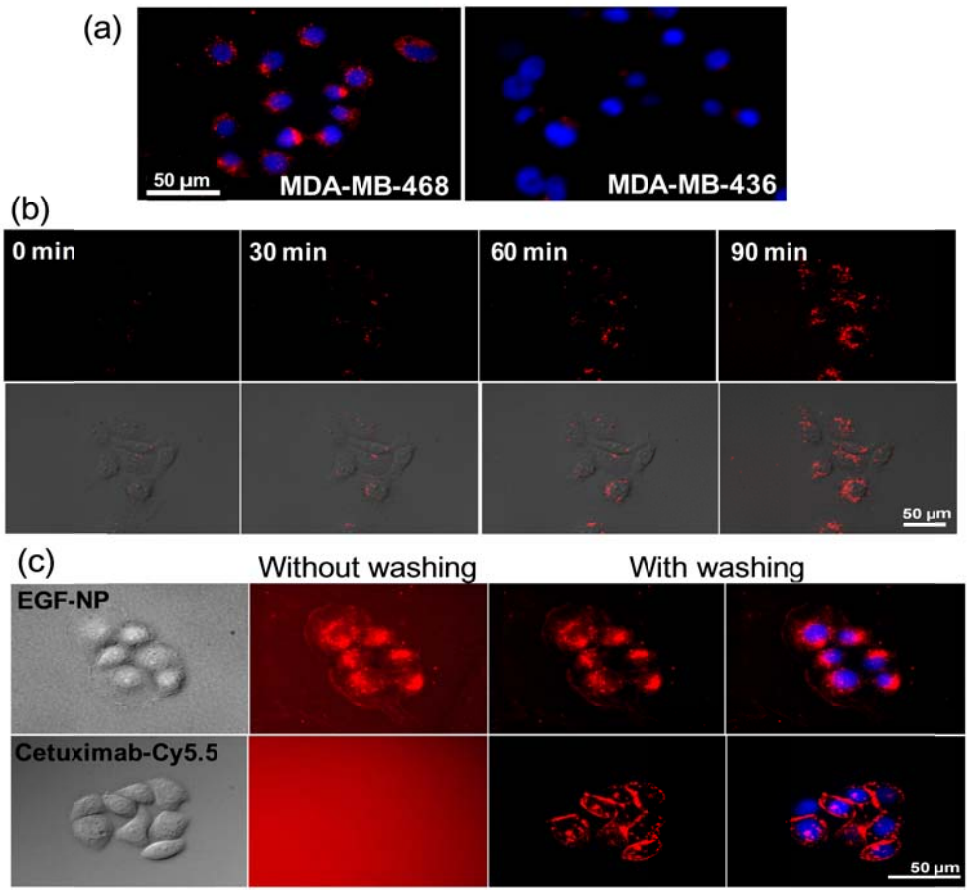

Figure 3.5. Cellular imaging of epidermal growth factor-based nanoprobe (EGF-NP) activation process. (a) Cellular images in MDA-MB-468 and MDA-MB-436 cells after treatment of EGF-NP (red) for 6 h. Nuclei were counterstained with DAPI (blue). (b) Cellular imaging of EGF-NP activation process in MDA-MB-468 cells. Cells incubated with EGF-NP (10 μM, red) were imaged at 5 min intervals over 90 min. (c) Cellular imaging before and after washing. Cells incubated with EGF-NP (red) or Cetuximab-Cy5.5 (red) for 2 h were imaged with a fluorescence microscope. Then, the same cells were washed twice with phosphate buffered saline (pH 7.4) and visualized by microscope. Cells undergoing the washing process were also stained with DAPI (blue).

fluorescent recovery of EGF-NP occurs in cell's lysosome, the cells were incubated with LAMP-1 (a lysosomal marker). The fluorescence dots from EGF-NP well-matched with LAMP-1 fluorescence signals, suggesting that lysosomal degradation causes the fluorescence recovery of EGF-NP.

3.3.5. *In vivo* fluorescence imaging in tumor-bearing mice

Intravenous injection of EGF-NP into tumor-bearing mice induced higher NIR fluorescence intensity in high EGFR-expressing tumors than in low EGFR-expressing tumors. After intravenous injection of EGF-NP into tumor-bearing mice, a strong fluorescence signal was detected from MDA-MB-468 tumors on the left flank as early as 30 min, and diminished after 1 h (Figure 3.7 a). Meanwhile, the NIR fluorescence signal from MDA-MB-436 tumors on the right flank of the mice was relatively faint, compared to that of MDA-MB-468 tumors on the left flank. To further assess the results of *in vivo* imaging, tumors were excised 3 h post-injection of EGF-NP. In the NIR *ex vivo* image, MDA-MB-468 tumor exhibited a stronger fluorescence signal, compared to the MDA-MB-436 tumor (Figure 3.7 b). Distinct fluorescence signals appeared from high EGFR-expressing tumor as early as 30 min after intravenous injection of EGF-NP, which indicates that this system can be a rapid cancer detection method.

Intravenous injection of EGF-NP into tumor-bearing mice induced higher NIR fluorescence intensity in high EGFR-expressing tumors than in low EGFR-

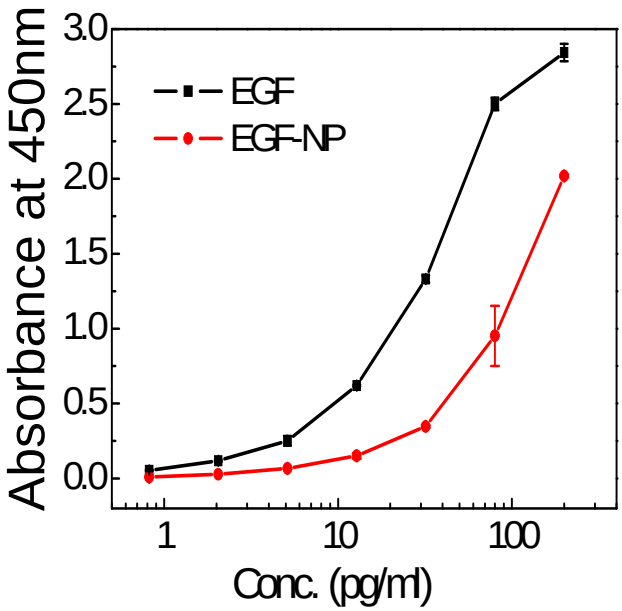

Figure 3.6. Binding assay showing the affinity of unmodified human epidermal growth factor (EGF) and EGF-based nanoprobe (EGF-NP) to anti-EGF antibody.

expressing tumors. After intravenous injection of EGF-NP into tumor-bearing mice, a strong fluorescence signal was detected from MDA-MB-468 tumors on the left flank as early as 30 min, and diminished after 1 h (Figure 3.7 a). Meanwhile, the NIR fluorescence signal from MDA-MB-436 tumors on the right flank of the mice was relatively faint, compared to that of MDA-MB-468 tumors on the left flank. To further assess the results of *in vivo* imaging, tumors were excised 3 h post-injection of EGF-NP. In the NIR *ex vivo* image, MDA-MB-468 tumor exhibited a stronger fluorescence signal, compared to the MDA-MB-436 tumor (Figure 3.7 b). Distinct fluorescence signals appeared from high EGFR-expressing tumor as early as 30 min after intravenous injection of EGF-NP, which indicates that this system can be a rapid cancer detection method.

Furthermore, administration of EGFR siRNA lowered the fluorescence intensity of EGF-NP in MDA-MB-468 tumors (Figure 3.8). EGFR siRNA was intratumorally injected into the tumor on the right flank 1 day before EGF-NP administration. Fluorescence intensity in non-treated tumors on the left flank was significantly higher ($p < 0.05$) than that in siRNA-treated tumors on the right flank of the mice at 1, 3 and 6 h after EGF-NP treatment. To further evaluate the findings from *in vivo* images, the extracted tumors were examined with a Kodak Image Station and by histology. Higher NIR fluorescence intensity was clearly observed in non-treated extracted tumors over siRNA-treated extracted tumors, which was consistent with *in vivo* optical imaging. Tumor sections were also analyzed by histology and fluorescence microscopy. H&E staining demonstrated similar carcinoma growth in

both non-treated and siRNA-treated tumors. IHC for EGFR antibody showed strong EGFR expression in non-treated tumors and significant EGFR gene silencing in siRNA-treated tumors. Fluorescence images also demonstrated that Cy5.5 fluorescence of EGF-NP from non-treated tumor tissues was significantly higher than that from siRNA-treated tumor tissues.

Signal accumulation of EGF-NP in EGFR expressing tumors was much faster than that of the Food and Drug Administration (FDA)-approved EGFR monoclonal antibodies conjugated with the same NIR fluorophore (Cy5.5). FDA-approved monoclonal antibodies conjugated with NIR fluorophores have been used as imaging agents.[28,29] Therefore, EGFR antibody and EGF-NP conjugated with the same NIR fluorophore were compared as imaging agents by *in vivo* distribution and tumor accumulation. First, Cetuximab-Cy5.5 conjugates and EGF-NP were intravenously injected into the tail vein of MDA-MB-468 tumor-bearing mice, respectively. After administration of both agents, fluorescent signal in tumors increased over time (Figure 3.9 a). The EGF-NP signal in the tumor peaked within the first 12 h of the measurement, whereas the Cetuximab-Cy5.5 signal slowly increased and reached its highest level at 5 to 9 days (Figure 3.9 b).

3.4. Discussion

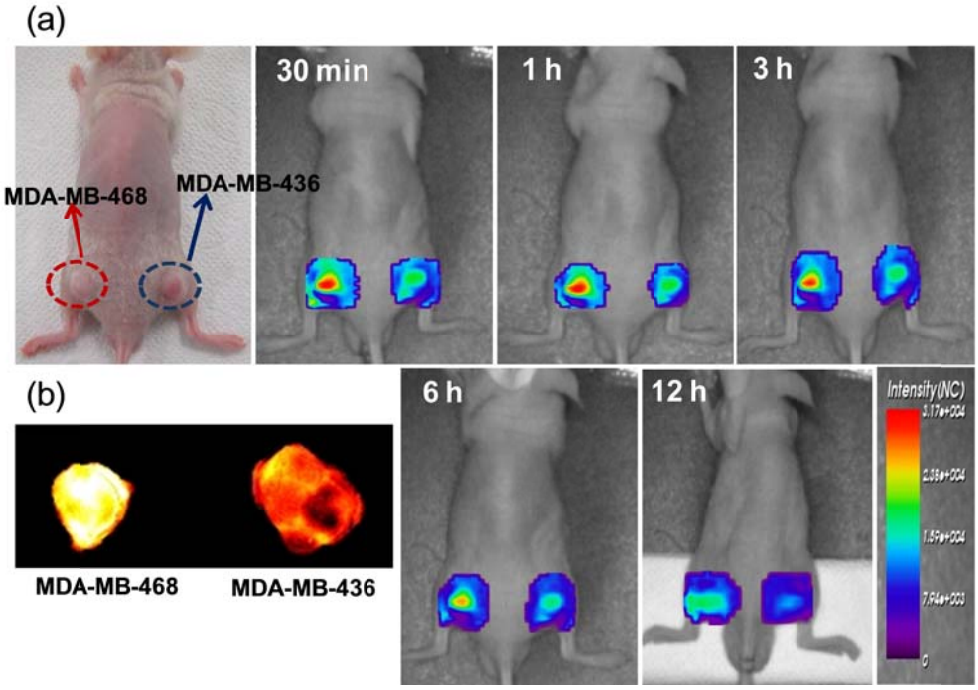

Figure 3.7. *In vivo* and *ex vivo* near infrared (NIR) fluorescence images of MDA-MB-468 and MDA-MB-436 tumors (n=5). (a) *In vivo* NIR fluorescence tomographic images of subcutaneous MDA-MB-468 and MDA-MB-436 tumor-bearing mice 30 min, 1, 3, 6 and 12 h after intravenous injection of the epidermal growth factor (EGF)-based nanoprobe (EGF-NP). Higher NIR fluorescence intensity was visualized in MDA-MB-468 tumors compared to MDA-MB-436 tumors. (b) NIR fluorescence images of excised tumors from mice at 3 h post-injection of EGF-NP.

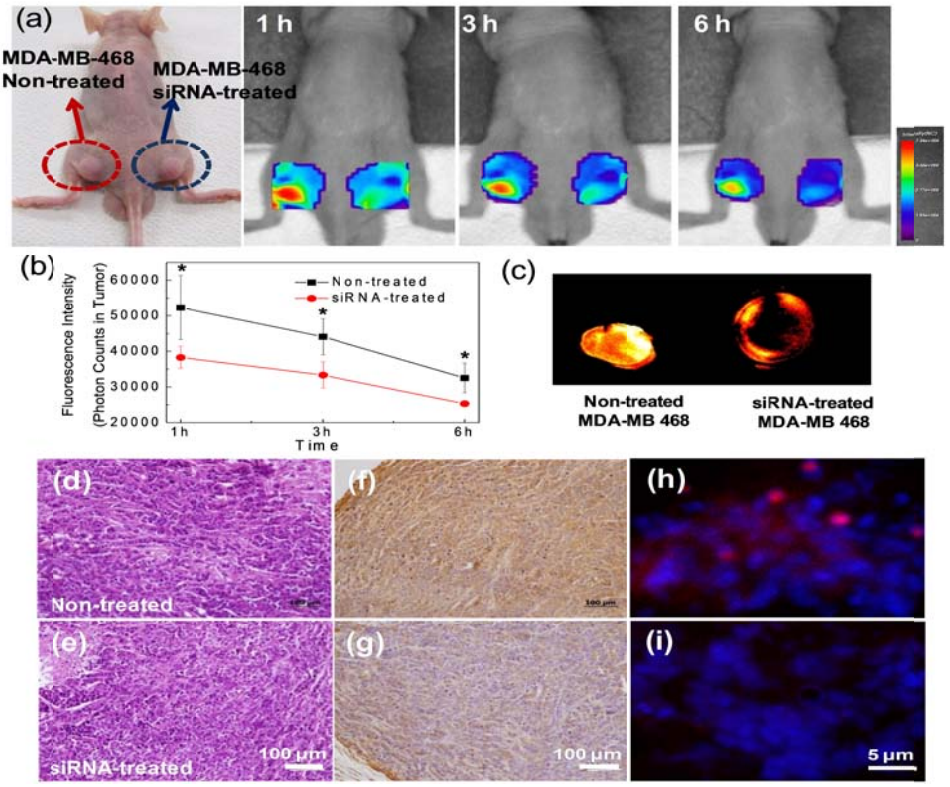

Figure 3.8. NIR fluorescence images and histology of tumor-bearing mice intravenously injected with EGF-NP and pretreated with or without EGFR siRNA. EGFR siRNA was intratumorally injected into the tumor on the right flank 1 day before EGF-NP administration. (a) *In vivo* NIR fluorescence tomographic images of subcutaneous MDA-MB-468 tumor-bearing mice (n=4) at 1, 3 and 6 h after intravenous injection of the EGF-NP. Higher NIR fluorescence intensity was visualized in non-treated MDA-MB-468 tumors compared to siRNA-treated MDA-MB-468 tumors. (b) NIR fluorescence signal intensity in tumor region (n=4). (c) NIR fluorescence images of excised tumors from mice at 3 h post-injection of EGF-NP. (d,e) Hematoxylin and eosin staining, (f,g) immunohistochemical staining for EGF receptor (EGFR) and (h,i) fluorescence microscopy images of tumor sections.

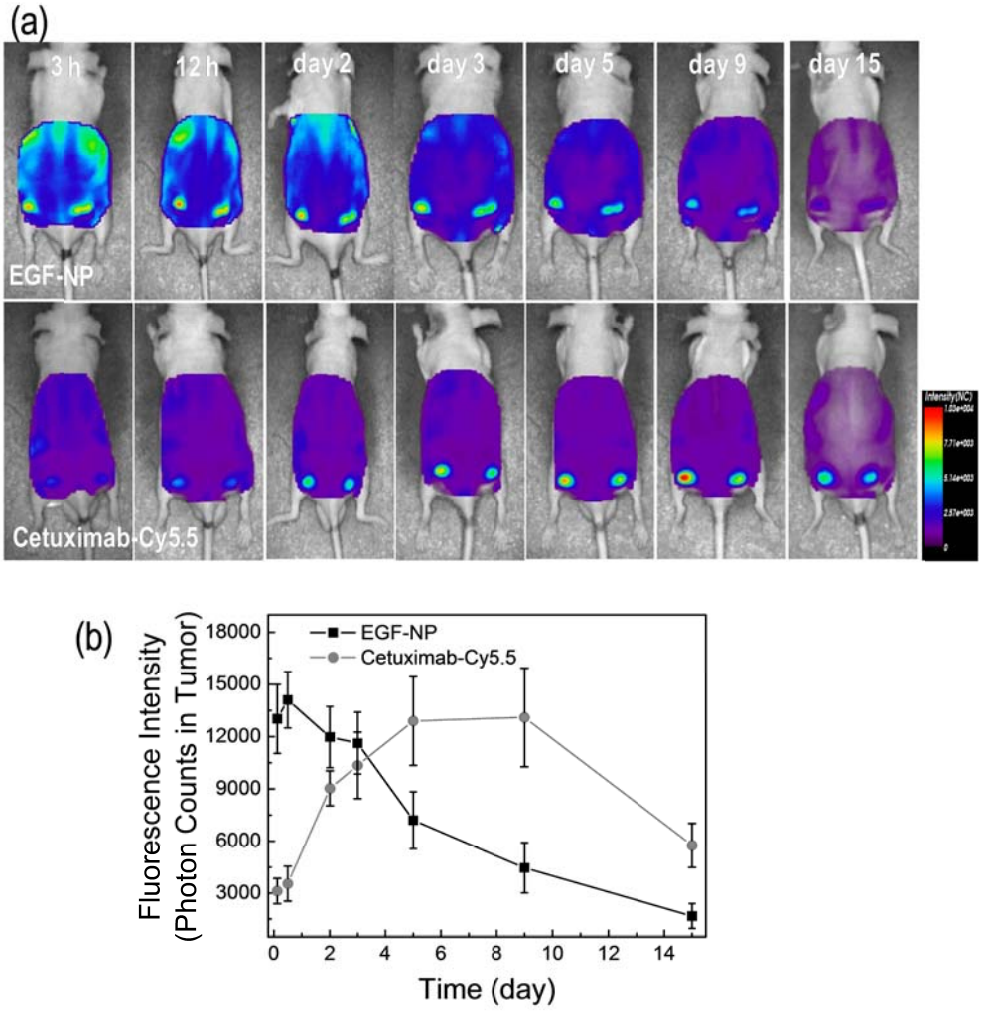

Figure 3.9. Whole body near infrared (NIR) fluorescence imaging after intravenous injection of epidermal growth factor-based nanoprobe (EGF-NP) or Cetuximab-Cy5.5 (n=3). (a) *In vivo* NIR fluorescence images of MDA-MB-468 tumor-bearing mice. (b) NIR fluorescence signal intensity in tumor region.

For EGFR-targeted fluorescently activatable imaging, it was hypothesized that 1) the fluorescence of EGF when labeled with a NIR fluorophore and a quencher would be strongly quenched when outside the target cells, 2) binding to EGFR would lead to cellular internalization and intracellular degradation of EGF-NP in the lysosome, and 3) lysosomal degradation of EGF-NP would cause separation of the fluorophore from the quencher, allowing a recovered, strong fluorescence signal only within the EGFR-positive cells (Figure 3.1). This newly designed EGF-NP is hypothesized to have strongly quenched fluorescence in the blood stream, via the quenching effect between dyes and quenchers, but after cellular internalization and lysosomal degradation the quenched EGF-NP can boost strong NIR fluorescence intensity.

Optical imaging probes are used to distinguish the target tumor by taking the surrounding background as a reference.[30] Therefore, it is important to increase the signal in the target tumor cells or tissues while decreasing the signal in the surrounding background to improve the efficiency of these probes. An activatable system using the fluorophore-quencher pair emits low to no fluorescence signal in the quenched state, because the emitting light from the fluorophore is absorbed by the quencher via fluorescence resonance energy transfer (FRET).[31] This fluorescence activatable effect is an important contribution to the optical probe, because it keeps background signals low, while displaying fluorescent signals in the target cells, thereby resulting in sensitive detection.

The mechanism of fluorescent recovery of activatable EGF-NP involves a series

of events; EGFR binding, cellular internalization, and lysosomal degradation. EGFR-EGF complex is usually internalized and undergoes degradation by lysosomal proteases in the lysosome after EGF binds to the EGFR.[32,33] Similar to EGF-EGFR complex, EGF-NP is hypothesized to bind to EGF receptor, be internalized, and be degraded in the cellular lysosome. In the present study, EGF-NP obviously showed the capability to bind to the EGFR. Moreover, NIR fluorescence signal of EGF-NP was recovered in the presence of lysozyme, one of the proteases found in lysosomes, and SDS, (Figure 3.4), and fluorescence dots from EGF-NP in cellular imaging matched with lysosomal marker fluorescence signals. Developing an imaging probe monitoring the mechanism can help to pinpoint the source causing the cancer of specific patients.

EGF-NP specifically targets EGFR-positive tumor cells. A more intense fluorescent intracellular signal was observed in MDA-MB-468 cells than in MDA-MB-436 cells after EGF-NP treatment (Figure 3.5). Furthermore, EGFR siRNA pretreatment in high EGFR-expressing MDA-MB-468 cells resulted in specific knockdown of the EGFR gene and subsequent decrease of fluorescent signal from EGF-NP. This supports that fluorescence recovery of EGF-NP is likely due to specific binding of EGF-NP to EGFR and internalization into EGFR-positive cells. *In vivo* specific targeting of EGF-NP to EGFR-positive tumor cells was demonstrated by higher NIR fluorescence intensity in high EGFR-expressing tumors over low EGFR-expressing tumors (Figure 3.7). In addition, NIR fluorescence signal from siRNA-treated MDA-MB-468 tumors was significantly

lowered compared to that of non-treated MDA-MB-468 tumor (Figure 3.8). Therefore, both *in vitro* cellular imaging and *in vivo* optical imaging support that EGF-NP specifically targets EGFR-positive tumor cells.

In addition, EGF-NP was also cleared more quickly from the body compared to Cetuximab-Cy5.5. In literature, two different radiolabelled imaging agents, EGF (Mr, 6 kDa) labeled with ^{111}In (EGF-^{111}In) and EGFR monoclonal antibody (Mr, 150 kDa) labeled with ^{111}In (MAb-^{111}In), were compared for their biodistribution after being systemically injected into EGFR-expressing tumor-bearing mice.[34] EGF-^{111}In was rapidly cleared from the blood in the mice and achieved < 0.2% of the injected dose (% ID/g) in the blood at 72 h after injection. On the other hand, MAb-^{111}In was eliminated more slowly with 3% at 72 h post-injection. Slow blood clearance of MAb-^{111}In was attributed to its large molecular weight, which hampers its filtration at the kidney glomerulus. Proteins larger than 60 kDa are known to be non-filtered through the kidney.[35] Despite rapid blood clearance of EGF-NP, the imaging agent enables clear visualization of the tumor 12 h post-injection. A short lag time between injection and imaging combined with a sufficient imaging contrast is advantageous, especially for monitoring applications such as monitoring of EGFR expression during a course of treatment. This short lag time facilitates repeated imaging acquisition within a short time frame. In addition, rapid clearance of the imaging probe can lessen safety concerns.

3.5. Conclusions

Development and characterization of an EGFR-targeted, fluorescently labeled and internally quenched probe (EGF-NP) were presented in this study. This probe is based on a natural ligand of EGFR, EGF (~6 kDa). EGF-NP was easily modified with fluorophores for labeling purposes and displayed high binding affinity for EGFR *in vitro* and *in vivo*. Also, EGF-NP takes the advantage of its small molecular weight compared to an antibody-fluorophore conjugate by having both rapid tumor localization and clearance from body. EGF-NP, as a protein-based imaging probe monitoring its target receptor, mechanistically met the chief requirements, such as specific binding affinity to the target receptor, a fast clearance from the body and tissue permeability. Therefore, this diagnostic *in vivo* imaging probe can be applied to choose patients for EGFR-targeted therapy and to monitor the therapeutic efficacy of EGFR-targeted drugs.

3.6. References

1. Bai, M.; Bornhop, D. J. *Current medicinal chemistry* **2012**, *19*, 4742.

2. Moore, C. M.; Pendse, D.; Emberton, M. *Nature Clinical Practice Urology* **2009**, *6*, 18.

3. Becker, A.; Hessenius, C.; Licha, K.; Ebert, B.; Sukowski, U.; Semmler, W.; Wiedenmann, B.; Grotzinger, C. *Nature Biotechnology* **2001**, *19*, 327.

4. Li, K.; Ding, D.; Huo, D.; Pu, K.-Y.; Thao, N. N. P.; Hu, Y.; Li, Z.; Liu, B. *Advanced Functional Materials* **2012**, *22*, 3107.

5. Bhattacharyya, S.; Khan, J. A.; Curran, G. L.; Robertson, J. D.; Bhattacharya, R.; Mukherjee, P. *Advanced Materials* **2011**, *23*, 5034.

6. Gao, J.; Liu, W.; Xia, Y.; Li, W.; Sun, J.; Chen, H.; Li, B.; Zhang, D.; Qian, W.; Meng, Y.; Deng, L.; Wang, H.; Chen, J.; Guo, Y. *Biomaterials* **2011**, *32*, 3459.

7. Gao, J.; Yu, Y.; Zhang, Y.; Song, J.; Chen, H.; Li, W.; Qian, W.; Deng, L.; Kou, G.; Chen, J.; Guo, Y. *Biomaterials* **2012**, *33*, 270.

8. Bae, K. H.; Lee, K.; Kim, C.; Park, T. G. *Biomaterials* **2011**, *32*, 176.

9. Jemal, A.; Siegel, R.; Xu, J.; Ward, E. *CA: A Cancer Journal for Clinicians* **2010**, *60*, 277.

10. Ang, K. K.; Berkey, B. A.; Tu, X.; Zhang, H.-Z.; Katz, R.; Hammond, E. H.; Fu, K. K.; Milas, L. *Cancer Research* **2002**, *62*, 7350.

11. Marega, R.; De Leo, F.; Pineux, F.; Sgrignani, J.; Magistrato, A.; Naik, A. D.; Garcia, Y.; Flamant, L.; Michiels, C.; Bonifazi, D. *Advanced Functional Materials* **2013**, *23*, 3173.

12. Huang, C.-C.; Su, C.-H.; Li, W.-M.; Liu, T.-Y.; Chen, J.-H.; Yeh, C.-S. *Advanced Functional Materials* **2009**, *19*, 249.

13. Heskamp, S.; Laverman, P.; Rosik, D.; Boschetti, F.; van der Graaf, W. T. A.; Oyen, W. J. G.; van Laarhoven, H. W. M.; Tolmachev, V.; Boerman, O. C. *Journal of Nuclear Medicine* **2012**, *53*, 146.

14. Gong, H.; Kovar, J.; Little, G.; Chen, H.; Olive, D. M. *Neoplasia* **2010**, *12*, 49.

15. Van de Broek, B.; Devoogdt, N.; D'Hollander, A.; Gijs, H.-L.; Jans, K.; Lagae, L.; Muyldermans, S.; Maes, G.; Borghs, G. *ACS Nano* **2011**, *5*, 4319.

16. Bhirde, A. A.; Patel, V.; Gavard, J.; Zhang, G.; Sousa, A. A.; Masedunskas, A.; Leapman, R. D.; Weigert, R.; Gutkind, J. S.; Rusling, J. F. *ACS Nano* **2009**, *3*, 307.

17. Thomas, T. P.; Shukla, R.; Kotlyar, A.; Liang, B.; Ye, J. Y.; Norris, T. B.; Baker, J. R. *Biomacromolecules* **2008**, *9*, 603.

18. Creixell, M.; Bohórquez, A. C.; Torres-Lugo, M.; Rinaldi, C. *ACS Nano* **2011**, *5*, 7124.

19. Diagaradjane, P.; Orenstein-Cardona, J. M.; E. Colón-Casasnovas, N.;

Deorukhkar, A.; Shentu, S.; Kuno, N.; Schwartz, D. L.; Gelovani, J. G.; Krishnan, S. *Clinical Cancer Research* **2008**, *14*, 731.

20. Ke, S.; Wen, X.; Gurfinkel, M.; Charnsangavej, C.; Wallace, S.; Sevick-Muraca, E. M.; Li, C. *Cancer Research* **2003**, *63*, 7870.

21. Lee, S.; Ryu, J. H.; Park, K.; Lee, A.; Lee, S.-Y.; Youn, I.-C.; Ahn, C.-H.; Yoon, S. M.; Myung, S.-J.; Moon, D. H.; Chen, X.; Choi, K.; Kwon, I. C.; Kim, K. *Nano Letters* **2009**, *9*, 4412.

22. Ryu, J. H.; Lee, A.; Chu, J.-U.; Koo, H.; Ko, C.-Y.; Kim, H. S.; Yoon, S.-Y.; Kim, B.-S.; Choi, K.; Kwon, I. C.; Kim, K.; Youn, I. *Arthritis & Rheumatism* **2011**, *63*, 3824.

23. Ryu, J. H.; Kim, S. A.; Koo, H.; Yhee, J. Y.; Lee, A.; Na, J. H.; Youn, I.; Choi, K.; Kwon, I. C.; Kim, B.-S.; Kim, K. *Journal of Materials Chemistry* **2011**, *21*, 17631.

24. Lee, S.; Choi, K. Y.; Chung, H.; Ryu, J. H.; Lee, A.; Koo, H.; Youn, I.-C.; Park, J. H.; Kim, I.-S.; Kim, S. Y.; Chen, X.; Jeong, S. Y.; Kwon, I. C.; Kim, K.; Choi, K. *Bioconjugate Chemistry* **2011**, *22*, 125.

25. Yoon, H. Y.; Koo, H.; Choi, K. Y.; Lee, S. J.; Kim, K.; Kwon, I. C.; Leary, J. F.; Park, K.; Yuk, S. H.; Park, J. H.; Choi, K. *Biomaterials* **2012**, *33*, 3980.

26. Lacroix, M.; Leclercq, G. *Breast Cancer Research and Treatment* **2004**, *83*, 249.

27. Na, J. H.; Koo, H.; Lee, S.; Min, K. H.; Park, K.; Yoo, H.; Lee, S. H.; Park, J. H.; Kwon, I. C.; Jeong, S. Y.; Kim, K. *Biomaterials* **2011**, *32*, 5252.

28. Ogawa, M.; Regino, C. A. S.; Seidel, J.; Green, M. V.; Xi, W.; Williams, M.; Kosaka, N.; Choyke, P. L.; Kobayashi, H. *Bioconjugate Chemistry* **2009**, *20*, 2177.

29. Sailor, M. J.; Park, J.-H. *Advanced Materials* **2012**, *24*, 3779.

30. Hama, Y.; Urano, Y.; Koyama, Y.; Kamiya, M.; Bernardo, M.; Paik, R. S.; Shin, I. S.; Paik, C. H.; Choyke, P. L.; Kobayashi, H. *Cancer Research* **2007**, *67*, 2791.

31. Oishi, M.; Tamura, A.; Nakamura, T.; Nagasaki, Y. *Advanced Functional Materials* **2009**, *19*, 827.

32. Roepstorff, K.; Grandal, M. V.; Henriksen, L.; Knudsen, S. L. J.; Lerdrup, M.;

Grøvdal, L.; Willumsen, B. M.; Van Deurs, B. *Traffic* **2009**, *10*, 1115.

33. Gorden, P.; Carpentier, J. L.; Cohen, S.; Orci, L. *Proceedings of the National Academy of Sciences* **1978**, *75*, 5025.

34. Reilly, R. M.; Kiarash, R.; Sandhu, J.; Lee, Y. W.; Cameron, R. G.; Hendler, A.; Vallis, K.; Gariépy, J. *Journal of Nuclear Medicine* **2000**, *41*, 903.

35. Jia, L.; Zhang, L.; Shao, C.; Song, E.; Sun, W.; Li, M.; Gao, Y. *PLoS ONE* **2009**, *4*, 5146.

Chapter 4

Detection of lysyl oxidase activity in extracellular matrix using gold nanoprobes

4.1. Introduction

The tumor stroma is characterized by remodeling and stiffening of the extracellular matrix (ECM).[1-3] ECM comprises a heterogenous group of macromolecules, such as collagen, elastin, proteoglycans, noncollagenous glycoproteins, and elastic fibers.[4] ECM is constantly remodeling by the simultaneous synthesis and degradation of ECM components with different turnover rates. ECM stiffening depends on the collagen cross-linking. During the formation of intramolecular or intermolecular cross-linking of collagen, collagen fibers change into increasingly insoluble and show progressively incremental stiffening.[5,6]

Lysyl oxidase (LOX) is an ECM-remodeling enzyme that is frequently elevated in the tumor microenvironment.[7, 8] Specifically, LOX oxidatively deaminates (hydroxyl)lysine residues, which form the aldehyde groups, yielding allysine (Figure 4.1). By enzymatic oxidation in the telopeptides of collagen by LOX, highly reactive aldehyde groups can react with adjacent aldehyde groups, rendering intramolecular cross-linking of collagen, or can react with other ε-amino groups of (hydroxyl)lysine residues of an adjacent helix, rendering the intermolecular cross-linking of collagen. In this oxidative reaction process, hydrogen peroxide is released. Active LOX increases ECM stiffness, regulates cell migration, and promotes cancer malignancy.[9] Indeed, excessive LOX has been correlated with poor prognosis and ECM stiffness in breast, colorectal, head and neck, and prostate cancer.[10-12] Therefore, sensitive detection of LOX activity is needed.

Recently, gold nanoparticle (AuNP)-based colorimetric sensors have attracted interest as a rapid and simple detection method.[13] Stabilized AuNPs in solution present a characteristic absorption band at a specific wavelength due to plasmon resonance. This absorption band is red-shifted toward longer wavelengths by the aggregation of AuNPs, which causes that color of AuNP solution to turn from original pinkish red to blue/purple.[14] This color change can be used to detect the presence or amount of analytes that cause the selective aggregation of AuNPs.[15, 16] In this study, the AuNPs were functionalized with the LOX-sensitive hexapeptides (LOX-AuNPs), which were applied to detect LOX as a colorimetric sensor in *in vitro*, cancer cell, and tumor tissue levels (Figure 4.2). The color and absorption spectra of AuNPs in solution was monitored before and after the addition of LOX *in vitro*. The potential use of LOX-AuNPs for detecting the amount of LOX in cancer cells was investigated, which was compared with the results of Western blot analysis and a commercially available LOX assay. Finally, the potential use of LOX-AuNPs in tumor tissues was examined, and tumor tissues were further analyzed for their collagen content and their ECM stiffness.

4.2. Experimental section

4.2.1. Materials

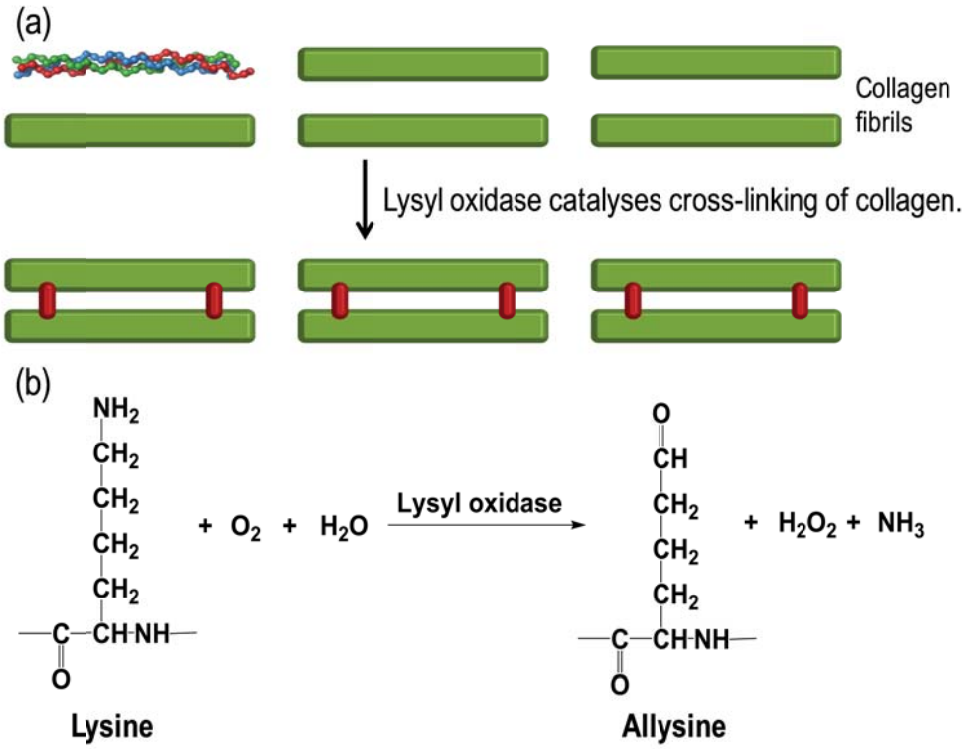

Figure 4.1. Lysyl oxidase (LOX) as an extracellular matrix-remodeling enzyme. (a) LOX oxidatively deaminates (hydroxyl)lysine residues, which forms the aldehyde groups, yielding allysine. In this reaction, hydrogen peroxide is released. (b) By enzymatic oxidation in the telopeptides of collagen by LOX, highly reactive aldehyde groups can react with adjacent aldehyde groups or other ε-amino groups of (hydroxyl)lysine residues of an adjacent helix, rendering the cross-linking of collagen.

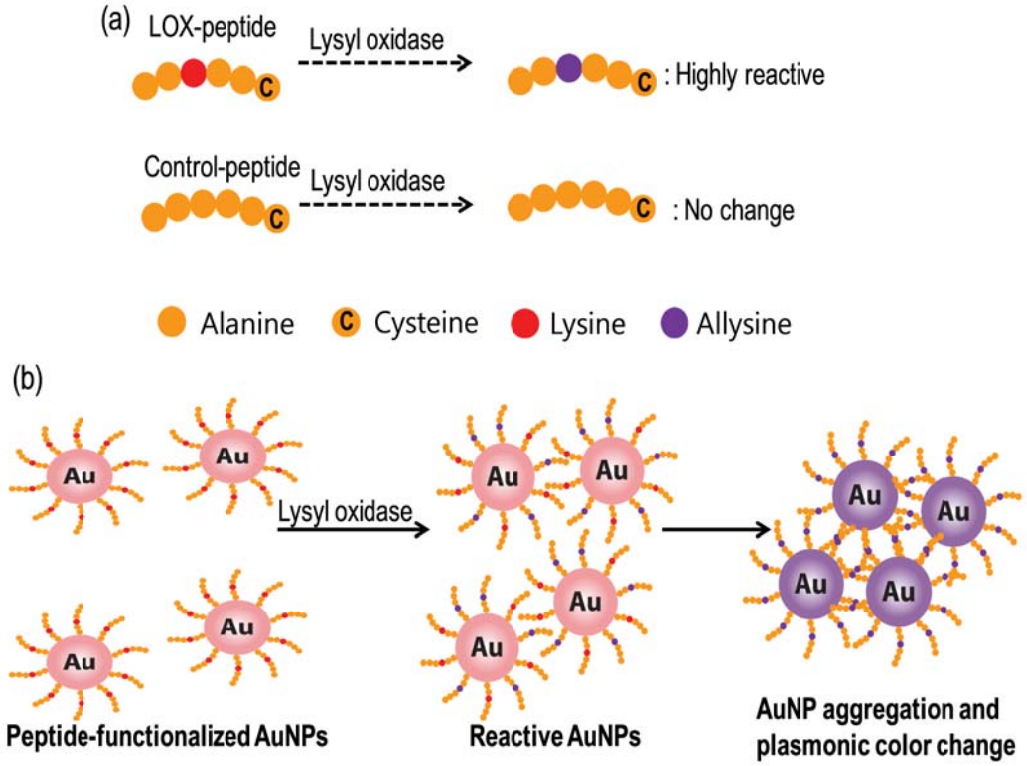

Figure 4.2. Scheme of peptide-functionalized gold nanoparticle (AuNP)-based colorimetric assay for lysyl oxidase (LOX) detection. (a) The reaction between the hexapeptide containing lysine (LOX-peptide) or hexapeptide without lysine (Control-peptide) and LOX. (b) The plasmonic coupling-based colorimetric assay for LOX detection. The color of AuNP solution turns from original pinkish red to blue/purple due to the aggregation of AuNPs.

LOX enzyme was purchased from OriGene (Rockville, MD). MMP-2 and cathepsin B enzymes were purchased from R&D Systems, Inc. (Minneapolis, MN). LOX inhibitor, β-aminopropionitrile, was purchased from Sigma-Aldrich (St. Louis, MO). Fetal bovine serum (FBS) was purchased from Invitrogen Canada (Burlington, ON, Canada), and RPMI 1640 medium was obtained from Gibco (Grand Island, NY). For Western blot analysis, anti-LOX and a horseradish peroxidase-conjugated anti-mouse antibody were purchased from Aviva Systems Biology (San Diego, CA) and Santa Cruz Biotechnology (Santa Cruz, CA), respectively. A commercially available LOX assay kit, Amplite^{TM} Fluorimetric Lysyl Oxidase Assay kit, was purchased from AAT Bioquest (Sunnyvale, CA).

4.2.2. Synthesis of gold nanoparticles

AuNPs were prepared according to the citrate reduction procedure.[17] A solution of $HAuCl_4$ (95 ml, 0.26 mM) was heated and equilibrated at 100 ^oC in a reactor. Then, sodium citrate (0.5% [w/v]) dissolved in distilled water (DW, 5 ml) was injected, and the mixture was reacted at the boiling temperature for 30 min before letting it cool to room temperature.

4.2.3. Preparation of peptide-functionalized gold nanoparticles

LOX-sensitive peptide (LOX-peptide, Ala-Ala-Lys-Ala-Ala-Cys), LOX-

insensitive peptide (Control-peptide, Ala-Ala-Ala-Ala-Ala-Cys), and LOX-insensitive peptide 2 (Control-2-peptide, Ala-Ala-Gly-Ala-Ala-Cys) were synthesized using a standard solid-phase peptide synthesis method (Peptron, Daejeon, Korea).[18] Peptide-functionalized AuNPs (1.3 nM) were prepared by mixing the freshly prepared AuNPs in DW (1 ml) with an aqueous solution of LOX-peptide or Control-peptide (5 mg/ml, 0.1 ml), yielding LOX-AuNPs or Control-AuNPs, respectively. After reacting at room temperature for 1 h, peptide-functionalized AuNPs were purified by centrifugation and washing with DW twice, and were re-dispersed in DW (1.3 nM). The dispersed AuNPs were stored at 4°C for further use.

4.2.4. Characterization of peptide-functionalized gold nanoparticles

The peptides treated with LOX enzyme were characterized by analytical reverse phase-high performance liquid chromatography (RP-HPLC); 20% to 80% acetonitrile containing 0.1% trifluoroacetic acid (TFA) versus DW containing 0.1% TFA over 30 min at a flow rate of 1.0 ml/min. Mass spectrometry was used to measure the molecular weight of the peptides treated with LOX enzyme using Varian 500-MS (Varian Inc., Palo Alto, CA). The mean diameter and size distribution of the AuNPs and LOX-AuNPs were observed with dynamic light scattering (DLS) at 25°C. UV/Vis absorbance of AuNPs or peptide-labeled AuNPs with or without various enzymes was recorded from 400 to 700 nm using UV/Vis

spectrophotometer (Optizen 2120, Mecasys, Daejeon, Korea). AuNP aggregates were observed using transmission electron microscopy (TEM, CM30 electronmicroscope, Philips, CA) operating at 80 kV. The sample solution was placed on the grid for 2 min and excess solution was blotted with filter paper. For staining, the grid was placed on a drop of 2% (w/v) uranyl acetate.

4.2.5. Sensitivity and specificity of peptide-functionalized gold nanoparticles for lysyl oxidase

The sensitivity of the LOX-AuNPs or Control-AuNPs was examined by incubating LOX-AuNPs (1.3 nM) in DW containing various concentrations (6.0, 12.0, 24.0, 48.0, and 96.0 nM) of LOX enzymes. Color change was observed, and the UV/Vis absorbance of LOX-AuNPs or Control-AuNPs was monitored. The specificity of the LOX-AuNPs was examined by incubating LOX-AuNPs (1.3 nM) in DW containing 15 nM of activated MMP, cathepsin and LOX plus LOX inhibitor. Color change and the UV/Vis absorbance of LOX-AuNPs were monitored.

4.2.6. Cell culture

Human breast cancer cell lines, MCF-7 and MDA-MB-231 were maintained in an RPMI 1640 medium containing 10% (v/v) FBS and penicillin G (100 U/ml)/streptomycin (100 μg/ml) at 37°C, 5% CO_2._MCF-7 (1×10^6 cells/dish) and

MDA-MB-231 (1×10^6 cells/dish) were plated on a 100-mm tissue culture dish. MCF-7 and MDA-MB-231 were cultured for 24, 48, or 72 h, respectively. LOX-containing conditioned media were collected from MCF-7 or MDA-MB-231.

4.2.7. Commercially available lysyl oxidase assay

A commercially available LOX activity assay kit, the Amplite™ Fluorimetric Lysyl Oxidase Assay Kit was utilized to validate the LOX-AuNPs-based results. The Amplite™ Fluorimetric Lysyl Oxidase Assay is a fluorescence signal-based method for detecting LOX. This assay utilizes a proprietary LOX substrate that can release hydrogen peroxide when reacted with LOX. In this assay, LOX activity was indirectly detected by measuring the production of hydrogen peroxide. In practice, conditioned media (50 μl) was added to the assay reaction mixture (50 μl) in 96-well plate. After incubating 30 min at 37°C, the signal was read at 576 nm by an absorbance plate reader.

4.2.8. Tumor models

All animal experimental procedures were in compliance with the institutional guidelines of Korea Institute of Science and Technology and the relevant laws. MCF-7 (1×10^6 cells/mouse) and MDA-MB-231 cells (1×10^7 cells/mouse) suspended in phosphate-buffered saline (PBS, 100 μl) were subcutaneously injected

into the left flank of athymic nude mice (20 g, Orient, Seoul, Korea), respectively. The LOX inhibitor (3 mg/kg body weight) was intraperitoneally injected every day from 14 days after the injection of tumor cells. When tumors reached 5.0 ± 0.5 mm in diameter, the tumors were excised for further analysis. For protein extraction, excised tumor tissues were grounded by liquid nitrogen, rinsed with PBS, and sonicated in lysis buffer (7 M urea, 2 M thiourea, 4% [v/v] CHAPS, 130 mM dithiothreitol, 1 mM NaF, Na_2VO_3, and a complete protein inhibitor mixture) for 20 min. The samples were then centrifuged at 9700 g for 15 min. The protein concentration in the supernatant was measured based on a Bradford assay (Bio-Rad protein assay kit; Bio-Rad, Hercules, CA).

4.2.9. Histological and Western blot analyses

Excised tumor tissues were fixed in 4% (v/v) buffered formalin, dehydrated with a graded ethanol series, and embedded in paraffin. The specimens were cut into 5 μm-thick sections and stained using the Masson's Trichrome method to detect collagen. For immunohistochemistry (IHC) analysis, sections were stained with primary antibodies against LOX. The staining signals were developed with a Histostain®-Plus Kit (Invitrogen). The nucleus was stained with 4',6-diamidino-2-phenylindole (DAPI).

For Western blot analysis, each aliquot of the cell supernatant or extracted proteins mixed with a sample buffer (0.25 M of Tris, 0.8% [w/v] sodium dodecyl sulfate, 10%

[v/v] glycerol, 0.05% [w/v] bromophenol blue, pH 6.8) was run on 10% polyacrylamide gel after boiling (10 min). Gels were transferred to a blot membrane using iBLOT (Invitrogen). Membranes were blocked with milk in Tris-buffered saline-Tween20 (TBST) at room temperature for 1 h and then incubated with anti-LOX at 4°C overnight. Three washes (15 min each) with TBST were performed, and the membranes were incubated with a horseradish peroxidase-conjugated anti-mouse antibody for 1 h in TBST and then washed (three washes, 15 min each) with TBST. β-actin was used as internal control. Immunoreactive proteins were visualized with enhanced chemiluminescence.

4.2.10. Compressive modulus measurements

Compression testing was performed on cylinidrical shape-cutting tumor tissues using an electro-metchanical driven indenter (Instron 5966) including a force transducer (a load cell of 10 N), a stepper motor, and a linear displacement transducer.[1, 19] The tangent elastic moduli of the tumor tissues were calculated from the initial linear slope in the resulting stress-strain curves.

4.2.11. Statistical analysis

Data represents the means ± standard deviation. A one-way analysis of variance was used for the comparison of variables between groups. A value of $p < 0.05$ was

considered statistically significant.

4.3. Results

4.3.1. Reactivity of lysyl oxidase-peptide for lysyl oxidase

Hexapeptide containing lysine (LOX-peptide) showed a distinct response to LOX, while hexapeptides without lysine (Control-peptide, Control-2-peptide) did not respond to LOX. LOX is known to deaminate lysine to allysine which is highly reactive. Aldehyde groups in allysine can react with adjacent aldehyde groups or with ε-amino group of a lysine residue.[20] The products before and after addition of LOX were evaluated by analytical RP-HPLC and mass spectroscopy (Figure 4.3). The HPLC profiles of the LOX-peptide after the addition of LOX showed one main peak, which is different from that before the addition of LOX. Mass spectrometry showed a peak at 575.8 Da in the product before the addition of LOX. After the addition of LOX, it showed an additional peak at 1151.3 Da, indicating the conjugation between two LOX-peptides. However, Control-peptide did not show any change in the results of HPLC and mass spectroscopy after the addition of LOX.

4.3.2. Characterization of peptide-functionalized gold nanoparticles

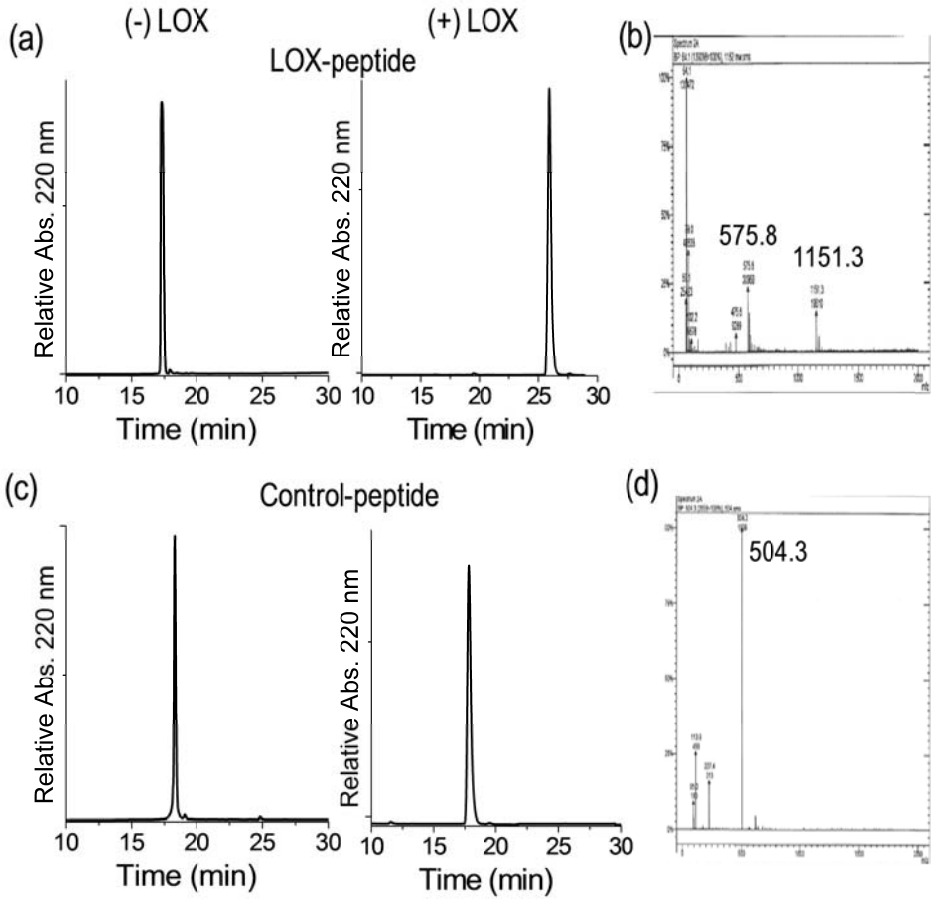

Figure 4.3. Reactivity of lysyl oxidase (LOX)-peptide for LOX. (a) HPLC profiles of the LOX-peptide before and after the addition of LOX and (b) mass spectrometry of the reaction mixture between LOX-peptide and LOX. (c) HPLC profiles of the Control-peptide before and after the addition of LOX and (d) mass spectrometry of the reaction mixture between Control-peptide and LOX.

The peptide-functionalized AuNPs were prepared in DW using LOX-peptide and Control-peptide. Because thiol groups interact strongly with AuNPs, hexapeptides used in this study were designed to contain cysteine in one side of peptide. The hydrodynamic diameter of AuNPs grew from 14.76 ± 0.38 nm in diameter to 24.76 ± 0.29 nm in diameter in DLS analysis, confirming the presence of peptides on the surface of AuNPs (Figure 4.4 a). TEM measurements showed that both AuNPs and LOX-AuNPs are spherical shape with the similar size range of 13–20 nm. In addition, the surface plasmon resonance peak of AuNPs red-shifted from 518 nm to 522 nm after being modified with LOX-peptide (Figure 4.4 b). The surface charge of AuNPs, zeta-potential was -30.0 ± 5.6 mV in AuNPs, and changed to 21.5± 0.6 mV in LOX-AuNPs (Table 4.1).

4.3.3. Detection of lysyl oxidase *in vitro*

A series of concentrations of LOX were added to LOX-AuNPs in DW (1.3 nM, 1 ml). By incubating these mixtures for 1 h, the solution color was observed and UV/Vis absorbance was monitored. The solution turned from the original pinkish red to purple (Figure 4.5 a) and the absorption spectra of the LOX-AuNPs red-shifted and broadened with increasing LOX concentrations (Figure 4.5 d). The plasmon band shifted from 522 nm at 0 nM LOX and to 592 nm at 96 nM LOX. The spectral shifts appeared at concentrations as low as 12 nM. LOX-AuNPs was found to be well-dispersed in solution before the addition of LOX in a TEM image,

Table 4.1. Hydrodynamic diameter and surface charge of gold nanoparticles (AuNPs)

Nanoparticle	Hydrodynamic diameter (nm)	Surface charge (mV)
AuNP	14.76±0.38	-30.0±5.6
LOX-AuNP	24.76±0.29	21.5±0.6

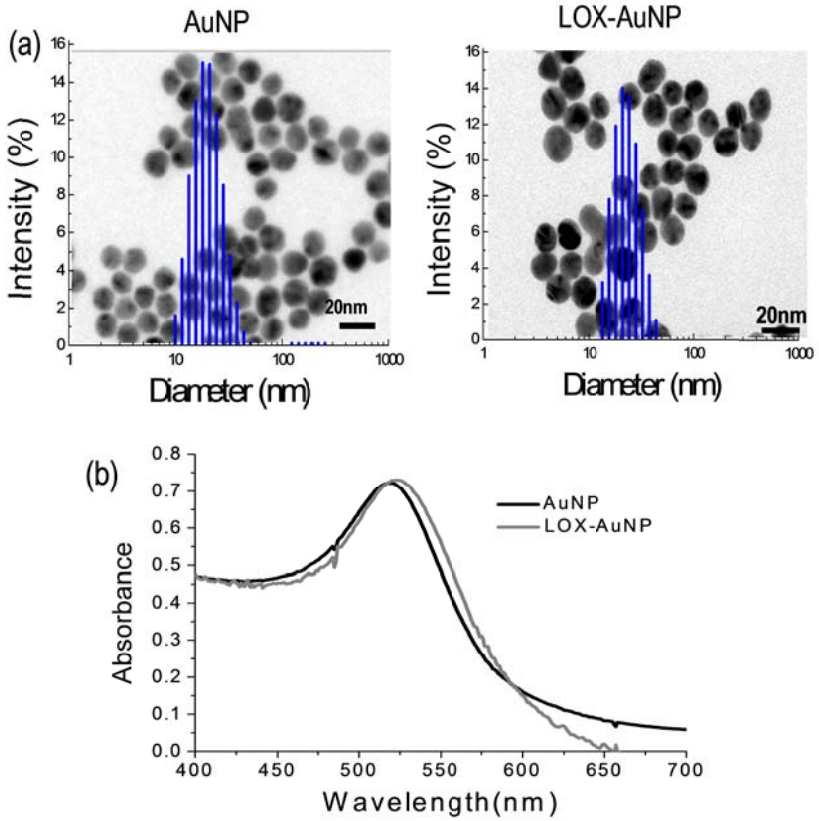

Figure 4.4. Characterization of bare gold nanoparticle (AuNP) and lysyl oxidase (LOX)-AuNP. (a) Size distribution of bare AuNP and LOX-AuNP. (b) UV/Vis spectra of bare AuNP and LOX-AuNP. (c) Transmission electron microscopy images of bare AuNP and LOX-AuNP.

whereas it was found to form aggregates in the presence of LOX (Figure 4.5). Quantitative analysis was performed by measuring the absorbance values of A650/A520. The calibration curve for LOX quantification showed the linear range (r^2 = 0.999) from 12 nM to 96 nM (Figure 4.5 e). Meanwhile, any noticeable changes in the UV/Vis spectra or color of the resulting AuNPs were not shown when other enzymes including MMP or cathepsin were added to LOX-AuNPs (Figure 4.6). In addition, pretreatment of LOX inhibitor prevented changes in the UV/Vis spectra or color of the resulting AuNPs. No change in the UV/Vis spectra or color of the resulting AuNPs was observed when a series of concentrations of LOX was added to Control-AuNPs.

4.3.4. Detection of lysyl oxidase in cancer cells

To investigate the potential use of LOX-AuNPs, they were applied to determine LOX in cancer cells with different LOX contents. MDA-MB-231 and MCF-7 cells were selected as high LOX-secreting and low LOX-secreting cells, respectively.[21] LOX is a secreted enzyme, hence, LOX detection was performed in the conditioned media using LOX-AuNPs, Western blot analysis, and a commercially available LOX assay kit. When the conditioned media after a 3-day culture of MDA-MB-231 cells were added to LOX-AuNP solution, color change and spectral shifts were more dramatic compared to that after a 3-day culture of MCF-7 cells (Figure 4.7). In addition, as the culturing periods of MDA-MB-231 cells increased from 1 day

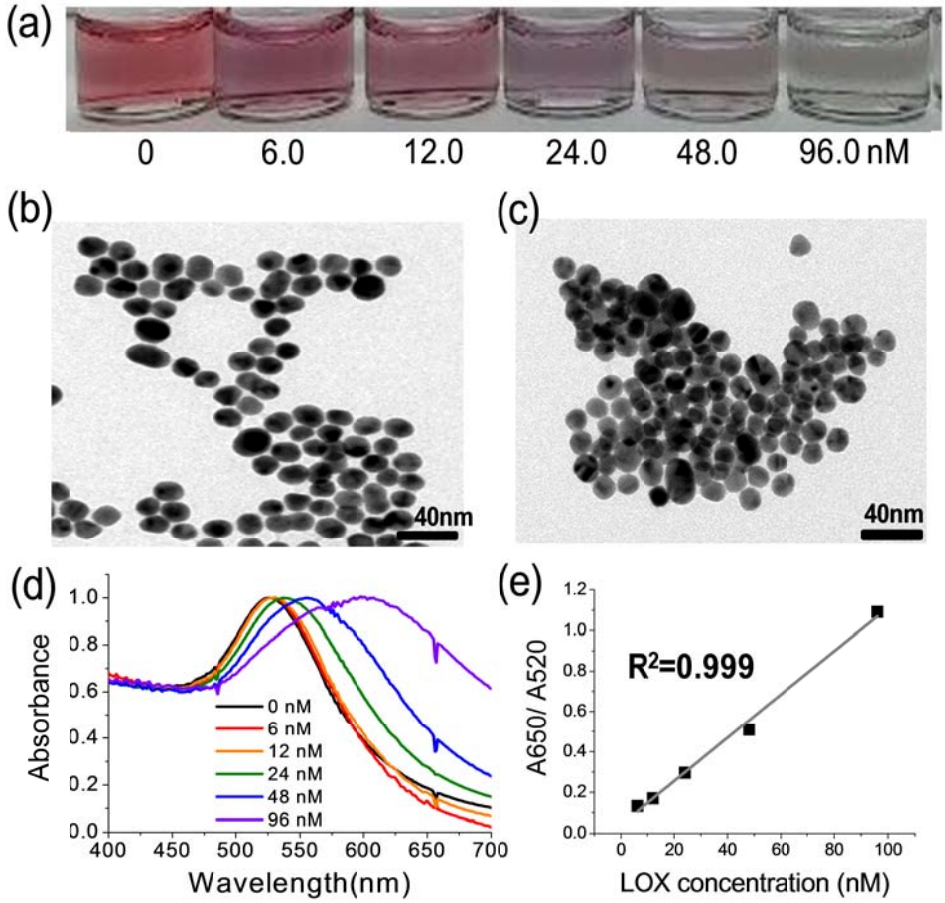

Figure 4.5. Detection of lysyl oxidase (LOX) using LOX-gold nanoparticles (AuNPs). (a) Optical micrographs of LOX-AuNPs after the addition of different concentrations of LOX. Transmission electron microscopy image of the LOX-AuNPs (b) before the addition of LOX and (c) after the addition of LOX (96.0 nM). (d) Corresponding UV/Vis absorption spectra of LOX-AuNPs with different concentrations of LOX in (a). (e) Calibration curve for LOX determination. Quantitative analysis was performed by measuring the absorbance values of A650/A520.

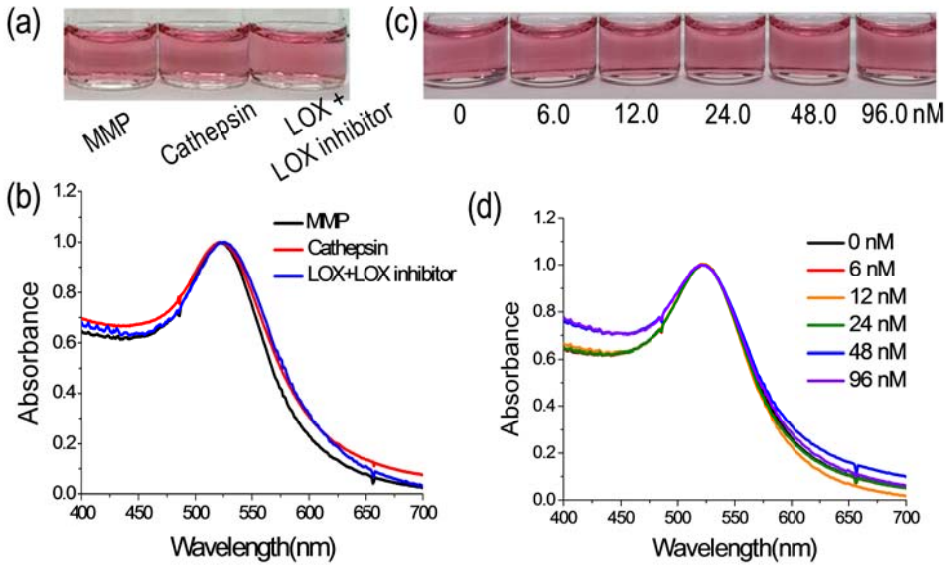

Figure 4.6. Specificity of lysyl oxidase (LOX)-gold nanoparticles (AuNPs) for LOX. (a) Optical micrographs of LOX-AuNPs after the addition of matrix metalloproteinase (MMP), cathepsin, and LOX plus LOX inhibitor. (b) Corresponding UV/Vis absorption spectra of LOX-AuNPs after the addition of MMP, cathepsin, and LOX plus LOX inhibitor. (c) Optical micrographs of Control-AuNPs after the addition of different concentrations of LOX. (d) Corresponding UV/Vis absorption spectra of Control-AuNPs after the addition of different concentrations of LOX in (d).

to 3 days, color change and spectral shifts increased as well. LOX expression in the conditioned media after a 3-day culture of MDA-MB-231 cells was barely detectable in Western blot analysis (Figure 4.7 d). LOX expression in the other conditioned media was not detected in Western blot analysis. A commercially available LOX assay, the Amplite™ Fluorimetric Lysyl Oxidase Assay is a fluorescence signal-based method for detecting hydrogen peroxide released in the reaction between a LOX substrate and LOX.[22] Importantly, LOX activity from the commercial assay revealed a very similar tendency but lowered sensitivity as measured in the LOX-AuNP assay results (Figure 4.7 e).

4.3.5. Detection of lysyl oxidase in tumor tissues

To investigate potential for the use of LOX-AuNPs, they were applied to determine LOX in tumor tissues with different LOX contents. When tumors reached 7.0 ± 0.5 mm in diameter, MDA-MB-231 tumors, MDA-MB-231 tumors treated with LOX inhibitor, and MCF-7 tumors were excised, and proteins were extracted. Western blot analysis indicated higher levels of LOX expression in MDA-MB-231 tumors, compared to those of MDA-MB-231 tumors treated with LOX inhibitor and MCF-7 tumors (Figure 4.8 a). Proteins extracted from respective tumor tissues were added to LOX-AuNP solution. Distinct color changes and spectral shifts in the plasmon band were correlated with the LOX contents analyzed by Western blot analysis (Figure 4.8).

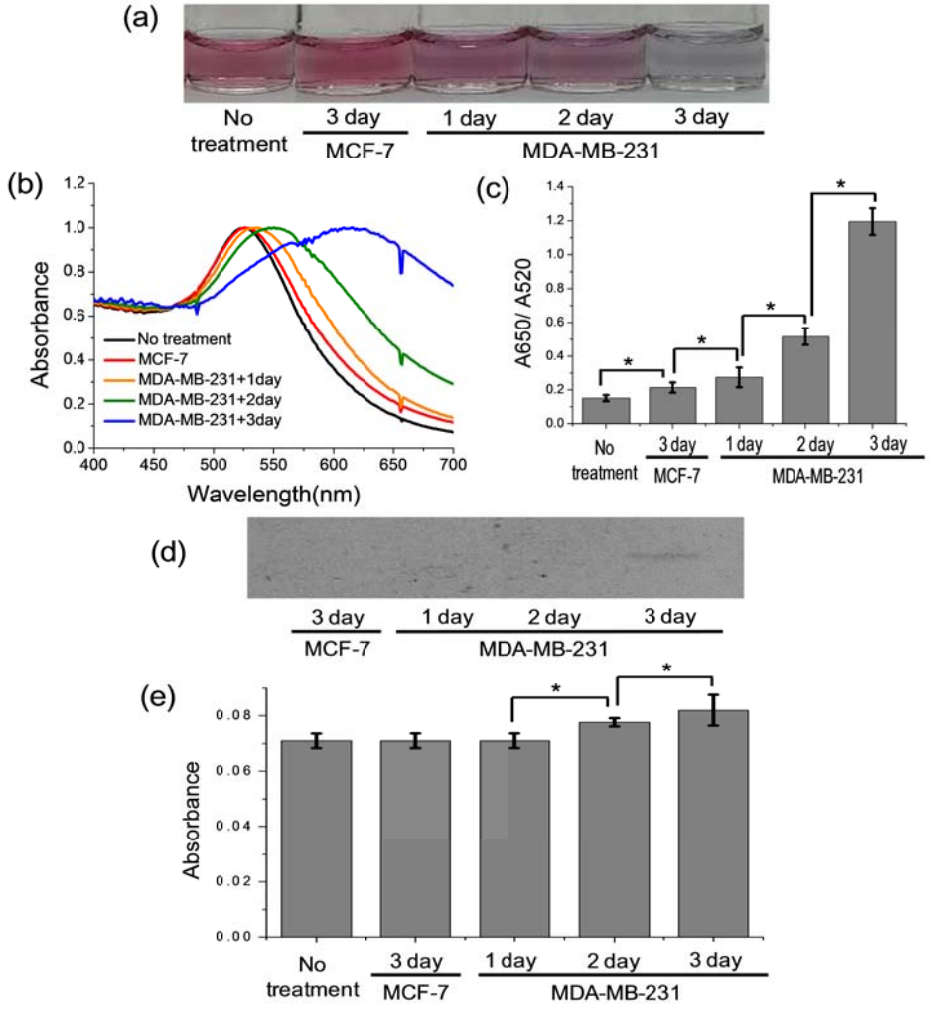

Figure 4.7. Application of lysyl oxidase (LOX)-gold nanoparticles (AuNPs) to cancer cells with different LOX contents. (a) Optical micrographs of LOX-AuNP solution before or after the addition of the conditioned media after a 3-day culture of MCF-7 cells, 1-day, 2-day, and 3-day cultures of MDA-MB-231 cells. (b) Corresponding UV/Vis absorption spectra of (a). (c) Absorbance value of A650/A520 in the conditioned media in (a). (d) Western blot analysis for LOX proteins in the conditioned media in (a). (e) LOX detection in the conditioned media in (a) using a commercially available LOX assay, the Amplite™ Fluorimetric Lysyl Oxidase Assay. Asterisks indicate $p < 0.05$.

4.3.6. Analysis of extracellular matrix remodeling in tumors

IHC against LOX antibody showed strong LOX expression in MDA-MB-231 tumors and limited LOX expression in MCF-7 tumors. In addition, reduced LOX expression was present in MDA-MB-231 tumors treated with LOX inhibitor. Next, the amount of collagen tumor tissue was evaluated using Masson's Trichrome staining. Collagen in fibrils was stained to be blue with Masson's Trichrome. Phosphomolybdic acid, which is highly acid, binds to collagen in Masson's Trichrome staining, which appears blue. Higher amounts of fibrillar collagens present within the MDA-MB-231 tumors appeared blue compared to MCF-7 tumors. In addition, MDA-MB-231 tumors treated with LOX inhibitor somewhat lost their collagen-containing fibrils. Compression testing revealed an incremental stiffening of the MBA-MB-231 tumors compared to MCF-7 tumors (Figure 4.8 d). The elastic modulus of MCF-7 tumors (52 ± 12 kPa) was found to decrease by 89% compared with MBA-MB-231 tumors (457 ± 171 kPa). LOX-inhibitor-treated MBA-MB-231 tumors (402 ± 121 kPa) have a slightly lower value than MBA-MB-231 tumors without LOX-inhibitor treatment.

4.4. Discussion

A significant amount of experimental evidence provides support for the notion that changes in LOX levels alter ECM mechanics and then contribute to cancer

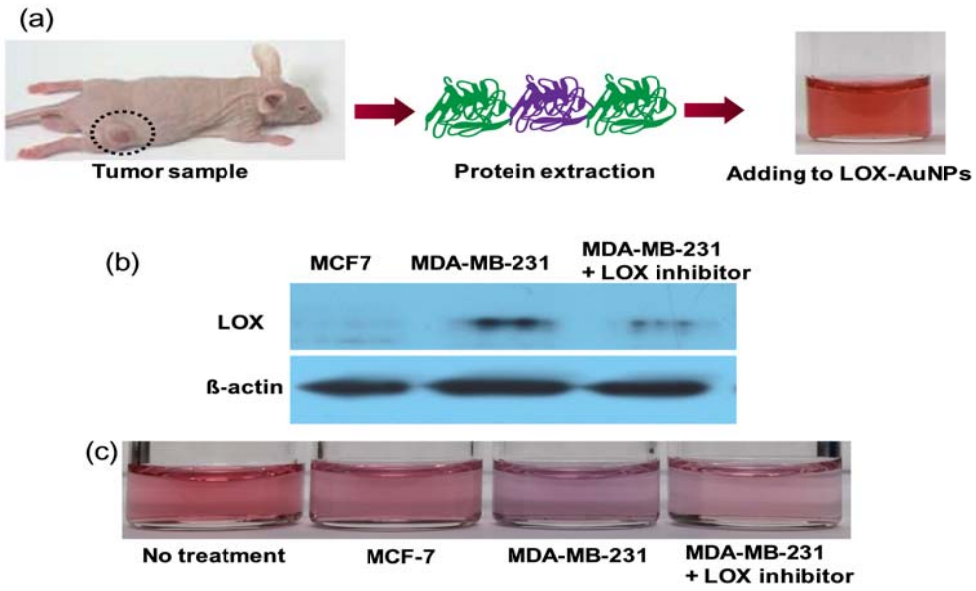

Figure 4.8. Application of lysyl oxidase (LOX)-gold nanoparticles (AuNPs) to tumor tissues with different LOX contents. (a) Scheme of application of LOX-AuNPs to tumor tissues. (b) Western blot analysis for LOX proteins in MCF-7 tumors, MDA-MB-231 tumors, and MDA-MB-231 tumors treated with LOX inhibitor. (c) Optical micrographs of LOX-AuNPs after the addition of the protein extracted from MCF-7 tumors, MDA-MB-231 tumors, and MDA-MB-231 tumors treated with LOX inhibitor. (continued)

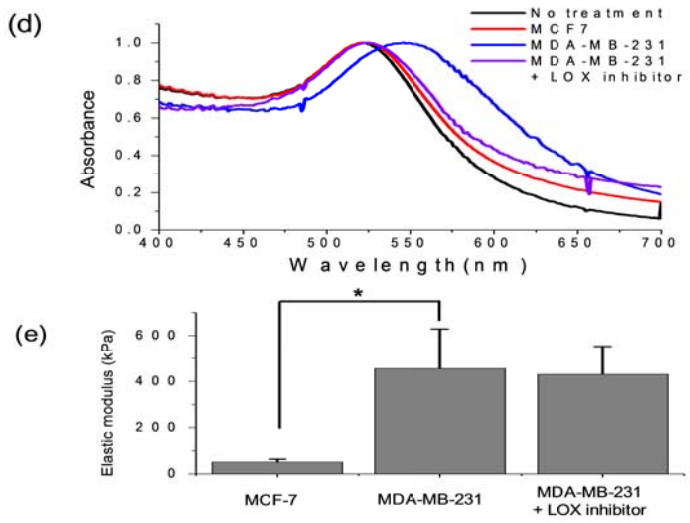

Figure 4.8. Application of lysyl oxidase (LOX)-gold nanoparticles (AuNPs) to tumor tissues with different LOX contents. (d) Corresponding UV/Vis absorption spectra of (c). (e) Compressive modulus of MCF-7 tumors, MDA-MB-231 tumors, and MDA-MB-231 tumors treated with LOX inhibitor. Asterisk indicates $p < 0.05$.

progression: a number of studies have demonstrated that LOX activity is closely correlated with tumors' stiffness and invasiveness of cancer.[1, 11, 23] In this study, AuNPs functionalized with LOX-sensitive peptides were applied to detect presence or amount of LOX in *in vitro*, cancer cell, and tumor tissue levels.

It was assumed that the peptides that have been reactive by LOX on AuNPs can bind to adjacent molecules, which can result in the aggregation of AuNPs via bridging of neighboring AuNPs. The spectral shift and color change of AuNPs is well known to occur due to the change of the aggregate size and interparticle spacing.[24, 25] In this study, the absorption spectra red-shifted and broadened with increasing LOX. Also, an obvious color change was observed from red to purple. Further supporting evidence of the aggregation of LOX-AuNPs was gathered by TEM imaging. TEM images displayed that the well-dispersed LOX-AuNPs before addition of LOX, assembled into AuNP aggregates after addition of LOX. These results in the LOX-AuNP solution together indicate that LOX induces the aggregation and following spectral shift and color change of AuNP.

The presence or amount of LOX can be directly observed by the color variation of the AuNP solution with the "naked eye" or quantified with absorption spectral measurements in the LOX-AuNP assay. Analyzing method using LOX-AuNPs in this study showed detection limit in the nanomolar range of LOX concentration. A commercially available LOX assay indirectly detects the production of hydrogen peroxide released from reaction between LOX substrate and LOX. However, hydrogen peroxide can be generated by multiple enzymes and in multiple cellular

compartments besides LOX reactions in cancer tissue.[26, 27] Indeed, aberrant generation of hydrogen peroxide is known to be correlated with the development and progression of cancer.[26, 28] Based on these results, the LOX-AuNP method is sensitive, rapid, simple, and has potential for use in colorimetric sensors.[29]

Active LOX has been known to increase collagen cross-linking and subsequent ECM stiffness. Indeed, the levels of LOX measured using LOX-AuNPs in various tumor tissues correlated directly with their collagen contents measured with Masson's Trichrome staining and ECM stiffness measured with tensile loading assay. The elastic modulus of MDA-MB-231 tumors was significantly higher than that of MCF-7 tumors and was slightly higher than that of MDA-MB-231 tumors treated with LOX inhibitor. This is consistent with the previous findings.[1, 22] LOX inhibitor β-aminopropionitrile hinders collagen cross-linking and lowers ECM stiffness *in vivo*. In addition, ECM stiffness is known to be closely related with cancer progression and metastasis. Measured stiffness in this study is correlated with previously reported invasive properties of cancer; MDA-MB-231 cells are known as a highly invasive/metastatic breast cancer cell line, while MCF-7 cells are part of a poorly invasive/nonmetastatic breast cancer cell line.[30, 31]

4.5. Conclusions

LOX, an ECM-remodeling enzyme, is known to strongly affect ECM stiffness via

the cross-linking of collagen. AuNPs functionalized with LOX-sensitive hexapeptides were applied to detect LOX as a colorimetric sensor in *in vitro*, cancer cell, and tumor tissue levels. Importantly, when LOX-AuNP was applied to various tumor tissues, the levels of LOX measured using LOX-AuNPs in various tumor tissues correlated directly with their collagen content measured with Masson's Trichrome staining and ECM stiffness measured with tensile loading assay. LOX-AuNPs may be useful for detecting LOX activity and further ECM stiffness of tumor tissues.

4.6. References

1. Levental, K. R.; Yu, H.; Kass, L.; Lakins, J. N.; Egeblad, M.; Erler, J. T.; Fong, S. F. T.; Csiszar, K.; Giaccia, A.; Weninger, W.; Yamauchi, M.; Gasser, D. L.; Weaver, V. M. *Cell* **2009**, *139*, 891.

2. Butcher, D. T.; Alliston, T.; Weaver, V. M. *Nature Reviews Cancer* **2009**, *9*, 108.

3. Sinkus, R.; Lorenzen, J.; Schrader, D.; Lorenzen, M.; Dargatz, M.; Holz, D. *Physics in Medicine and Biology* **2000**, *45*, 1649.

4. Ng, M. R.; Brugge, J. S. *Cancer Cell* **2009**, *16*, 455.

5. Coral, K.; Angayarkanni, N.; Madhavan, J.; Bharathselvi, M.; Ramakrishnan, S.; Nandi, K.; Rishi, P.; Kasinathan, N.; Krishnakumar, S. *Investigative Ophthalmology & Visual Science* **2008**, *49*, 4746.

6. Vater, C. A.; Harris, E. D. Jr.; Siegel, R. C. *Biochemical Journal* **1979**, *181*, 639.

7. Osawa, T.; Ohga, N.; Akiyama, K.; Hida, Y.; Kitayama, K.; Kawamoto, T.; Yamamoto, K.; Maishi, N.; Kondoh, M.; Onodera, Y.; Fujie, M.; Shinohara, N.; Nonomura, K.; Shindoh, M.; Hida, K. *British Journal of Cancer* **2013**, *109*, 2237.

8. Barry-Hamilton, V.; Spangler, R.; Marshall, D.; McCauley, S.; Rodriguez, H. M.; Oyasu, M.; Mikels, A.; Vaysberg, M.; Ghermazien, H.; Wai, C.; Garcia, C. A.; Velayo, A. C.; Jorgensen, B.; Biermann, D.; Tsai, D.; Green, J.; Zaffryar-Eilot, S.; Holzer, A.; Ogg, S.; Thai, D.; Neufeld, G.; Van Vlasselaer, P.; Smith, V. *Nature Medicine* **2010**, *16*, 1009.

9. Kanapathipillai, M.; Mammoto, A.; Mammoto, T.; Kang, J. H.; Jiang, E.; Ghosh, K.; Korin, N.; Gibbs, A.; Mannix, R.; Ingber, D. E. *Nano Letters* **2012**, *12*, 3213.

10. Sounni, N. E.; Noel, A. *Clinical Chemistry* **2013**, *59*, 85.

11. Barker, H. E.; Cox, T. R.; Erler, J. T. *Nature Reviews Cancer* **2012**, *12*, 540.

12. Baker, A.-M.; Cox, T. R.; Bird, D.; Lang, G.; Murray, G. I.; Sun, X.-F.; Southall, S. M.; Wilson, J. R.; Erler, J. T. *Journal of the National Cancer Institute* **2011**, *103*, 407.

13. Zhou, G.; Liu, Y.; Luo, M.; Xu, Q.; Ji, X.; He, Z. *ACS Applied Materials & Interfaces* **2012**, *4*, 5010.

14. Guarise, C.; Pasquato, L.; De Filippis, V.; Scrimin, P. *Proceedings of the National Academy Sciences United States of America* **2006**, *103*, 3978.

15. Tiwari, N.; Rathore, A.; Prabhune, A.; Kulkarni, S. *Advances in Bioscience and Biotechnology* **2010**, *1*, 322.

16. Choi, J. H.; Kim, H. S.; Choi, J.-W.; Hong, J. W.; Kim, Y.-K.; Oh, B.-K. *Biosensors and Bioelectronics* **2013**, *49*, 415.

17. Ojea-Jiménez, I.; López, X.; Arbiol, J.; Puntes, V. *ACS Nano* **2012**, *6*, 2253.

18. Kagan, H. M.; Williams, M. A.; Williamson, P. R.; Anderson, J. M. *Journal of Biological Chemistry* **1984**, *259*, 11203.

19. Gefen, A.; Gefen, N.; Zhu, Q.; Raghupathi, R.; Margulies, S. S. *Journal of Neurotrauma* **2003**, *20*, 1163.

20. Eyre DR, P. M.; Gallop, P. M. *Annual Review of Biochemistry* **1984**, *53*, 717.

21. Kirschmann, D. A.; Seftor, E. A.; Fong, S. F. T.; Nieva, D. R. C.; Sullivan, C. M.; Edwards, E. M.; Sommer, P.; Csiszar, K.; Hendrix, M. J. C. *Cancer Research* **2002**, *62*, 4478.

22. Mammoto, A.; Mammoto, T.; Kanapathipillai, M.; Wing Yung, C.; Jiang, E.; Jiang, A.; Lofgren, K.; Gee, E. P. S.; Ingber, D. E. *Nature Communication* **2013**, *4*, 1759.

23. Erler, J. T.; Bennewith, K. L.; Nicolau, M.; Dornhofer, N.; Kong, C.; Le, Q.-T.; Chi, J.-T. A.; Jeffrey, S. S.; Giaccia, A. J. *Nature* **2006**, *440*, 1222.

24. Slocik, J. M.; Zabinski, J. S.; Phillips, D. M.; Naik, R. R. *Small* **2008**, *4*, 548.

25. Verma, A.; Srivastava, S.; Rotello, V. M. *Chemistry of Materials* **2005**, *17*, 6317.

26. Van de Bittner, G. C.; Dubikovskaya, E. A.; Bertozzi, C. R.; Chang, C. J. *Proceedings of the National Academy of Sciences* **2010**, *107*, 21316.

27. López-Lázaro, M. *Cancer Letter* **2007**, *252*, 1.

28. Lee, D.; Khaja, S.; Velasquez-Castano, J. C.; Dasari, M.; Sun, C.; Petros, J.; Taylor, W. R.; Murthy, N. *Nature Material* **2007**, *6*, 765.

29. Kumar, S.; Rhim, W.-K.; Lim, D.-K.; Nam, J.-M. *ACS Nano* **2013**, *7*, 2221.

30. Charafe-Jauffret, E.; Ginestier, C.; Monville, F.; Finetti, P.; Adelaide, J.; Cervera, N.; Fekairi, S.; Xerri, L.; Jacquemier, J.; Birnbaum, D.; Bertucci, F. *Oncogene* **2005**, *25*, 2273.

31. Uchino, M.; Kojima, H.; Wada, K.; Imada, M.; Onoda, F.; Satofuka, H.; Utsugi, T.; Murakami, Y. *BMC Cancer* **2010**, *10*, 1.

Chapter 5

Tissue-permeable drug-dye conjugates for tumor visualization

5.1. Introduction

Successful surgical procedures for cancer treatment depend on the accurate and rapid localization of tumor tissues, following their correct resection.[1] If the localization of tumors can be displayed in a simple and rapid fashion due to differentiation between tumor and normal tissues, it allows complete tumor resection while preserving important structures like nerves, ureters, and blood vessels.[2] Optical fluorescence imaging is an ideal technology for intra-operative procedures because it offers highly attractive properties, including high sensitivity, real-time image acquisition, portability, low cost, and the absence of ionizing radiation.[3] Fluorescently labeled probes that can expose the difference between tumor and normal tissues can be a favorable approach for the intra-operative detection of cancer.

There are several structural differences between tumor and normal tissues (Figure 5.1).[4] A prominent characteristic of tumor tissues is increased microvessel density, especially in peripheral tumor regions and deficiencies in blood and lymphatic vessel function. Dense vascularization is known to be present in a tumor's periphery. Blood vessels in tumor tissues are known to be leaky and irregularly dilated, unlike normal blood vessels. Moreover, lymphatic vessels in tumors are lacking, which results in the inefficient drainage of interstitial fluid and proteins from the tumor tissue. Another characteristic of tumor tissue is the modified composition and density of the extracellular matrix (ECM). The ECM is composed of a loose

connective network of collagen, elastin, laminin, and fibronectin in normal tissues. Meanwhile, the ECM in tumor tissues include a much denser and thicker network consisting of different compositions compared to normal tissues. These differences between tumor and normal tissues can contribute to the selective detection of tumors.

The extent of drug distribution throughout the body may be represented by the volume of distribution (Vd), the proportionality factor that relates the total amount of a drug in the body to its concentration in the blood at a steady state.[5] A higher Vd indicates that a larger amount of the drug has been distributed in the tissue, suggesting it could be highly permeable to the tissue.[6] In the present study, it was hypothesized that 1) drugs with high Vd can penetrate more deeply into the tissue compared to drugs with a low Vd, and 2) they can differently accumulated in tumor or normal tissues due to the structural differences between them. To verify this hypothesis, four drugs with different Vd values were selected: raloxifene, scopolamine, ampicillin, and ibuprofen (Table 5.1).[7-9] The near-infrared dye, FCR675 was conjugated to the drugs to visualize localization of the drugs *in vivo* and *ex vivo* in this study. Four drug-dye conjugates were synthesized, topically applied via spraying onto an HCT116-luc tumor, and transanally applied via the anus into descending colon of colon tumor-bearing mice (Figure 5.2). The topical application via spraying of the probe can be achieved with reduced doses in a simple and rapid fashion compared to systemic application.[1] The localization of the drug-dye conjugates was analyzed through *in vivo* and *ex vivo* fluorescence imaging.

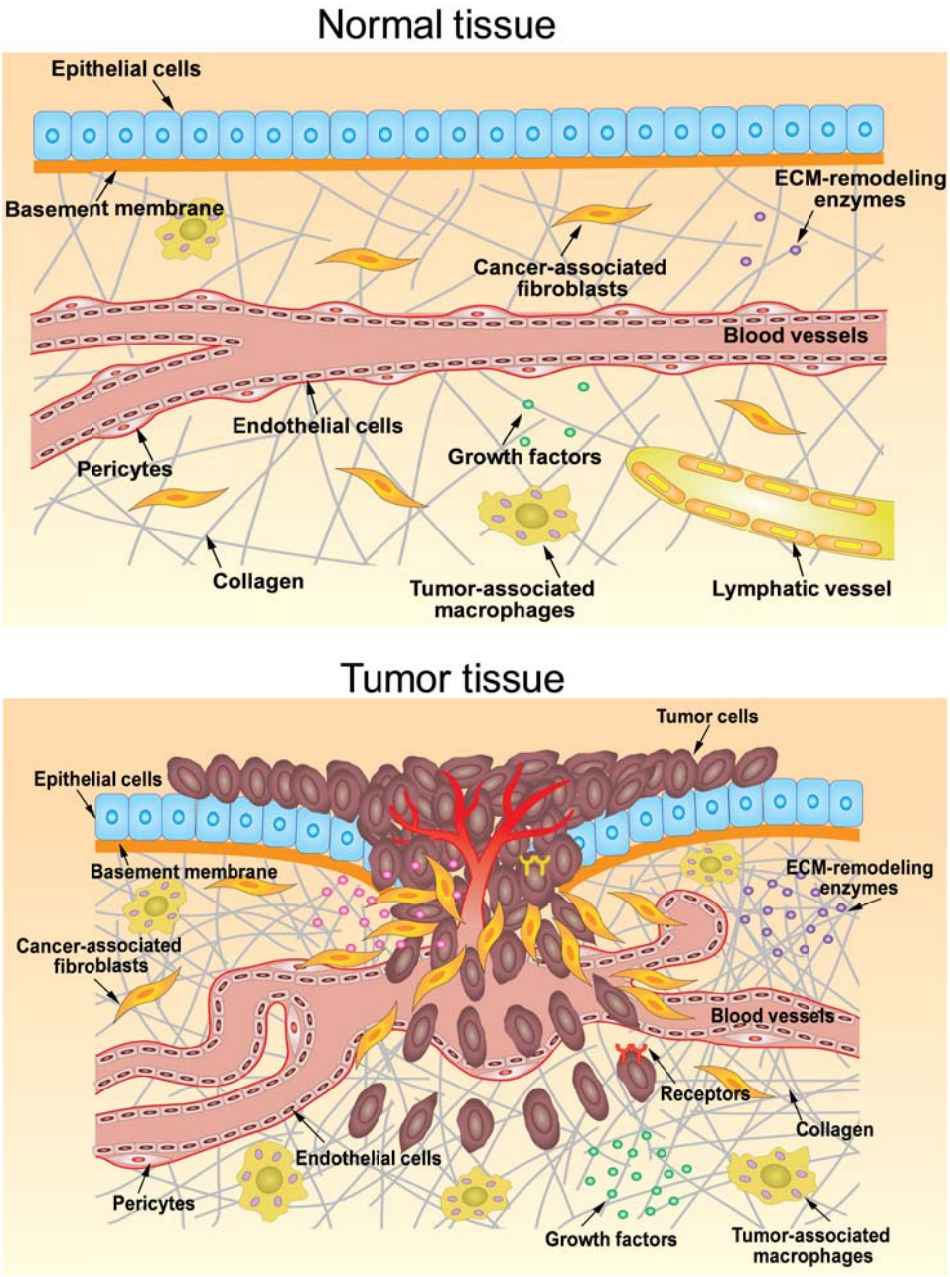

Figure 5.1. Schematic illustration of the major components in normal tissue and tumor tissue.

Table 5.1. Characteristics of drugs used in this study

	Raloxifene	Scopolamine	Ampicillin	Ibuprofen
Molecular Weight	473.58	303.35	371.39	206.29
Mechanism of action	Estrogen receptor modulator	Muscarinic antagonist	Transpeptidase inhibitor	Cyclooxygenase inhibitor
Volume of distribution	2348 L/kg	3.1 L/kg	0.38 L/kg	0.1 L/kg
LogP	5.4	0.89	0.46	3.8

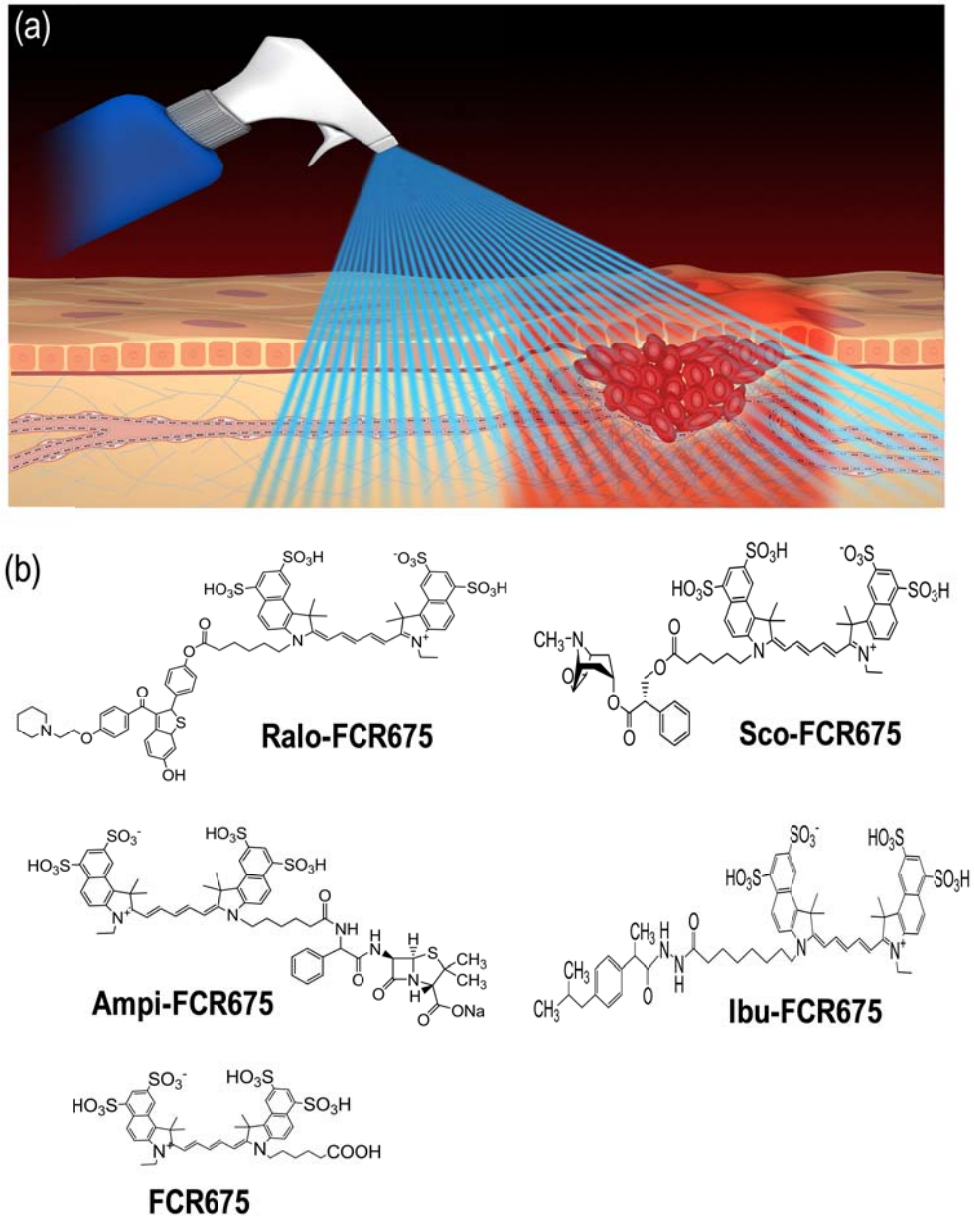

Figure 5.2. (a) Schematic illustration of tumor detection by spraying drug-dye conjugates. (b) Chemical structures of four drug-dye conjugates (Ralo-FCR675, Sco-FCR675, Ampi-FCR675 and Ibu-FCR675) and free dye (FCR675).

5.2. Experimental section

5.2.1. Materials

FCR675 (excitation/emission; 674/699 nm) was purchased from Bioacts (Incheon, Korea). Raloxifene hydrochloride, scopolamine hydrochloride, ampicillin sodium, and ibuprofen were purchased from Sigma-Aldrich (St. Louis, MO). CD31 and von Willebrand Factor (vWF) antibodies were purchased from Santa Cruz Biotechnology Inc. (Santa Cruz, CA), and horseradish peroxidase-conjugated anti-mouse antibody was purchased from Waters (Milford, MA). DMEM and RPMI 1640 were purchased from Gibco (Grand Island, NY).

5.2.2. Synthesis of drug-dye conjugates

To develop the Ralo-FCR675 and Sco-FCR675 conjugates, raloxifene hydrochloride (1.0 mmol), and scopolamine hydrochloride (1.0 mmol) were incubated in a 1:9 (v/v; 0.5 ml) triethylamine (TEA)/dimethylformamide (DMF) for 20 min for desalting, respectively. The FCR675 carboxylic acid (2.0 mmol) was mixed with diisopropylcarbodiimide (DIC; 1.0 mmol) and N,N'-dimethylaminopyridine (DIPEA; 4.0 mmol) in DMF (0.5 ml), and the reaction mixture was then stirred at room temperature (RT) for at least 10 min. Desalted raloxifene and scopolamine in TEA/DMF were added to the FCR675 mixture, and stirred at RT for 6 h. To develop the Ampi-FCR675 conjugate, ampicillin sodium

(1.2 mmol) was mixed with FCR675 N-hydroxysuccinamide (NHS) ester (1.0 mmol) in DMF (0.5 ml). To synthesize the Ibu-FCR675 conjugate, ibuprofen (1.0 mmol) was mixed with DIPEA (2.0 mmol) and 1-[bis(dimethylamino)methylene]-1H-1,2,3-triazolo[4,5-b]pyridinium 3-oxide hexafluorophosphate (HATU; 1.2 mmol) that had been dissolving in DMF for 15 min. Then, the activated ibuprofen was mixed with the FCR675 amine that had been dissolved in DMF in the dark and shaken overnight. The product was purified by semi-preparative reverse phase-high performance liquid chromatography (RP-HPLC) using 5% to 95% acetonitrile containing 0.1% trifluoroacetic acid (TFA) versus distilled water (DW) containing TFA over 25 min at a flow rate of 5 ml/min. The appropriate fractions were collected and lyophilized.

5.2.3. Characterization of drug-dye conjugates

Four drug-dye conjugates were characterized by analytical RP-HPLC using 30% to 90% acetonitrile containing 0.1% TFA versus DW containing TFA over 20 min at a flow rate of 1 ml/min. Matrix-assisted laser desorption/ionization-time of flight (MALDI-TOF) mass spectrometry was utilized to quantify the molecular weight of four drug-dye conjugates using a MALDI-TOF system (Microflex LRF20, Bruker Daltonics, Bremen, Germany). The partition coefficients (logP) of drug-dye conjugates were determined using the RP-HPLC method.[10] The calibration curve was drawn using the retention time and logP of the standard substances, including

ethyl acetate, nitrobenzene, toluene, 1,2-dichlorobenzene, and phenanthrene (Figure 5.2). In this calibration curve, logk' means $\log[(T_R-T_0)/T_0]$, and T_R and T_0 indicate retention time of sample and non-retained substance, respectively. The retention time of the drug-dye conjugates was converted to a logP scale through a calibration curve.

5.2.4. Cytotoxicity and cellular uptake

The cytotoxicity of drug-dye conjugates was evaluated with a 3-(4,5-dimethylthiazol-2-yl)-2,5-diphenyl tetrazolium bromide (MTT) assay. Fire fly luciferase (luc) gene-transfected human colorectal carcinoma cells (HCT116-luc) were maintained in an RPMI 1640 medium containing 10% (v/v) fetal bovine serum and penicillin G (100 U/ml)/streptomycin (100 μg/ml) at 37°C, 5% CO_2. HCT116-luc cells (1×10^4 cells/well) were seeded in a 96-well plate and maintained for 12 h. The various concentrations of the four drug-dye conjugates and the free dye (0.1, 1.0, 5.0, 10, 25, 50 μM) were added to each well of the cell and then incubated for 24 h. The MTT solution was added and incubated for 2 h, and absorbance was observed at 570 nm with a plate reader. Cell viability was calculated as the percentage of viable cells relative to untreated cells. The experiment was performed in triplicate.

To investigate the cellular uptake of Ralo-FCR675, HCT116-luc cells were plated

in 35-mm covered glass-bottomed dishes and incubated for 48 h. Various concentrations of Ralo-FCR675 (0, 1.25, 2.5, 5.0 M) were treated in each cell culture and incubated for 2 h. The cells were stained with 4',6-diamidino-2-phenylindole (DAPI). The samples were observed using a confocal laser scanning microscope (Leica SP5, Leica Microsystems, Buffalo, Grove, IL).

5.2.5. Liver tumor model

All animal experimental procedures were in compliance with the institutional guidelines of Korea Institute of Science and Technology and the relevant laws. A tumor was induced in male athymic BAL/c nude mice (20 g, Orient, Korea), and the mice were anesthetized with an intraperitoneal injection of xylazine (10 mg/kg body weight) and ketamine (80 mg/kg body weight). A paramidline abdominal incision was made to expose the liver. Then, HCT116-luc cells (3×10^5 cells/mouse) suspended in 20 μl of sterile saline were injected into the left lobe of each mouse's liver under the capsule. After the injection of tumor cells, the paramidline incision was sutured with 4-0 black silk.

5.2.6. Topical application via spraying of drug-dye conjugates

Fourteen days after the injection of the HCT116-luc cells into the liver, the liver

was once again exposed via a paramidline abdominal incision. Four drug-dye conjugates and the free dye (FCR675) were topically applied by spraying the surface of the HCT116-luc tumor in the liver. Before application, the fluorescence intensities of the four drug-dye conjugates and the free dye were adjusted using a Kodak image station (4000MM; Kodak, New Haven, CT) equipped with a cooled charged-coupled device video camera (CCD camera; Kodak, Japan), a special C-mount lens, and a Cy5.5 bandpass emission filter (680-720 nm). After incubating for 3 min, the tissue was washed three times with phosphate-buffered saline (PBS).

5.2.7. *In vivo* and *ex vivo* fluorescence imaging

To quantify the drugs' circulation time in the blood, Ralo-FCR675, Sco-FCR675, Ampi-FCR675, and Ibu-FCR675 were intravenously injected into the tail vein. One milliliter of blood samples (n=3) were drawn from the mice at pre-determined time points and were centrifuged at 4000 rpm for 10 min at 4°C. A Kodak image station captured NIR fluorescence images of the supernatant fractions.

After topical application via spraying for 3 min and subsequent washing, an IVIS Spectrum imaging system (Caliper Life Sciences, Hopkinton, MA) captured NIR fluorescence and bioluminescence images *in vivo*. For bioluminescence imaging, a D-luciferin solution (150 mg/kg body weight) was intraperitoneally injected 10 min prior to imaging. The total photon counts from pre-defined regions of interest (ROI)

in each animal were calculated using Living Image software (Caliper Life Sciences). After the *in vivo* NIR fluorescence imaging, the mouse was sacrificed, and the liver was excised and imaged using the IVIS Spectrum imaging system.

Ex vivo NIR fluorescence of excised liver tumor was captured with a small animal imaging system (OV100, Olympus, Japan). Ralo-FCR675 and FCR675 were topically applied via spraying on the exposed liver through a paramidline abdominal incision in live mice. After 3 min of incubation and washing, the liver was excised and sliced at 400 μm thickness to observe the penetration of the Ralo-FCR675 and FCR675 along the depth of the tumor. Fluorescence images of the liver tumor were taken using OV-100 with 620-650 nm/680-710 nm (Ex/Em) channel.

5.2.8. Azoxymethane-induced colon cancer model

Male A/J mice (6 weeks old, Orient, Korea) were injected intraperitoneally with 10 mg/kg of azoxymethane (AOM) dissolved in PBS once a week for 8 weeks.[11, 12] The mice were anesthetized by inhalation of isoflurane. A midline abdominal incision was made to expose the colon. Ralo-FCR675 (5 μM, 500 μl) was administered via the anus into descending colon with a plastic needle. The anus and transverse colon were immediately clamped with blunt forceps for 3 min. The colon was washed three times by PBS and carefully excised. Excised colons were imaged by an IVIS Spectrum imaging system. The colon lesions exhibited high fluorescence signals were analyzed with hematoxylin and eosin (H&E) staining.

5.2.9. Histological analysis

Each excised liver was divided into two pieces. One piece was embedded into an optimal cutting-temperature (OCT) compound for cryosection preparation and further fluorescence microscopy analysis. The other piece was fixed in a 4% (v/v) buffered formalin and then embedded in paraffin. 8 μm-thick frozen sections cut from the OCT-embedded specimens were stained with DAPI and observed for microscopic imaging of Cy5.5 and DAPI fluorescence. Meanwhile, 4 μm-thick sections cut from the paraffin-embedded tissues were stained with H&E or Masson's trichrome. In addition, the paraffin sections were stained with the primary antibodies against endothelial cell markers, von Willebrand Factor (vWF) and CD31. The staining signal was developed with a Histostain®-Plus Kit. Sections were counterstained with Harris's hematoxylin.

5.3. Results

5.3.1. Characterization of drug-dye conjugates

Four drug-dye conjugates were synthesized by directly coupling FCR675 with raloxifene, scopolamine, ampicillin, and ibuprofen (Figure 5.2 b). FCR675 acid in the presence of DIC and DIPEA was coupled with a hydroxyl group of raloxifene and scopolamine, respectively, to afford Ralo-FCR675 and Sco-FCR675. FCR675 NHS ester was conjugated to an amine group of ampicillin sodium in DMF to

synthesize Ampi-FCR675. Ibuprofen was reacted with the FCR675 amine using HATU and DIPEA as coupling reagents to produce the Ibu-FCR675 conjugate. All drug-dye conjugates were purified using RP-HPLC, rendering > 95% purity of all conjugates (data not shown).

Formation of the drug-dye conjugates was confirmed with mass spectrometry analysis. Each conjugate analyzed by MALDI-TOF displayed a mass in agreement with the calculated values (calculated for Ralo-FCR675: 1370, found: 1371; calculated for Sco-FCR675: 1201, found: 1202; calculated for Ampi-FCR675: 1268, found: 1267; calculated for Ibu-FCR675: 1147, found: 1147) (Figure 5.4, Table 5.2). The partition coefficient (logP) of the drugs used in this study ranges between 0.46 and 5.4. However, the logP of the drug-dye conjugates drawn from the standard curve narrowly ranges between 0.87 and 1.3 after conjugating with FCR675 (Figure 5.3, Table 5.2).

To evaluate the cytotoxicity of the drug-dye conjugates, the viability of HCT116-luc cells was measured using a MTT (Figure 5.5 a). The HCT116-luc cells were treated with various concentrations of the drug-dye conjugates (0.1, 1.0, 5.0, 10, 25, and 50 μM). All drug-dye conjugates and the free dye exhibited cell viability > 95% at all concentrations up to 50 μM. Cellular uptake of Ralo-FCR675 was evaluated in HCT116-luc cells. Increasing fluorescence intensity was observed in the cells with higher concentrations of treated Ralo-FCR657 (Figure 5.5 b). Ralo-FCR675 displayed fluorescence signals in both the cytoplasm and the nuclei.

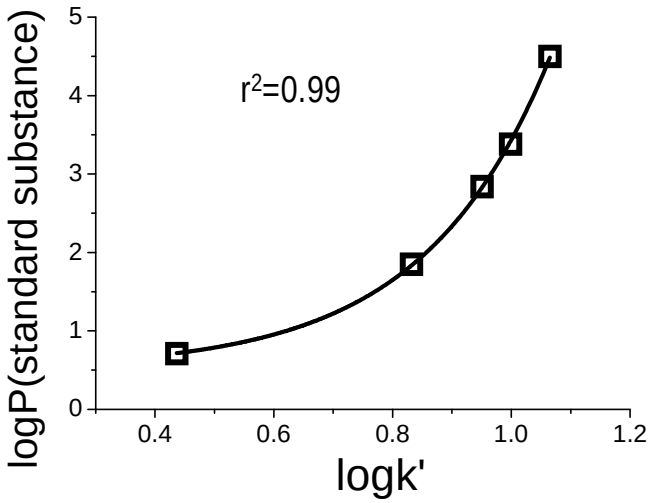

Figure 5.3. Calibration curve drawn using retention time and partition coefficient (logP) of the standard substance including ethyl acetate, nitrobenzene, toluene, 1,2-dichlorobenzene, and phenanthrene to determine logP of drug-dye conjugates.

Table 5.2. Molecular weight and logP of drug-dye conjugates

	Ralo-FCR675	Sco-FCR675	Ampi-FCR675	Ibu-FCR675
Molecular Weight	1371	1202	1267	1147
LogP	1.3	1.0	0.87	1.2

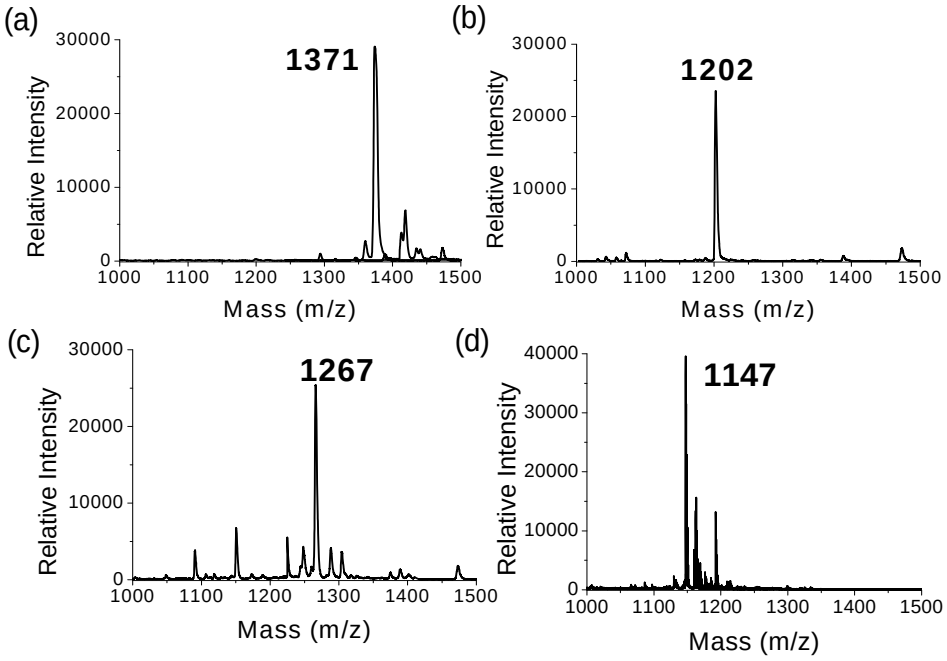

Figure 5.4. Mass spectrometry of (a) Ralo-FCR675, (b) Sco-FCR675, (c) Ampi-FCR675, and (d) Ibu-FCR675.

To measure how fast the drug-dye conjugates extravasate from blood vessels, the blood samples obtained from mice after intravenous administration of the drug-dye conjugates were analyzed. Ralo-FCR675 demonstrated weak fluorescence intensity (fluorescence intensity: 676 ± 44) in the blood even at 15 min after intravenous injection. However, Ibu-FCR675 showed exceptionally strong fluorescence intensity (fluorescence intensity: 2632 ± 245) at 15 min after intravenous injection and considerable fluorescence intensity (fluorescence intensity: 1141 ± 41) in the blood at 360 min after intravenous injection (Figure 5.6). The conjugates remained in the blood, in ascending order, is as follows: Ralo-FCR675, Sco-FCR675, Ampi-FCR675, and Ibu-FCR675. The Vd value of the drug-dye conjugates was not directly measured; however, the circulating time of the drug-dye conjugates in blood can represent the property of Vd, in part.

5.3.2. Preferential accumulation of drug-dye conjugates in tumors

To evaluate the distribution of the drug-dye conjugates in the tumors, 100 μl of 25 μM four drug-dye conjugates and the free dye (FCR675) in PBS were topically applied via spraying on the liver surface of the HCT116 liver tumor-bearing mice. The tumors were induced in the liver using luciferase-transfected HCT116 tumor cells. Drug-dye conjugates were simultaneously sprayed both on the surface of the tumors and in non-tumor regions. After spraying, the livers was preserved for 3 min and then washed for 1 min three times. This protocol was followed in experiments

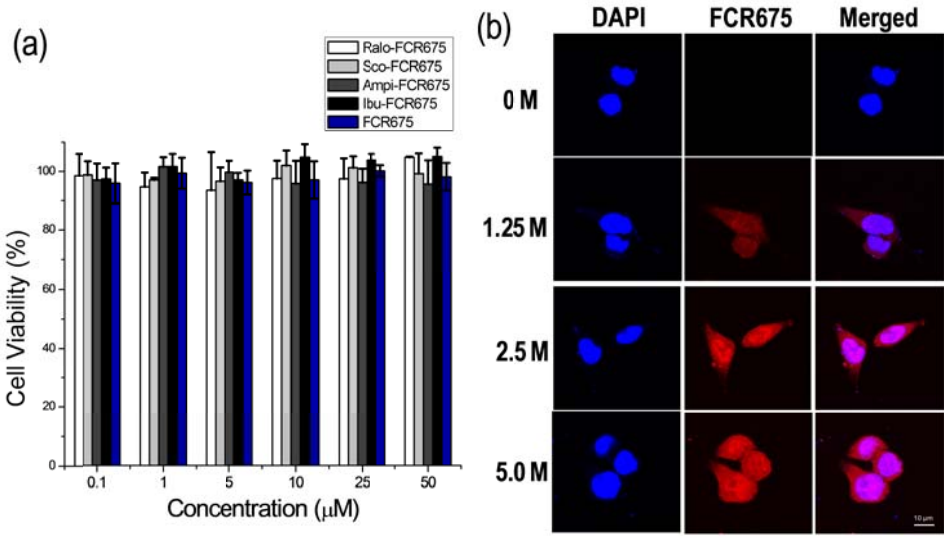

Figure 5.5. Cytotoxicity and cellular uptake of drug-dye conjugates. (a) Cell viability measured with a 3-(4,5-dimethylthiazol-2-yl)-2,5-diphenyl tetrazolium bromide (MTT) assay. HCT116-luc cells were incubated for 12 h with various concentrations of four drug-dye conjugates and FCR675. (b) Cellular uptake of various concentrations of Ralo-FCR675 (red). The nucleus was stained with DAPI (blue). The scale bar indicates 10 μm.

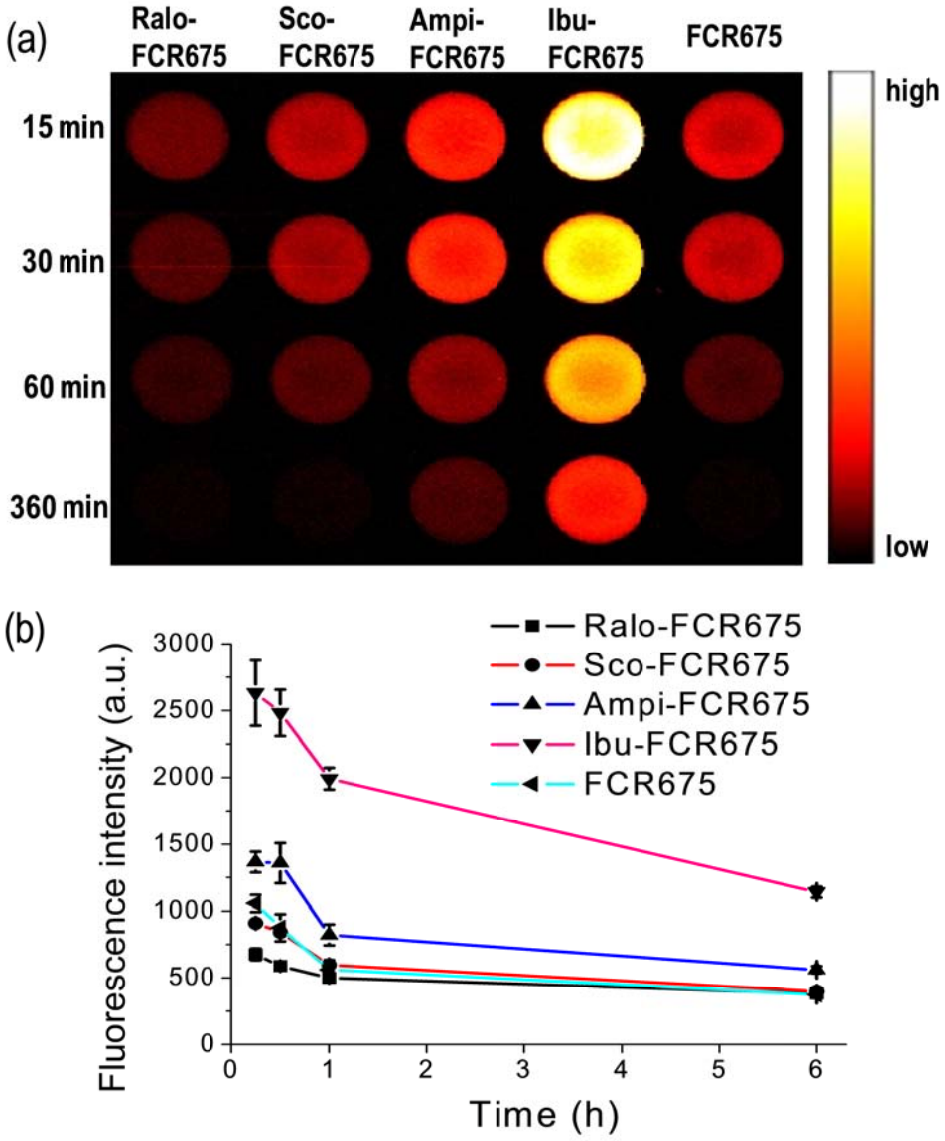

Figure 5.6. Measurement of how fast the drug-dye conjugates and free dye extravasate from blood vessels. (a) Representative fluorescence images and (b) fluorescence intensity graph of blood samples (n=3) obtained from mice intravenously injected with four drug-dye conjugates or free dye.

of this study. The presence and location of tumors in mice were measured with bioluminescence. Ralo-FCR675 exhibited the strongest fluorescence in the images from the IVIS Spectrum imaging system, and the location of this signal was significantly matched with the tumor region (Figure 5.7). Conversely, minimal NIR fluorescence remained on the liver tumor surface when Ibu-FCR675 and FCR675 were applied. Importantly, cross-section images of the livers presented penetration depth of the drug-dye conjugates. Ralo-FCR675 penetrated the tumors to a maximum depth (up to 3 mm below the surface); Sco-FCR675 penetrated to half the tumors' maximum depth (up to 1.5 mm below the surface); and Ampi-FCR675, Ibu-FCR675, and FCR675 rarely penetrated into the tumors (< 0.5 mm below the surface) (Figure 5.7). In addition, selective accumulation and high permeability of Ralo-FCR675 in the tumor tissue was confirmed by the images from the OV100 imaging system (Figure 5.7). On the other hand, FCR675 was rarely present in the tissues.

5.3.3. Analysis of the distribution of drug-dye conjugates

The rapid penetration of Ralo-FCR675 was displayed in tumor sections (Figure 5.8 a). Twenty, 40, and 60 seconds after spraying, the livers were immediately excised and frozen. As the incubation time became longer, increasing penetration of Ralo-FCR675 was observed in the tumor tissue. Within 60 s, Ralo-FCR675 displayed considerable penetration. The selective accumulation of the drug-dye

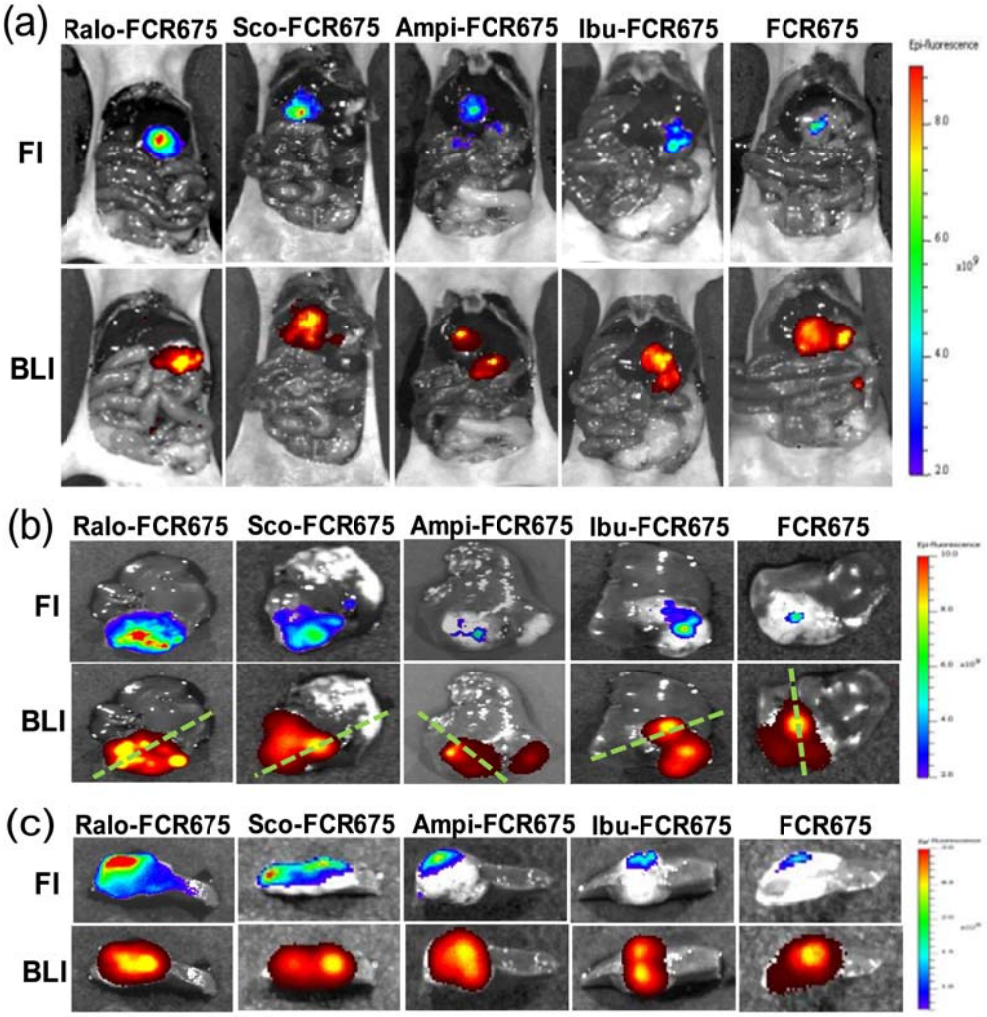

Figure 5.7. *In vivo* and e*x vivo* imaging in HCT116-luc liver tumor-bearing mice. (a) *In vivo* NIR fluorescence imaging (FI) and bioluminescence imaging (BLI) of exposed livers captured with an IVIS Spectrum imaging system after topical application via spraying for 3 min and subsequent washing. (b) *Ex vivo* near infrared (NIR) FI and BLI of excised livers of liver tumor-bearing mice with four drug-dye conjugates and free drug. (c) Cross-sectional NIR FI and BLI of livers in liver tumor-bearing mice with four drug-dye conjugates and free drug. The livers were cut along the green dotted lines in (b). (continued)

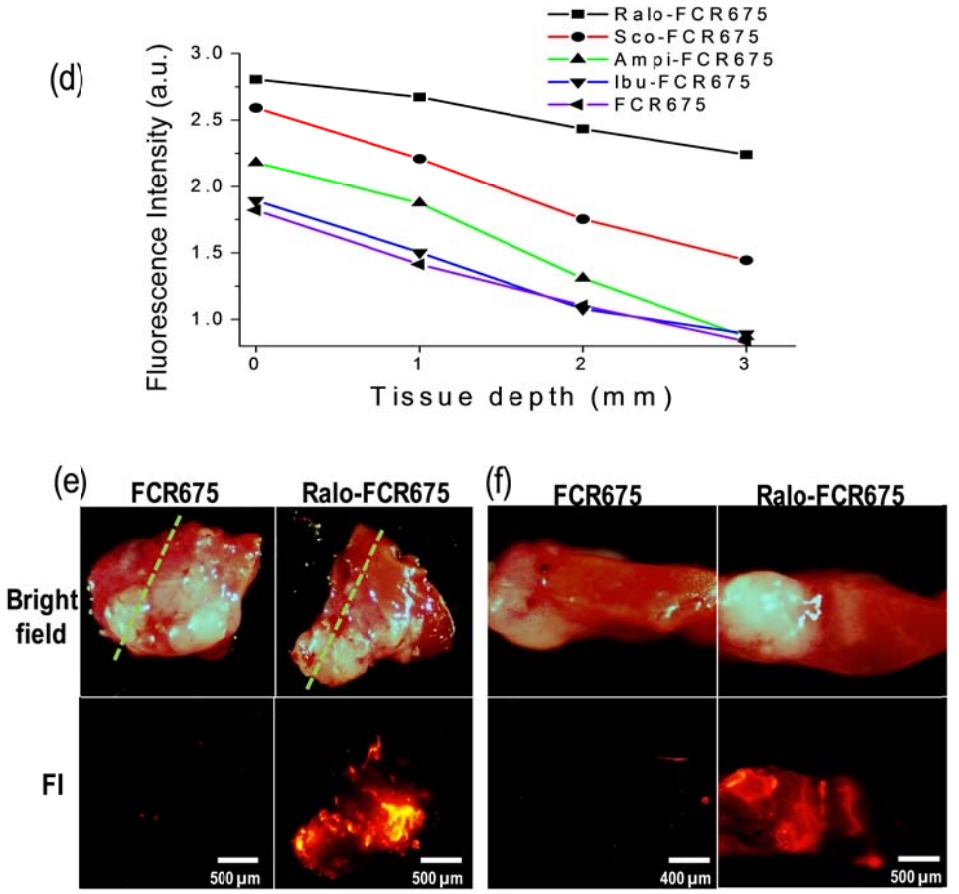

Figure 5.7. *In vivo* and *ex vivo* imaging in HCT116-luc liver tumor-bearing mice. (d) NIR fluorescence signal intensities according to tumor depth in cross-section images. (e) *Ex vivo* NIR FI of excised livers captured by OV-100 imaging system after topical application via spraying of Ralo-FCR675 and FCR675. (f) Cross-sectional NIR FI of livers in liver tumor-bearing mice with Ralo-FCR675 and FCR675. The livers were cut along the green dotted lines in (e).

conjugates was further confirmed by analyzing fluorescence in tumor and normal sections. Ralo-FCR675 was confirmed to penetrate most deeply into the tumor tissue among the drug-dye conjugates studied (Figure 5.8 b). When Sco-FCR675 and Ampi-FCR675 were topically applied, their fluorescence intensity was strong near the tumor surface and then drastically diminished on the way to the tumor core. When Ibu-FCR675 and FCR675 were sprayed on the tumors, minimal fluorescence intensity was found throughout the tumor tissue. Unlike the preferential accumulation in tumor regions, minimal fluorescence intensity was found throughout the normal tissue when all drug-dye conjugates were topically applied. These data indicated that the drug-dye conjugate preferentially accumulated in tumor tissue.

H&E analysis confirmed the presence of the HCT116 tumors in all excised livers (Figure 5.9 a). Substantially deposited collagens in the basement membrane appeared blue in the tumor tissue through Masson's trichrome staining (Figure 5.9 b). Fibrillar collagens present within the tumor mass appeared blue, whereas the sections from normal livers appeared red in the basement membrane without signs of collagen deposition (Figure 5.9 c). Anti-vWF and anti-CD31 immunostaining revealed that denser blood vessels existed in the tumor periphery compared to normal tissues (Figure 5.9).

5.3.4. Transanal application to colon cancer model

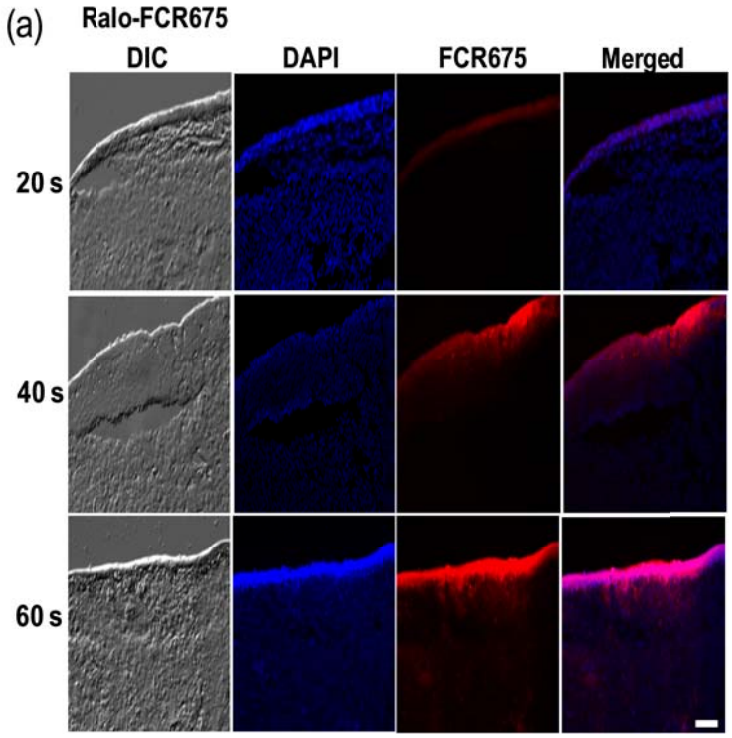

Figure 5.8. Accumulation of the drug-dye conjugates analyzed in tumor sections. (a) Fluorescence signals in liver tumor sections of mice 20, 40 and 60 s after the topical application of Ralo-FCR675 (red) via spraying. The nucleus was stained with DAPI (blue). The scale bars indicate 50 μm. (continued)

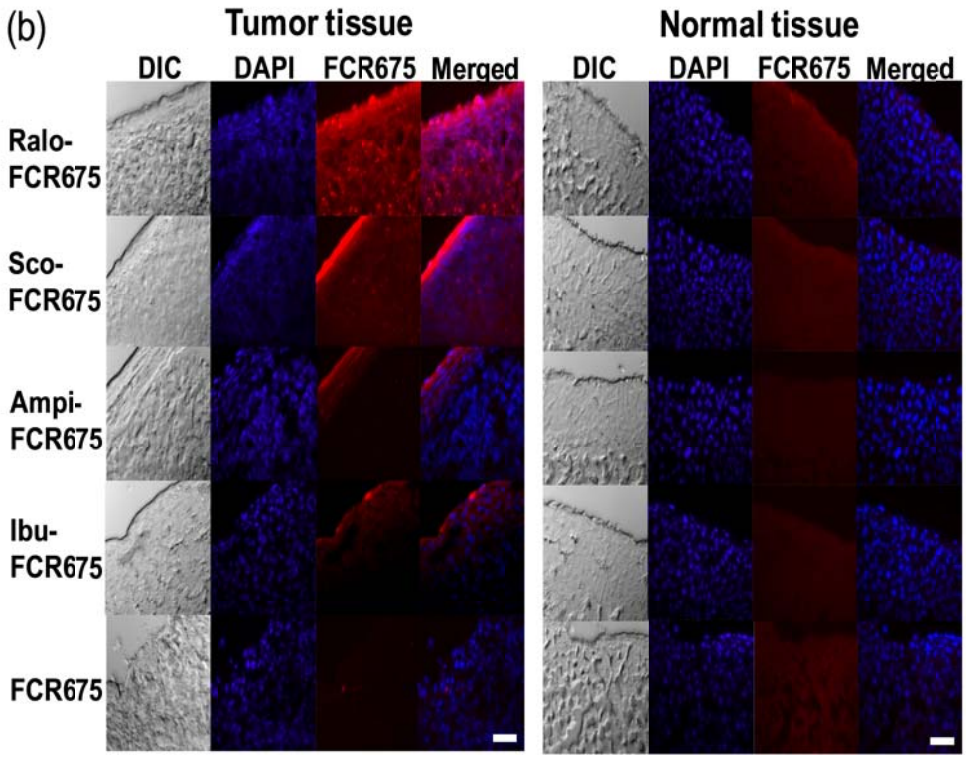

Figure 5.8. Accumulation of the drug-dye conjugates analyzed in tissue sections. (b) Fluorescence signals detected in liver tumor and normal liver sections of mice after the topical application of four drug-dye conjugates and free dye (red) for 3 min and subsequent washing. The nucleus was stained with DAPI (blue). Scale bars indicate 50 μm.

Colon tumors developed in the descending colon of mice treated with AOM, as described previously.[12] The Ralo-FCR675 (5 μM/500 μl PBS/mouse) was applied via the anus into the descending colon of colon tumor-bearing mice and maintained inside the descending colon for 3 min by clamping between the anus and transverse colon. Then, the colon tissue was washed three times with PBS, and the tumor-bearing mice were sacrificed. The cancer lesions of the excised colon demonstrated high fluorescence intensity compared with adjacent mucosa in the NIR *ex vivo* image (Figure 5.10 b). Colon lesions demonstrating a high fluorescence signal revealed well-differentiated carcinomas in H&E stain (Figure 5.10 c).

5.4. Discussion

A number of studies have demonstrated various approaches to the intra-operative detection of tumors.[1, 2, 13, 14] In this study, it was investigated whether fluorescently labeled drugs with high Vd selectively accumulated into tumor, not in normal tissue, which enabled visualization of the tumor. Drugs with different Vd values were selected: raloxifene (2348 l/kg), scopolamine (3.1 l/kg), ampicillin (0.38 l/kg), and ibuprofen (0.15 l/kg).[7-9] These drugs were conjugated with NIR dye and then topically applied via spraying on the surface of an HCT116-luc liver tumor and transanally applied via the anus into the descending colon of colon tumor-bearing mice. Ralo-FCR675 can penetrate more deeply into the tissues than other drug-dye conjugates and, more interestingly, the fluorescence of Ralo-FCR675 was

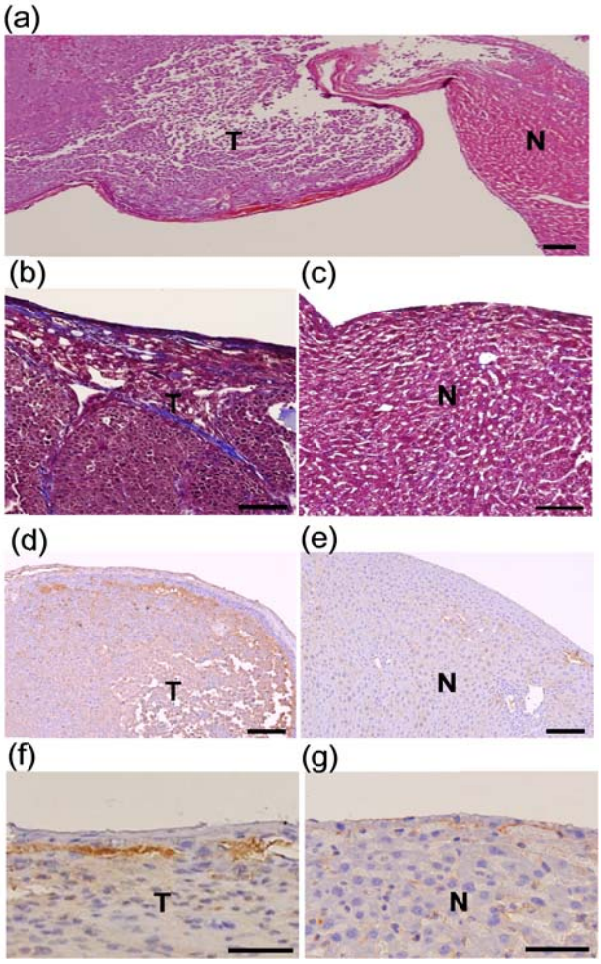

Figure 5.9. Histological and immunohistochemical analyses. (a) Hematoxylin and eosin staining, (b,c) Masson's trichrome staining, (d,e) anti-von Willebrand Factor (vWF) immunostaining, and (f,g) anti-CD31 immunostaining of liver tumor tissues and normal liver tissues. All excised liver was confirmed to contain HCT116 tumor by hematoxylin and eosin staining. In Masson's trichrome staining, collagen fibers appeared blue. Substantially deposited collagens in the basement membranes appeared blue in tumor tissue through Masson's trichrome staining. vWF and CD31 were used as endothelial cell markers. T, liver tumor tissue; N, normal liver tissue. The scale bars indicate 100 μm in (a) and 50 μm in (b-g).

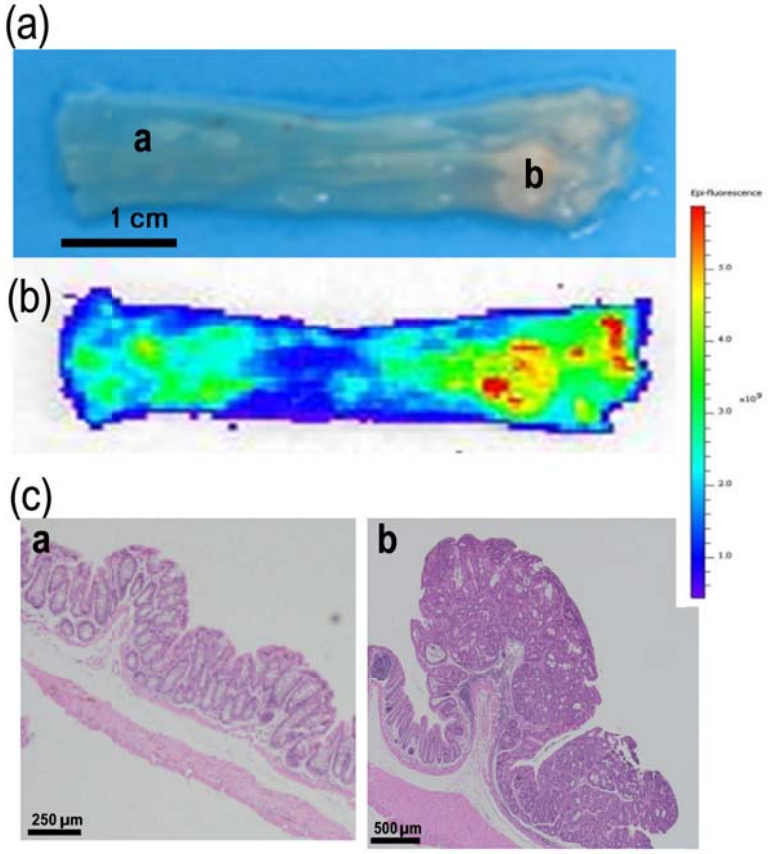

Figure 5.10. Transanal application of Ralo-FCR675 to azoxymethane-induced colon cancer mice. Ralo-FCR675 was administered via the anus into the descending colon with a plastic needle. (a) Photo image and (b) Fluorescence image of excised colon after transanal application of Ralo-FCR675. (c) Hematoxylin and eosin stains in colon tissue sections marked **a** (left image) and **b** (right image) in (a).

preferentially observed in tumor lesions.

The topical application of Ralo-FCR675 caused preferential distribution in tumor tissue, rather than in normal tissue. First, Ralo-FCR675 penetrated more deeply into tumor tissue than other drug-dye conjugates presumably due to its high Vd (Figure 5.7, 5.8). In addition, drug-dye conjugates selectively accumulated in tumor tissues over normal tissues (Figure 5.7, 5.8), which is attributed to a much denser and thicker ECM network in tumor tissues and denser vascularization in peripheral tumor tissues unlike normal tissue (Figure 5.9).

Raloxifene-dye conjugates could aid surgeons as contrast agents for delineating the margins of a tumor mass for tumor resection and appropriate biopsy.[15] It is worth noting that Ralo-FCR675 selectively accumulated in tumors as compared to normal tissues. Drug-dye conjugates were devised as a solution that is amenable to spraying *in vivo*, thus interfacing more readily with intraoperative and endoscopic procedures. Drug-dye conjugates can be topically applied via spraying to surgically exposed lesions at risk, making exposed lesions accessible to fluorescence detection[16]. In addition, the short incubation time (3 min) required for fluorescence detection does not require the surgeon to wait with exposed lesions. The fluorescence lasts sufficiently long (12 h), maintaining > 90% fluorescence intensity (data not shown). This long-lasting fluorescence could enable various interventional procedures, such as tumor resectioning or endoscopic biopsy in clinical settings. To detect the tumor foci at the margins of the tumor mass, FCR675 dye in the NIR fluorescence spectrum (650–900 nm) provides benefits such as relatively low

autofluorescence and high tissue penetration, allowing for highly sensitive imaging in deep tissue.[17, 18]

Combining raloxifene with a therapeutic drug has the potential to selectively improve local delivery to the tumor center, contributing to overcoming drug resistance. Ralo-FCR675 penetrated most deeply into tumor tissue. Limited drug penetration through tumor tissue precludes exposing all the target cancer cells to a lethal concentration of a drug. This has been considered a primary reason for chemotherapy resistance leading to treatment failure.[19, 20] Therefore, using raloxifene as a delivery carrier for a therapeutic drug could enhance drug penetration into the tumor core, thereby overcoming chemotherapy resistance.

Combining raloxifene with an imaging agent or a therapeutic drug could be applied as the mode of local delivery. The local delivery of a therapeutic drug has recently attracted much interest with the development of highly technological medical devices such as endoscope, laparoscopic, or robotic instruments. Local delivery presents many advantages, including reduced dosage and only local exposure, potentially minimizing the risk of systemic side effects.[21] In fact, the local injection of the mitomycin C-dextran conjugate to the tumor sites led to decreased systemic toxicity.[22] Drug-dye conjugates were topically applied to liver tumors in this study, which could be translated to patients' oral cavity for clinical applications.

Known drugs have the advantage of accelerating clinical translation as contrast agents. Modified drugs are certainly considered a new area in regulatory approval

for human use.[23] However, all drugs used in clinical settings come with practitioners' knowledge of the pharmacokinetics, biodistribution, and side effects in humans, thereby reducing translational risk. Most drugs have their Vd values evaluated in animals and in early-phase clinical trials before they can be introduced into a clinical setting. Factors affecting Vd include the solubility and plasma-binding capability of drugs, which result in Vds displaying a wide range of values.[24] The documented Vd values of drugs can be easily screened for additional contrast agent candidates.

5.5. Conclusions

Four drug-dye conjugates were synthesized by coupling the NIR dye FCR675 with four drugs with different Vd values: raloxifene, scopolamine, ampicillin, and ibuprofen. Topically applied Ralo-FCR675 also rapidly penetrated to the tumor's maximum depth and, importantly, it preferentially accumulated in the tumor lesions, which enabled the visualization of the tumor. Fluorescently labeled drugs with high Vd, such as raloxifene, have the potential to rapidly detect tumors, contributing to effective tumor resection.

5.6. References

1. Urano, Y.; Sakabe, M.; Kosaka, N.; Ogawa, M.; Mitsunaga, M.; Asanuma, D.; Kamiya, M.; Young, M. R.; Nagano, T.; Choyke, P. L.; Kobayashi, H. *Science Translational Medicine* **2011**, *3*, 110.

2. Nguyen, Q. T.; Tsien, R. Y. *Nature Reviews Cancer* **2013**, *13*, 653.

3. Weissleder, R.; Pittet, M. J. *Nature* **2008**, *452*, 580.

4. Heldin, C.-H.; Rubin, K.; Pietras, K.; Ostman, A. *Nature Reviews Cancer* **2004**, *4*, 806.

5. Allen L, K. K.; MacKichan J.; Ritschel W. A. *Journal of Clinical Pharmacology* **1982**, *22*, 1.

6. Finkel, R.; Clark, M. A.; Cubeddu, L. X. Lippinocott's Illustrated Reviews: Pharmacology, Fourth Edition **2009,** Lippincott Williams & Wilkins**.**

7. Heringa, M. *International Journal of Clinical Pharmacology and Therapeutics* **2003***, 41*, 331.

8. Obach, R. S.; Lombardo, F.; Waters, N. J. *Drug Metabolism and Disposition* **2008**, *36*, 1385.

9. Sjövall J, A. G.; Huitfeldt B. *British Journal of Clinical Pharmacology.* **1986**, *21*, 171.

10. Griffin, S.; Wyllie, S. G.; Markham, J. *Journal of Chromatography A* **1999** *864*, 221.

11. Lee, S.; Ryu, J. H.; Park, K.; Lee, A.; Lee, S.-Y.; Youn, I.-C.; Ahn, C.-H.; Yoon, S. M.; Myung, S.-J.; Moon, D. H.; Chen, X.; Choi, K.; Kwon, I. C.; Kim, K. *Nano Letters* **2009**, *9*, 4412.

12. Prashant, R.; Nambiar, G. G.; Nicholas A.; Lillo, Kishore Guda, Herbert E. Whiteley, Daniel W. *International Journal of Oncology* **2003**, *22*, 145.

13. Themelis, G.; Harlaar, N.; Kelder, W.; Bart, J.; Sarantopoulos, A.; Dam, G.; Ntziachristos, V. *Annals of Surgical Oncology* **2011**, *18*, 3506.

14. Terwisscha van Scheltinga, A. G. T.; van Dam, G. M.; Nagengast, W. B.; Ntziachristos, V.; Hollema, H.; Herek, J. L.; Schröder, C. P.; Kosterink, J. G. W.; Lub-de Hoog, M. N.; de Vries, E. G. E. *Journal of Nuclear Medicine* **2011**, *52*,

1778.

15. Van Dam, G. M.; Themelis, G.; Crane, L. M. A.; Harlaar, N. J.; Pleijhuis, R. G.; Kelder, W.; Sarantopoulos, A.; de Jong, J. S.; Arts, H. J. G.; van der Zee, A. G. J.; Bart, J.; Low, P. S.; Ntziachristos, V. *Nature Medicine* **2011**, *17*, 1315.

16. Mohs, A. M.; Mancini, M. C.; Singhal, S.; Provenzale, J. M.; Leyland-Jones, B.; Wang, M. D.; Nie, S. *Analytical Chemistry* **2010**, *82*, 9058.

17. Frangioni, J. V. *Journal of Clinical Oncology* **2008**, *26*, 4012.

18. van Oosten, M.; Schäfer, T.; Gazendam, J. A. C.; Ohlsen, K.; Tsompanidou, E.; de Goffau, M. C.; Harmsen, H. J. M.; Crane, L. M. A.; Lim, E.; Francis, K. P.; Cheung, L.; Olive, M.; Ntziachristos, V.; van Dijl, J. M.; van Dam, G. M. *Nature Communication* **2013**, *4*, 2584.

19. Tannock, I. F.; Lee, C. M.; Tunggal, J. K.; Cowan, D. S. M.; Egorin, M. J. *Clinical Cancer Research* **2002**, *8*, 878.

20. Agarwal, R.; Kaye, S. B. *Nature Reviews Cancer* **2003**, *3*, 502.

21. Rosbach, K. J.; Williams, M. D.; Gillenwater, A. M.; Richards-Kortum, R. R. *Translational Oncology* **2011**, *5*, 160.

22. Nomura, T.; Saikawa, A.; Morita, S.; Sakaeda, T.; Yamashita, F.; Honda, K.; Yoshinobu, T.; Hashida, M. *Journal of Controlled Release* **1998**, *52*, 239.

23. Scheuer, W.; van Dam, G. M.; Dobosz, M.; Schwaiger, M.; Ntziachristos, V. *Science Translational Medicine* **2012**, *4*, 134.

24. Paixão, P.; Aniceto, N.; Gouveia, L. F.; Morais, J. A. G. *European Journal of Pharmaceutical Sciences* **2013**, *50*, 526.

Chapter 6

Imaging of tumor-associated macrophages using dextran sulfate-based nanoprobes

6.1. Introduction

Macrophages are phygocytic cells in the immune system and respond to local environmental cues. Macrophages are categorized as classically activated macrophages (M1 macrophages) or alternatively activated macrophages (M2 macrophages).[1, 2] M1 macrophages are activated by lipopolysaccharide or interferon-γ, producing pro-inflammatory mediators and exerting antitumor cytotoxicity.[3] On the other hand, M2 macrophages are activated by stimulation with interleukin (IL)-4 and IL-13, secreting a wide range of angiogenic growth factors and secreting immunosuppressive cytokines. Recent, compelling evidence indicates that tumor-associated macrophages (TAMs), possessing M2-like qualities, play a significant role in promoting tumor angiogenesis, cell invasion, tumor growth, and metastasis in many human cancers, including colon, breast, skin, and lung.[4, 5] In particular, the extent of TAM infiltration within tumors generally correlates with poor prognosis, for example, in high-risk breast cancer.[6] Therefore, TAMs can be a unique target for tumor imaging, facilitating clinical applications for the prognosis and treatment of tumors.[7]

TAMs are known to over-express class A scavenger receptors (SR-A).[8, 9] SR-A is included in a family of scavenger receptors among membrane receptors and is a multifunctional receptor that binds with various negatively charged macromolecules.[10] Dextran sulfate (DS), a negatively charged derivative of dextran, performs as a ligand for SR-A.[11] Previously, DS nanoprobes (DSNPs) were

developed to detect SR-A-positive macrophages in rheumatoid arthritis. In this study, NIR fluorophore-labeled DSNPs were prepared and characterized. The *in vitro* cellular uptake of DSNPs was investigated in MDA-MB-468 cancer cells, RAW264.7 macrophage cells, and isolated TAM. *In vivo* body distribution of DSNPs was observed in MDA-MB-468 tumor-bearing mice. TAMs in excised tumors were confirmed with immunohistochemical analysis using anti-CD204 antibody, which were compared with the fluorescence signal from the DSNPs.

6.2. Experimental section

6.2.1. Materials

DS sodium salt (mw = 36–50 kDa) was obtained from MP Biochemicals, LLC (Santa Ana, CA). FPR675 (excitation and emission maximum of 674 nm and 699 nm, respectively) was purchased from Bioacts (Incheon, Korea). 4-Dimethylaminopyridine (DMAP), 4-nitrophenyl chloroformate, and 5β-cholanic acid were purchased from Sigma-Aldrich (St. Louis, MO). Fetal bovine serum (FBS) was purchased from Invitrogen Canada (Burlington, ON, Canada), and RPMI 1640 medium and Dulbecco's modification of Eagle's medium (DMEM) were obtained from Gibco (Grand Island, NY). Monoclonal mouse anti-CD68 antibody was purchased from Abcam (Cambridge, MA). Monoclonal mouse anti-F4/80

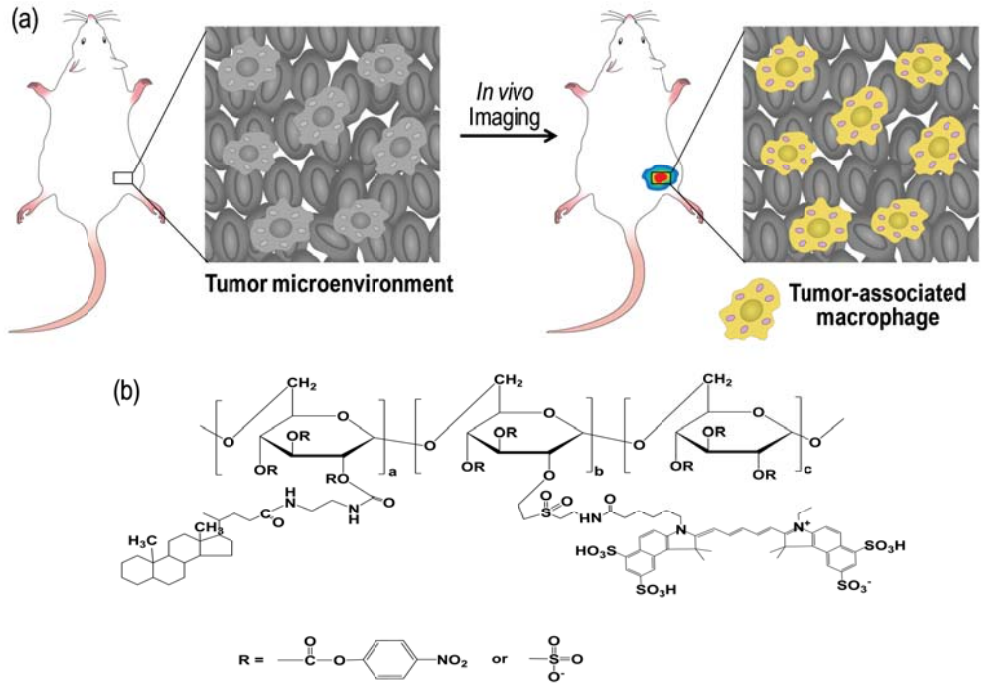

Figure 6.1. Schematic presentation describing that FPR675-labeled dextran sulfate-based nanoprobes (DSNPs) can be utilized for depicting infiltration of tumor-associated macrophage (TAM). (a) Illustration for detection of TAM infiltration. (b) Chemical structures of DSNPs.

conjugated with FITC and monoclonal mouse anti-CD204 (anti-SR-A) conjugated with FITC were purchased from Abcam (Cambridge, MA) and Novus Biologicals (Santa Cruz, CA), respectively. Collagenase was purchased from Sigma-Aldrich. 5(6)-Carboxyfluorescein N-hydroxysuccinimidyl ester (CFSE) Cell Labeling Kit was purchased from Abcam.

6.2.2. Preparation of dextran sulfate-based nanoprobes

For fluorophore labeling, FPR675 (2 mg, 1.7 μmol) was added dropwise to the DS in dimethyl sulfoxide (DMSO; 200 mg/ 80 ml).[12] The resulting solution was stirred for 24 h at room temperature (RT) and then dialyzed against distilled water (DW) with a cellulose membrane (MWCO = 6–8 kDa) for 72 h, resulting in FPR675-labeled DS. Amphiphilic FPR675-labeled DS-5β-cholanic acid conjugates were synthesized by chemically conjugating hydrophobic bile acid (5β-cholanic acid) to water-soluble FPR675-labeled DS. FPR675-labeled DS (100 mg, 0.262 mmol) was dissolved in DSMO/pyridine (1:1, v/v; 15 ml), which was added with 4-nitrophenyl chloroformate (158 mg, 0.786 mmol) and DMAP (9.6 mg, 0.0786 mmol) at 0 ^{o}C and argon atmosphere. After reacting for 4 h, the mixture was isolated through precipitation with ether/ethanol (1:1, v/v; 300 ml). The precipitate was filtered and washed with ether. The 4-nitrophenyl-activated FPR675-labeled DS dissolved in DMSO/pyridine (2:1, v/v) was mixed with aminoethyl 5β-cholanoamide (13. 81 mg, 0.0356 mmol) that was converted from 5β-cholanic acid.[13] The resulting solution

was stirred for 48 h at 50 °C and argon atmosphere and then dialyzed against water/methanol mixture (1:4, v/v) with a cellulose membrane (MWCO = 12–14 kDa) for 72 h. The FPR675-labeled DS-5β-cholanic acid conjugate (1 mg/ml) was sonicated with a probe-type sonicator (Ultrasonic Processor, GEX-600) in DW, resulting in well-dispersed FPR675-labeled DSNPs.

6.2.3. Characterization of dextran sulfate-based nanoprobes

The mean diameter and size distribution of DSNPs in DW were observed with dynamic light scattering (DLS) at 25°C. DSNPs' morphology in DW (1 mg/ml) was assessed with transmission electron microscopy (TEM, CM30 electronmicroscope, Philips, CA). TEM analysis was performed at 200 kV. The sample solution was placed on the grid for 2 min and excess solution was blotted with filter paper. For staining, the grid was placed on a drop of 2% (w/v) uranyl acetate. The zeta potentials of DSNPs (1 mg/ml) in DW were measured with an ELS-8000 eletrophoretic light scattering spectrometer (Ostuka, Electronics, Japan).

6.2.4. Isolation of tumor-associated macrophages

All animal experimental procedures were in compliance with the institutional guidelines of Korea Institute of Science and Technology and the relevant laws. TAMs were prepared as described by Solinas et al.[14, 15] Briefly, MDA-MB-468 cells

(1×10^6 cells/mouse) suspended in 50 μl of sterile saline were injected subcutaneously into the flank of BALB/c mice (20 g, Orient, Seoul, Korea). When tumors reached approximately 7.0 ± 0.5 mm in size, they were harvested from sacrificed MDA-MB-468 tumor-bearing BALB/c mice under sterile conditions to isolate TAMs. Excised tumors were chopped into small pieces, and then incubated with serum-free RPMI 1640 containing collagenase (1 mg/ml) for 1 h at 37°C. The digested tissues were filtered using a cell strainer with 70 μm pores to generate a single-cell suspension. Then, cells were recovered by centrifugation at 1000 rpm for 10 min, washed twice with phosphate-buffered saline (PBS), and resuspended in serum-free RPMI 1640. The cells were incubated for 1 h at 37°C, and then unattached cells were washed away. Isolated TAMs were maintained in RPMI 1640 medium containing 10% (v/v) FBS and penicillin G (100 U/ml)/streptomycin (100 μg/ml) at 37°C, 5% CO_2.

For characterization of the isolated TAMs, cells were plated in 35 mm cover-glass bottom dishes and incubated for 48 h. After washing with PBS, the cells were permeabilized and blocked. Cells were treated with monoclonal mouse anti-CD204 antibody (1:100 dilution) for overnight 4°C, and then with goat anti-mouse IgG-FITC (1:100 dilution) for 1 h. Then, the cells were stained with 4',6-diamidino-2-phenylindole (DAPI). The cells were observed using IX81-ZDC focus drift compensating microscope (Olympus, Tokyo, Japan).

6.2.5. Cytotoxicity and cellular uptake

MDA-MB-468, a breast cancer cell line, and RAW264.7, a macrophage cell line, were maintained in RPMI 1640 medium containing 10% (v/v) FBS and penicillin G (100 U/ml)/streptomycin (100 μg/ml) at 37°C, 5% CO_2. The DSNPs' cytotoxicity was evaluated using Cell Counting Kit-8 (CCK-8) assay. In brief, RAW264.7 or MDA-MB-468 cells (1×10^4 cells/well) were seeded in a 96-well microplate, and cultured for 24–36 h. The DSNPs (5, 25, 50, 100 μg/ml) were added to each well of the cell culture and incubated for 24 h. CCK-8 solution was added to each well of the cell culture and incubated for 2 h, and absorbance was observed at 450 nm with a plate reader. Cell viability was expressed as a percentage relative to the untreated control cells.

MDA-MB-468 (1×10^5 cells/dish), RAW264.7 (1×10^5 cells/dish), and the isolated TAM (1×10^5 cells/dish) were plated in 35 mm cover-glass bottom dishes and grown to 80% confluence. The cells were washed twice with PBS (pH 7.4) and then incubated with serum-free medium containing DSNPs (200 nM) for 6 h. The cells were washed with PBS (pH 7.4) twice, fixed with fresh 4% (v/v) paraformaldehyde at RT for 5 min, and mounted with Fluoromount-G™ (Southern Biotech, Birmingham, AL). Cellular uptake of DSNPs was observed using a confocal laser scanning microscope (Leica SP5, Leica Microsystems, Buffalo, Grove, IL).

To establish co-culture system of macrophage cells (RAW264.7) and cancer cells (MDA-MB-468), two types of cells were maintained in RPMI 1640 medium

containing 10% (v/v) FBS and penicillin G (100 U/ml)/streptomycin (100 μg/ml) at 37°C, 5% CO_2, respectively. To distinguish cancer cells and macrophage cells, the cancer cells were labeled using 5(6)-carboxyfluorescein N-hydroxysuccinimidyl ester (CFSE) cell labeling kit according to the manufacturer's protocol. A co-culture of macrophage cells and cancer cells was prepared by seeding 2×10^5 CFSE-labeled cancer cells and 2×10^5 macrophage cells onto 35 mm culture dish. The cells were cultured in RPMI 1640 medium containing 10% (v/v) FBS and penicillin G (100 U/ml)/streptomycin (100 μg/ml) at 37°C, 5% CO_2 for 24 h. The cells were washed twice with PBS (pH 7.4) and then incubated with serum-free medium containing DSNPs (200 nM) for 4 h. The DSNP uptake in the co-culture system was analyzed using a confocal laser scanning microscope.

6.2.6. *In vivo* and *ex vivo* fluorescence imaging

When MDA-MB-468 tumors reached approximately 7.0 ± 0.5 mm in size, DSNPs (1 mg/ml in 100 μl of PBS) was injected via tail vein to the tumor-bearing mice. *In vivo* NIR tomographic images were acquired with an eXplore Optix system (Advanced Research Technologies Inc., Montreal, Canada). For quantitative analysis, the total photon counts in tumors were calculated using the region of interest (ROI) measurement of the Analysis Workstation software program (Advanced Research Technologies Inc.). Values are presented as means ± standard deviations for groups of three animals. A one-way analysis of variance (ANOVA) was used for the comparison of continuous variables between groups. After *in vivo*

imaging studies, the mice were sacrificed, and the liver and tumor were excised and imaged using a Kodak image station (4000MM; Kodak, New Haven, CT) equipped with a special C-mount lens and FPR675 bandpass emission filters.

6.2.7. Histological analysis

For the histological evaluation, each excised tumor was divided into two pieces, and one was fixed in 4% (v/v) buffered formalin and embedded in paraffin. The other was embedded in optimum cutting temperature (OCT) compound for cryo-section preparation. The paraffin-embedded specimens were cut into 5 μm-thick sections, and they were stained with hematoxylin and eosin (H&E) or used for immunohistochemistry (IHC) against CD68. For IHC, the paraffin-embedded sections were deparaffinized and rehydrated with xylene, graded ethanol, and PBS (pH 7.4). Endogenous peroxidase was blocked by incubating the sections in 3% hydrogen peroxide in PBS for 20 min at RT. After being washed three times, each section was then incubated with primary antibodies to CD68 (1:200 dilution) for 2 h at RT. HISTOSTAIN®-PLUS Kit (Invitrogen, Carlsbad, CA) was applied to detect binding of primary reagents. Sections were counterstained with Harris's hematoxylin (Sigma) and examined using light microscope (BX51TF, Olympus). The 8 μm-thick frozen sections were prepared for fluorescence microscopic imaging of FPR675-labeled DSNPs and for IHC against F4/80 (1:200 dilution) or CD204 (1:200 dilution). The slices were washed with DW, permeablized with H_2O_2

solution, and then incubated with primary antibodies to F4/80 (1:200 dilution) or CD204 (1:200 dilution) for 2 h at RT. The slides were washed with PBS and mounted. The slides were observed under the IX81-ZDC focus drift compensating microscope without histological stains.

6.3. Results

6.3.1. Characterization of dextran sulfate-based nanoprobes

As TAM-targeting nano-sized carriers, amphiphilic FPR675-labeled DS-5β-cholanic acid conjugates were self-assembled in DW. TEM and DLS analyses displayed that DSNPs formed a spherical nanoparticle and that it was 188.5 ± 5.27 nm in diameter (Figure 6.2). The zeta potential of DSNPs was -47.5 ± 1.26 mV in DW. No significant changes in the size and distribution of DSNPs were observed in PBS for two weeks, which demonstrates the long-term stability of DSNPs in physiological conditions (data not shown). DSNPs' cytotoxicity in RAW264.7 and MDA-MB-468 cells was determined using CCK-8 assay (Figure 6.2 c). DSNPs exhibited cell viability > 95% at concentrations up to 100 μg/ml.

6.3.2. Cellular uptake of dextran sulfate-based nanoprobes

The cellular uptake behavior of DSNPs was investigated using MDA-MB-468

cancer cells, RAW264.7 macrophage cells, and isolated TAM. TAM was isolated from MDA-MB-468 tumors in BALB/c mice. This isolated TAM was stained positively with CD204. Most adherent cells were TAMs as assessed by morphology and CD204 (M2 macrophage marker) positivity (Figure 6.3 a). After incubating 30 min of DSNPs in various types of cells, a very low fluorescence signal from DSNPs was detected in the MDA-MB-468 cells, whereas a strong fluorescence signal was detected in the RAW264.7 cells and the isolated TAM (Figure 6.3 b). In the case of FPR675-labeled glycol chitosan nanoparticles (chitosan nanoprobes; CNPs), which have been evaluated as good optical probes for targeting of tumor cells, they showed high uptake into MDA-MB-468 cells and low uptake into RAW264.7 cells and the TAMs. In the co-culture system of macrophage cells and cancer cells, DSNPs entered preferentially in macrophage cells, indicating that DSNPs possess targeting capacity for macrophage cells.

6.3.3. *In vivo* distribution of dextran sulfate-based nanoprobes

At 1 h post-injection of DSNPs (5 mg/ml) through the tail vein, the fluorescence signals of tumor and liver sites were slightly increased. Then, tumor and liver sites were clearly delineated from the surrounding tissues 5 h post-injection of DSNPs and slowly diminished afterwards (Figure 6.4 a). In *ex vivo* images of excised liver and tumor at 24 h post-injection of DSNPs, higher NIR fluorescence intensity was observed in the tumor tissues than that of liver (Figure 6.4 b).

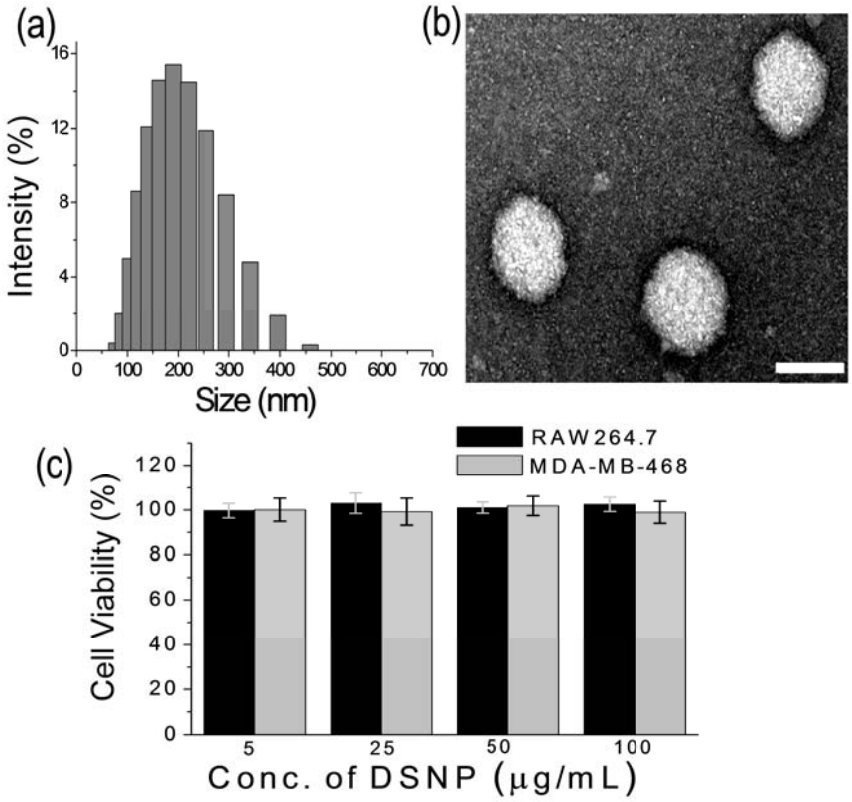

Figure 6.2. Characterization of dextran sulfate-based nanoprobes (DSNPs). (a) Size distribution of DSNPs in distilled water. (b) Transmission electron microscopy image of DSNPs. The scale bar indicates 200 nm. (c) Cell viability measured with Cell Counting Kit-8 assay. RAW264.7 and MDA-MB-468 cells were incubated for 24 h with various concentrations of DSNPs (5, 25, 50, 100 μg/ml).

6.3.4. Immunohistochemistry of tumor tissues

To reach approximately 7.0 ± 0.5 mm in diameter, tumor were grown for 6 weeks. Tumoral and peritumoral tissues from MDA-MB-468 subcutaneous tumors were analyzed with the histology and the IHC against CD68 (macrophage marker).[16] In H&E, a large number of infiltrated macrophages were detected in the peritumoral area, while small number of macrophages was detected in the tumoral area (Figure 6.5 a). Immunohistochemical analyses demonstrated that CD68-positive macrophages were present mainly in the peritumoral area and slightly in the tumoral area. In addition, the fluorescence signal from DSNPs (red) in the tumor tissue was co-localized both with those of F4/80 (green) or CD204 (green), respectively (Figure 6.5).

6.4. Discussion

Among various immune cells, TAMs are the crucial players in tumor microenvironment for mediating immuno-suppression.[5] TAMs are infiltrated into the tumor site by chemokines, cytokines, and other tumor-derived factors, which preferentially localize at the tumor-stroma interface.[2] TAMs have a tumor-supportive M2 function, which is differentiated from a tumor-supportive M1 function. They secrete a wide range of angiogenic growth factors including vascular endothelial growth factor (VEGF) and matrix-remodeling proteases such as

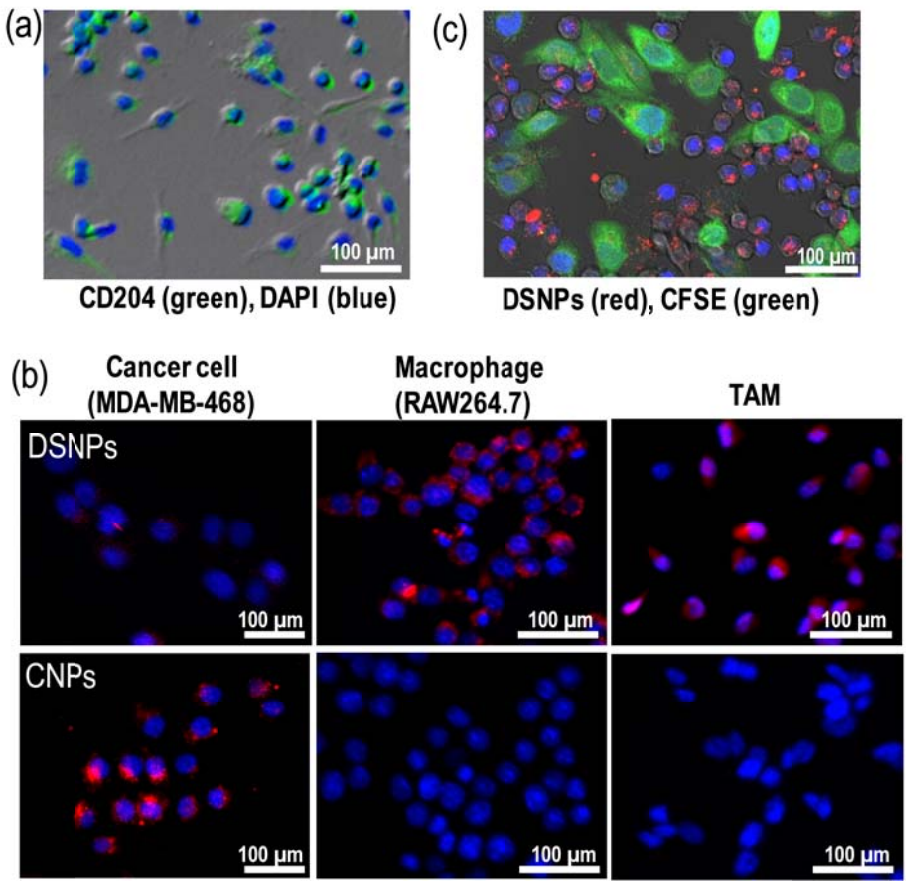

Figure 6.3. Immunocytochemistry of the isolated tumor-associated macrophages (TAMs) and cellular uptake of dextran sulfate-based nanoprobes (DSNPs). (a) Immunocytochemistry against CD204 of the isolated TAMs. Fluorescein isothiocyanate-conjugated antibody against CD204 was used for CD204 (green) imaging. (b) Cellular uptakes of DSNPs (red) and CNPs (red) in MDA-MB-468 cancer cells, RAW264.7 macrophages, and the isolated TAMs. FPR675-labeled DSNPs or chitosan nanoprobes (CNPs) were displayed as red fluorescence signals. (c) Cellular uptake of DSNPs (red) in the co-culture system of cancer cells and macrophage cells. Cancer cells were stained with 5(6)-carboxyfluorescein N-hydroxysuccinimidyl ester (CFSE, green) cell labeling kit. The scale bars indicate 100 µm. The nucleus was stained with DAPI (blue).

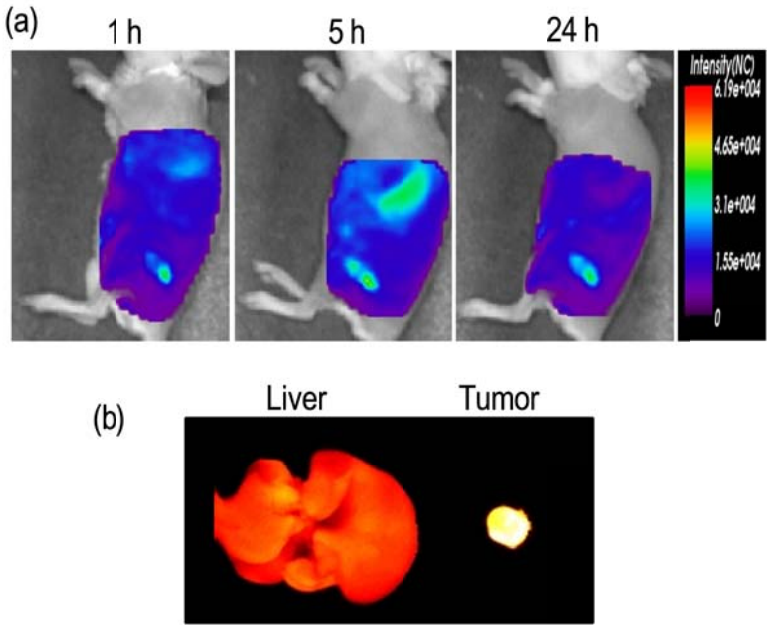

Figure 6.4. *In vivo* and *ex vivo* near infrared (NIR) fluorescence imaging using dextran sulfate-based nanoprobes (DSNPs) in MDA-MB-468 tumor-bearing mice. (a) Whole-body NIR fluorescence images of MDA-MB-468 tumor-bearing mice after intravenous injection of DSNPs. (b) *Ex vivo* images of a liver and tumor acquired with the KODAK image station 24 h after intravenous injection of DSNPs.

metalloproteinases and cathepsins, promoting tumor progression and metastasis. In addition, they overexpress immunosuppressive cytokines such as transforming growth factor (TGF)-β and IL-10, which hampers the infiltration of antitumor immune cells and further encourages a microenvironment conducive to tumor progression. Recently, there has been increasing clinical and preclinical evidence associating abundance of TAM with poor prognosis.[1, 17-19] Therefore, the monitoring of TAM infiltration in tumors could extend the clinical applications regarding cancer prognosis. Moreover, imaging of TAMs *in vivo* could be helpful in elucidating their role in cancer progression and evaluating macrophage-targeted treatment.

So far, TAMs have been predominantly identified using CD68 immunostaining.[10, 20] However, CD68 is a marker used to assess TAM, which cannot distinguish the M2 phenotype from monocytes and subpopulations of macrophages. Recently, CD204 (SR-A) has been recognized as a useful marker for the detection of TAMs. CD204 has been confirmed to be a specific marker for the immunosuppressive M2 macrophages useful for discriminating polarized M2 macrophages from M1 macrophages.[10, 20] CD204 has been reported to be strongly expressed in the TAMs. In addition, CD204-positive TAMs were significantly correlated with poor prognosis and malignant phenotypes in patients with glioma, pancreatic cancer, and ovarian epithelial tumors. In the immunostaining experiments assessing TAM, the antibodies against CD68, F4/80, and CD204 were utilized. Considering the diverse and heterogeneous TAMs population including multiple subtypes, it could be more

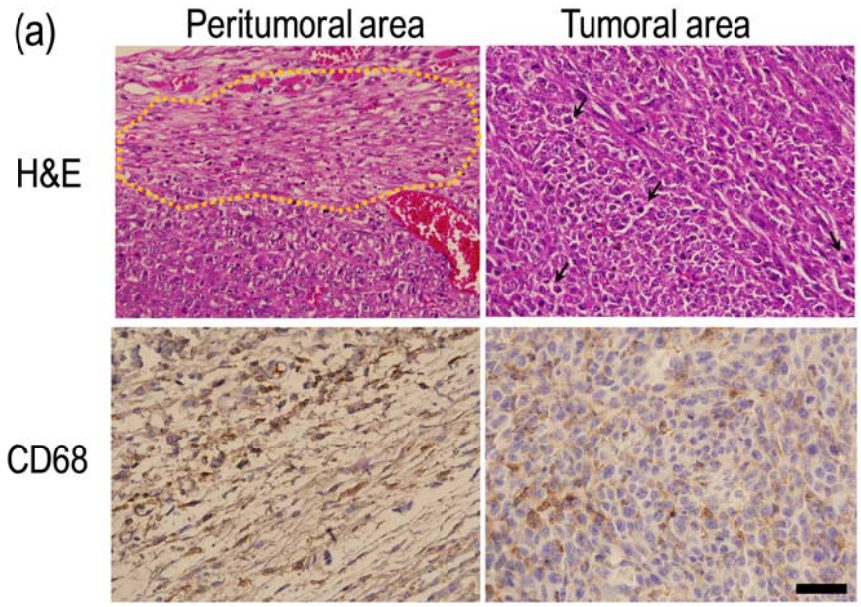

Figure 6.5. Histological and immunohistochemical analyses of the excised MDA-MB-468 tumors. (a) Hematoxylin and eosin staining images of tumoral and peritumoral tissues from MDA-MB-468 subcutaneous tumors. The yellow dotted line indicates a large number of infiltrated macrophages in the peritumoral area, and the arrows indicate the small number of macrophages in the tumoral area. Immunohistochemical analysis of CD68 for tumoral and peritumoral tissues from MDA-MB-468 subcutaneous tumors. The scale bar indicates 25 μm. (continued)

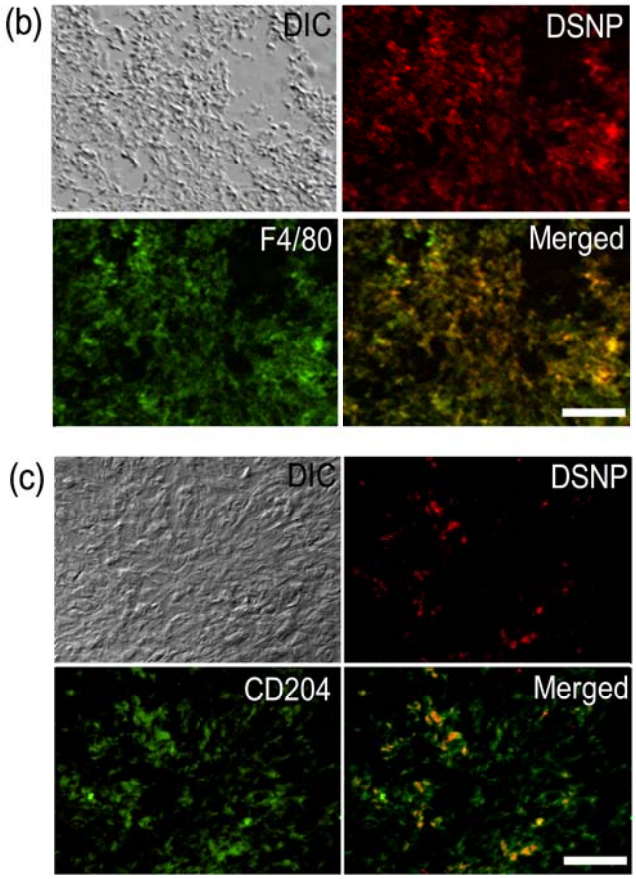

Figure 6.5. Histological and immunohistochemical analyses of the excised MDA-MB-468 tumors. Fluorescein isothiocyanate-conjugated antibodies against (b) F4/80 or (c) CD204 are displayed in green, and FPR675-labeled dextran sulfate-based nanoprobes (DSNPs) are displayed in red. The scale bar indicates 50 μm.

favorable to utilize two or more markers for detecting TAMs.

6.5. Conclusions

FPR675-labeled dextran sulfate-based nanoprobes (DSNPs) were developed to detect TAMs in tumors. DSNPs were significantly uptaken into RAW264.7 macrophage cells and isolated TAMs, not in MDA-MB-468 cancer cells. Immunohistochemical analysis using and CD68 (macrophage marker) displayed that TAM infiltration was mainly observed in peritumoral area of MDA-MB-468 tumors. In addition, DSNPs mainly target CD204 (M2 macrophage marker)-positive TAMs. This suggests that DSNPs could be potentially utilized to image TAM infiltration in tumors.

6.6. References

1. Cieslewicz, M.; Tang, J.; Yu, J. L.; Cao, H.; Zavaljevski, M.; Motoyama, K.; Lieber, A.; Raines, E. W.; Pun, S. H. *Proceedings of the National Academy of Sciences* **2013**, *110*, 15919.

2. Yu, S. S.; Lau, C. M.; Barham, W. J.; Onishko, H. M.; Nelson, C. E.; Li, H.; Smith, C. A.; Yull, F. E.; Duvall, C. L.; Giorgio, T. D. *Molecular Pharmaceutics* **2013**, *10*, 975.

3. Hagemann, T.; Wilson, J.; Burke, F.; Kulbe, H.; Li, N. F.; Plüddemann, A.; Charles, K.; Gordon, S.; Balkwill, F. R. *The Journal of Immunology* **2006**, *176*, 5023.

4. Locke, L. W.; Mayo, M. W.; Yoo, A. D.; Williams, M. B.; Berr, S. S. *Biomaterials* **2012**, *33*, 7785.

5. Zhu, S.; Niu, M.; O'Mary, H.; Cui, Z. *Molecular Pharmaceutics* **2013**, *10*, 3525.

6. Mukhtar, R. A.; Nseyo, O.; Campbell, M. J.; Esserman, L. J. *Expert Review of Molecular Diagnostics* **2011**, *11*, 91.

7. Verdoes, M.; Edgington, Laura E.; Scheeren, F. A.; Leyva, M.; Blum, G.; Weiskopf, K.; Bachmann, Michael H.; Ellman, Jonathan A.; Bogyo, M. *Chemistry & Biology* **2012**, *19*, 619.

8. Mantovani, A.; Sozzani, S.; Locati, M.; Allavena, P.; Sica, A. *Trends in Immunology* **2002**, *23*, 549.

9. Zhao G, R. B. *International Journal of Nanomedicine* **2013**, *8*, 61.

10. Ohtaki, Y.; Ishii, G.; Nagai, K.; Ashimine, S.; Kuwata, T.; Hishida, T.; Nishimura, M.; Yoshida, J.; Takeyoshi, I.; Ochiai, A. *Journal of Thoracic Oncology* **2010**, *5*, 1507.

11. You, D. G.; Saravanakumar, G.; Son, S.; Han, H. S.; Heo, R.; Kim, K.; Kwon, I. C.; Lee, J. Y.; Park, J. H. *Carbohydrate Polymers* **2014**, *101*, 1225.

12. Park, J. W.; Kim, Y.; Lee, K.-J.; Kim, D. J. *Bioconjugate Chemistry* **2012**, *23*, 350.

13. Choi, K. Y.; Min, K. H.; Na, J. H.; Choi, K.; Kim, K.; Park, J. H.; Kwon, I. C.; Jeong, S. Y. *Journal of Materials Chemistry* **2009**, *19*, 4102.

14. Solinas, G.; Schiarea, S.; Liguori, M.; Fabbri, M.; Pesce, S.; Zammataro, L.; Pasqualini, F.; Nebuloni, M.; Chiabrando, C.; Mantovani, A.; Allavena, P. *The Journal of Immunology* **2010**, *185*, 642.

15. Duff, M. D.; Mestre, J.; Maddali, S.; Yan, Z. P.; Stapleton, P.; Daly, J. M. *Journal of Surgical Research* **2007**, *142*, 119.

16. Melancon, M. P.; Lu, W.; Huang, Q.; Thapa, P.; Zhou, D.; Ng, C.; Li, C. *Biomaterials* **2010**, *31*, 6567.

17. Komohara, Y.; Ohnishi, K.; Kuratsu, J.; Takeya, M. *The Journal of Pathology* **2008**, *216*, 15.

18. Kawamura, K.; Komohara, Y.; Takaishi, K.; Katabuchi, H.; Takeya, M. *Pathology International* **2009**, *59*, 300.

19. Kurahara, H.; Shinchi, H.; Mataki, Y.; Maemura, K.; Noma, H.; Kubo, F.; Sakoda, M.; Ueno, S.; Natsugoe, S.; Takao, S. *Journal of Surgical Research* **2011**, *167*, 211.

20. Shigeoka, M.; Urakawa, N.; Nakamura, T.; Nishio, M.; Watajima, T.; Kuroda, D.; Komori, T.; Kakeji, Y.; Semba, S.; Yokozaki, H. *Cancer Science* **2013**, *104*, 1112.

요 약

분자영상은 21세기 암 치료에 있어서 매우 중요한 요소이다. 분자영상은 살아있는 상태에서 세포 또는 분자 수준에서 일어나는 질병과 관련있는 변화를 가시화하여 눈으로 보여주는 기술이다. 분자영상은 암을 보다 조기에 발견할 수 있게 하여 치료 효율을 높이는데 기여한다. 이 외에도 분자영상은 치료효과를 실시간으로 평가하고, 종양의 제거 수술 중에 종양의 위치와 크기를 빠르고 정확하게 보여주는데 기여할 수 있다. 여러 분자영상 방식 중에서 광학영상 방식은 적은 양의 타깃 물질도 민감하게 감지할 수 있으며 실시간 이미징 및 다양한 형광체를 이용한 다중 이미징이 가능하다는 점에서 장점이 있다.

오랫동안 암 연구는 암세포에 있는 특정한 생체분자를 표적화하여 연구해왔다. 그러나 암은 암세포만 모여있는 것이 아니라 혈관 관련 세포, 면역세포, 섬유아세포, 단백질분해효소, 성장인자, 세포외기질 등의 다양한 요소가 종양세포 주위에 혼재하여, 종양이 성장하거나 전이하는데 큰 역할을 한다고 알려졌다. 이렇게 종양세포를 둘러싸고 있는 다양한 요소들을 총칭하여 종양미세환경이라고 한다. 최근 종양세포와 더불어 종양미세환경도 같이 연구하여 암 진단 및 치료에 응용하려는 시도가 늘어나

고 있다.

본 논문은 암의 발생과 진행 과정에 따라 변화하는 암의 중요 요소들을 가시화하는 분자영상에 대한 연구로, 암에 대한 이해도를 높이고 암의 진단 및 치료에 기여함을 목적으로 하였다. 본 논문에서 암세포와 주변 미세환경의 다양한 요소, 단백질 분해효소, 성장인자 수용체, 세포외기질, 종양조직, 대식세포를 표적으로 하는 광학 영상 실험을 수행하였다.

첫 번째로 암의 전이과정에서 과발현되는 특성을 지닌 단백질분해효소 카셉신을 이미징하였다. 카셉신에 특이적으로 반응하는 기질 펩타이드와 근적외선 형광, 소광체로 이루어진 펩타이드 프로브를 암 표적성을 가진 키토산 나노입자의 표면에 도입함으로써 카셉신 나노프로브를 합성하였다. 카셉신 나노프로브는 카셉신-B에만 특이적으로 활성화되어 카셉신-B에 민감도 높은 이미징이 가능하였다. 카셉신 나노프로브는 전이성 간암, 전이성 폐암, 전이성 복막암에 적용되어, 카셉신 나노프로브를 이용한 전이암 이미징의 가능성을 보여주었다.

두 번째로 종양세포 표면에 과량 존재하는 수용체 중 상피성장인자 수용체를 표적으로 이미징을 시도하였다. 수용체를 타깃으로 하는 이미징은 수용체에 대한 특이성이 높은 프로브를 사용할 수 있다는 장점이 있다. 상피성장인자 수용체의 천연 리간드인 상피성장인자를 사용하여 광

학프로브 (상피성장인자 나노프로브)를 합성하였다. 상피성장인자 나노프로브는 세포내로의 이입후 리소좀에서의 분해를 통해 형광이 나타났다. 세포 및 동물 이미징 실험을 통해, 상피성장인자 나노프로브가 상피성장인자 수용체에 대한 뛰어난 특이성을 가지고, 종양의 이미징을 가능하게 함을 보여주었다.

세 번째로 세포외기질에 존재하는 라이실-산화효소를 민감하게 검출할 수 있는 방법을 연구하였다. 라이실-산화효소는 세포외기질의 구성물질 중 가장 많은 비중을 차지하는 콜라겐 분자에 포함된 라이신을 알리신으로 변화시키는데 관여하는 효소이다. 알리신 또는 라이신에 대한 결합 반응성이 높은 특징을 가진 알리신은 주변 콜라겐의 라이신이나 알리신과 반응하여 콜라겐의 교차결합을 유도하여, 종양의 단단함을 증가시킨다. 단단한 종양은 종양의 악성화 및 전이의 가능성을 높이기 때문에, 라이실-산화효소를 민감하게 검출하는 것은 중요하다. 검출을 위해 금나노입자의 표면플라즈몬공명 현상으로 인한 색깔 및 흡수 파장이 변화되는 성질을 이용하였다. 금나노입자의 표면에 라이실-산화효소에 반응하는 펩타이드를 도입(라이실-산화효소-금나노입자)하여, 라이실-산화효소에 의해 금나노입자의 뭉침현상으로 인해 금나노입자 용액의 색깔 및 흡수 파장의 변화가 일어날 수 있도록 고안하였다. 이를 이용하여, 세포의 상

등액과 종양에서 추출한 단백질에서 라이실-산화효소의 정량적인 분석이 가능함을 보여주었다.

네 번째는 수술 중 종양의 위치와 크기를 빠르고 정확히 보여줄 수 있도록 국부 도포 방식으로 사용할 수 있는 이미징 프로브를 합성하였다. 조직을 잘 투과하는 프로브를 만들기 위해, 분포용적 수치가 다양한 약물에 근적외선 형광체를 도입하여 간암모델의 간 표면에 뿌려주었다. 이미징한 결과 분포용적 수치가 높은 약물과 형광의 결합체는 주로 종양부위에 존재하였고, 종양 내부로 빠르고 깊이 침투한 것이 관찰되었다. 높은 분포용적을 가진 약물은 종양과 정상조직을 구분할 수 있는 유용한 인자가 될 수 있을 것으로 생각한다.

마지막으로 종양미세환경 요소 중 암의 성장을 돕는 역할을 하는 종양연관 대식세포의 생체내 이미징을 시도하였다. 종양 연관 대식세포 표면에 과량 존재하는 스카빈저 수용체 (scavenger receptor class A, SR-A)의 리간드인 황산 덱스트란을 이용하여 광학 프로브를 합성하였다. 본 광학 프로브는 종양세포로의 이입은 잘 이루어지지 않았지만, 대식세포와 종양 연관 대식세포로의 이입은 잘 이루어졌다. 본 광학 프로브를 쥐의 꼬리정맥을 통해 종양모델에 주입한 후 실시한 조직학 검사를 통해 광학 프로브가 주로 SR-A 수용체를 가지고 있는 종양 연관 대식

세포를 표적하고 있음을 확인하였다.

암은 여러 요소들이 관여하고 있는 질병이다. 한가지 요소만을 표적으로 이미징하기 보다는 다양한 요소들을 표적화하는 연구를 통해서, 보다 민감하고 특이적인 암 진단을 이룰 수 있을 것으로 기대한다.

주요어: 분자영상, 암영상, 광학영상, 종양미세환경, 약물전달시스템

학번: 2010-31012